

DEVELOPMENT AND IMPLEMENTATION OF THE TRIGGER  
SYSTEM FOR THE INO-ICAL DETECTOR

BY

SUDESHNA DASGUPTA

ENROLMENT NO. PHYS01200804027

CONSTITUENT INSTITUTION BARC MUMBAI

A THESIS SUBMITTED TO THE  
BOARD OF STUDIES IN PHYSICAL SCIENCES  
IN PARTIAL FULFILLMENT OF REQUIREMENTS  
FOR THE DEGREE OF  
DOCTOR OF PHILOSOPHY  
OF  
HOMI BHABHA NATIONAL INSTITUTE



JUNE 2013



# Homi Bhabha National Institute

## Recommendations of the Viva Voce Board

As members of the Viva Voce Board, we certify that we have read the dissertation prepared by **Sudeshna Dasgupta** entitled "**Development and implementation of the trigger system for the INO-ICAL detector**" and recommend that it may be accepted as fulfilling the dissertation requirement for the Degree of Doctor of Philosophy.



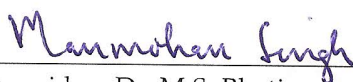
Chairman – Dr. A.K. Mohanty

Date: 21-3-2014



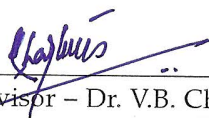
Guide/ Convener – Prof. N.K. Mondal

Date: 21.3.2014



Co-guide – Dr. M.S. Bhatia

Date: 21.3.2014



Technical Advisor – Dr. V.B. Chandratre

Date: 21.3.2014.



Technical Advisor – Dr. B. Satyanarayana

Date: 21/3/2014

Final approval and acceptance of this dissertation is contingent upon the candidate's submission of the final copies of the dissertation to HBNI.

We hereby certify that we have read this dissertation prepared under our direction and recommend that it may be accepted as fulfilling the dissertation requirement.

Date: 21.3.2014

Place: Mumbai



Guide – Prof. N.K. Mondal



Co-guide – Dr. M.S. Bhatia



## STATEMENT BY AUTHOR

---

This dissertation has been submitted in partial fulfillment of requirements for an advanced degree at Homi Bhabha National Institute (HBNI) and is deposited in the Library to be made available to borrowers under rules of the HBNI.

Brief quotations from this dissertation are allowable without special permission, provided that accurate acknowledgement of source is made. Requests for permission for extended quotation from or reproduction of this manuscript in whole or in part may be granted by the Competent Authority of HBNI when in his or her judgment the proposed use of the material is in the interests of scholarship. In all other instances, however, permission must be obtained from the author.

*Mumbai, June 2013*



---

Sudeshna Dasgupta



## DECLARATION

---

I hereby declare that the investigation presented in the thesis has been carried out by me. The work is original and has not been submitted earlier as a whole or in part for a degree / diploma at this or any other Institution / University.

*Mumbai, June 2013*



---

Sudeshna Dasgupta



Dedicated to

*My childhood ideal who continues to remain so ...*

**Netaji Subhash Chandra Bose**



## ACKNOWLEDGEMENTS

---

I express my sincere gratitude to my supervisor Prof. Naba K Mondal for his constant support and guidance throughout the course of this work. I have always been immensely inspired by his enthusiasm and dedication towards research.

I thank my co-guide Dr. M.S. Bhatia for his meticulous supervision of my work. I am equally thankful to my Doctoral Committee members, Dr. A.K. Mohanty and Dr. V.B. Chandratre, for their kind help and advice.

I am largely indebted to Dr. B. Satyanarayana who stands as the pillar of support, not only for me, but for each and every student working in the INO collaboration. This journey would have been a lot more difficult without his motivation and encouragement, on the academic as well as personal front.

I am extremely grateful to Prof. Sreerup Raychaudhuri for generously teaching me the fundamentals of Quantum Mechanics and Particle Physics during the early days of graduate school coursework. Being from engineering background, I was very much a stranger in these fields and would not have been able to acquire the essential knowledge but for his kind help.

I am also thankful to the other teachers of graduate courses, Prof. Gobinda Majumder, Prof. Vivek M Datar, Prof. Amol Dighe and Prof. Vandana Nanal, for imparting knowledge in diverse fields in the most attractive and impressive manner.

This work has been accomplished owing to the valuable contributions of my present and past colleagues in the Detector and Electronics R&D team of the ICAL experiment. I am especially indebted to Dr. Deepak Samuel who was instrumental in training me in the state-of-the-art technologies in both hardware and software domains and has been an everlasting source of encouragement. I am grateful to Mr. Suresh Upadhyaya, Mr. Suresh Kalmani, Mr. Nagaraj Panyam, Mr. Venkatesam Reddy, Mr. Piyush Verma, Mr. Sharad Joshi, Mr. Ravindra Shinde, Mr. Mandar Saraf, Mr. Manas Bhuyan, Mr. Shekhar Lahange, Ms. Asmita Redij, Mrs. Sonal Dhuldhaj, Mrs. Darshana Gonji, Mrs. Noopur Srivastava, Mrs. Shobha Rao, Mr. Vishal Asgolkar, Mr. Santosh Chavan and Mr. Ganesh Ghodke for their crucial assistance in different arenas of my work. I also thank Prof. Sudeb Bhattacharya, Prof. James Libby and Mrs. Anita Behere for their valuable inputs which largely aided in streamlining the progress of my work.

I owe my thanks to Prof. B.S. Acharya for painstakingly going through the manuscript of the thesis and providing useful suggestions which enhanced the quality of the thesis to a great extent.

I would like to thank the INO Graduate Training Program, whose first batch I belong to, for providing the excellent and rare opportunity of gaining hands-on experience in building the biggest ever scientific experiment of the country.

I am thankful to all INO collaboration members and my friends, particularly, Tarak Thakore, Sumanta Pal, Anushree Ghosh, Nitali Dash, Vivek Singh, Moon Moon Devi, S. Mathimalar, Varchaswi Kashyap, Ali Ajmi, Deepak Tiwari, Abhik Jash, Mohammed Salim, Kolahal Bhattacharya, Sanmay Ganguly and Nilay Kundu, for their enduring support and motivation which have enabled me to tread this long path.

I take pride in my joint family, my relatives, my small and quiet hometown, my teachers and my school and college friends, each of whom have played pivotal roles in shaping the journey of my life so far. I regret my recent bereavement of my grandfather, Late Nihar Ranjan Sengupta, who would have been extremely delighted to see this day.

Finally and most importantly, I express my deepest gratitude to my parents, Mr. Ranendra Dasgupta and Mrs. Alpana Sengupta, who have set before me the example of honesty and integrity, always granted me the full freedom to pursue my dreams and continue to inspire me to push the limits every day.

*Mumbai, June 2013*



---

Sudeshna Dasgupta

## ABSTRACT

---

The elusive neutrino has always perplexed the scientific community. The desperate attempt by Pauli in postulating its existence, followed by experimental discovery, to save the laws of conservation of energy and momentum in nuclear  $\beta$ -decay, bear testimony to this fact. Subsequent experiments like, Homestake, Sudbury Neutrino Observatory (SNO), Super-Kamiokande and KamLAND, have studied neutrinos produced in the Sun, those originating from cosmic ray interactions in the Earth's atmosphere and also those generated in nuclear reactors. Results from such pioneering experiments provide concrete evidence in support of neutrino mass through the detection of neutrino oscillations. This serves as the first indication of the Physics beyond the Standard Model. Neutrino has also emerged as an excellent probe in comprehending the underlying laws of nature in particle physics, nuclear physics, astronomy and cosmology. As a natural consequence, further experiments, armed with technological superiority, are being pursued world-wide to explore this particle of interest.

In this context, a multi-institutional venture, called the India-based Neutrino Observatory (INO), has been initiated in India to participate in this exciting area of experimental particle physics by building a world-class underground facility for studying neutrinos.

The INO collaboration has proposed to build a 50 kton magnetized Iron Calorimeter (ICAL) detector to study atmospheric neutrinos and to make precision measurements of the neutrino oscillation parameters. The detector will mostly look for muon neutrino induced charged current interactions using magnetized iron as the target mass and around 28,800 Resistive Plate Chambers (RPCs) as sensitive detector elements. A magnetic field of 1.3 T will be used to discriminate between neutrino and anti-neutrino interactions, which equips the ICAL detector with the unique capability of determining the neutrino mass hierarchy. The detector is also envisaged as a future far detector for a neutrino factory beam.

The extremely low rate of neutrino interactions necessitates the trigger scheme for such an experiment to achieve an optimization of the detection efficiency of the desired events and the chance trigger rates. It should also ensure feasibility of hardware implementation considering the vast volume of the detector. The development, validation and implementation of the ICAL trigger system, which satisfy these criteria, are documented in this thesis.

The design of the trigger scheme for the ICAL detector consists of a distributed and hierarchical architecture. The detector module is logically sub-divided into identical segments for the purpose of

trigger generation. The segment dimensions are chosen considering the expected hit pattern of the events of interest, the associated chance trigger rates and the feasibility of implementation. Pre-trigger signals produced at the RPC level are combined together to generate a local trigger at the segment level, which in turn initiates a global trigger signal to invoke the data acquisition system to record the event data.

The associated chance trigger rates have been calculated for different segment dimensions and for different sets of trigger criteria and are found to be negligible for an optimal combination of the trigger parameters. A simulation framework is developed to estimate the trigger efficiency of the scheme for the events of interest for the ICAL detector. The results ensure that substantially high detection efficiency can be obtained for the desired events under the proposed trigger scheme.

The hardware implementation of the trigger scheme is initiated by designing an FPGA-based trigger module using the look-up table based technique. The module has delivered satisfactory performance in the prototype detector with negligible spurious trigger rate and trigger inefficiency. This ensures that such technique can be successfully and reliably employed in designing the ICAL trigger system.

The overall layout for the implementation of the proposed trigger scheme for the ICAL detector has been devised and the trigger latency is estimated. A study is undertaken to ascertain the reliability of LVDS standard in transmitting the trigger signals for the ICAL detector. A technique for calibrating the delay offsets associated with the return-path of the trigger signal is proposed. The designs of the trigger boards are conceived and appropriate design components have been selected.

The work reported here has thus facilitated the evolution of the ICAL trigger system from the conceptual stage up to the board-level design.

The thesis is proposed to comprise six chapters. Chapter 1 contains a brief history of neutrino and its salient features. The major experiments that have been carried out for the detection and understanding of this fundamental particle are reviewed. The physics potential of the ICAL detector, proposed to be built by the INO collaboration, is summarized. Chapter 2 describes the architecture of the proposed trigger scheme for the ICAL detector and its validation results. The design of an FPGA-based trigger module for the ICAL prototype detector and its performance validation are discussed in Chapter 3. Chapter 4 illustrates the overall layout for the hardware implementation of the trigger system for the ICAL detector. Chapter 5 deals with the conceptual designs of the trigger boards proposed to constitute the ICAL trigger system. The work is finally summarized and the future scope is discussed in Chapter 6. The publications produced as the outcome of this work, which include peer-reviewed research articles, conference proceedings and technical notes, are listed in Appendix A.

# CONTENTS

---

Synopsis	xvii
List of Figures	xxxv
List of Tables	xli
Acronyms	xlili

## I INTRODUCTION 1

1	NEUTRINO PHYSICS	3
1.1	History of neutrino	3
1.2	Neutrino in the Standard Model	4
1.3	Neutrino oscillation	6
1.4	Sources of neutrinos	9
1.5	Neutrino oscillation experiments	12
1.5.1	Solar neutrino experiments	12
1.5.2	Atmospheric neutrino experiments	15
1.5.3	Reactor neutrino experiments	16
1.5.4	Accelerator neutrino experiments	18
1.5.5	Summary of results on oscillation parameters	19
1.6	Open questions	19
1.7	Physics potential of the INO-ICAL detector	21
1.8	Trigger system for the ICAL detector	24

## II RESEARCH WORK 27

2	DEVELOPMENT AND VALIDATION OF ICAL TRIGGER SCHEME	29
2.1	Signal flow in the data acquisition system	29
2.2	The trigger criteria	29
2.3	The trigger scheme	30
2.3.1	RPC level	31
2.3.2	Segment level	33
2.3.3	Module level	37
2.4	Surface and underground chance trigger rates	40
2.5	Trigger simulation framework	42
2.5.1	Analysis input	42
2.5.2	Results	43
3	TRIGGER MODULE FOR ICAL PROTOTYPE DETECTOR	55
3.1	The prototype detector	55
3.2	The trigger system	56
3.2.1	Level 0 trigger signal	57
3.2.2	Level 1 trigger signal	57
3.2.3	Level 2 trigger signal	57
3.2.4	Final trigger signal	57
3.3	The Final Trigger Module	58
3.4	Performance validation	61

3.4.1	False triggers	61	
3.4.2	Missed triggers	63	
3.4.3	Coincidence rates and final trigger rate	64	
3.4.4	Additional inputs	64	
4	IMPLEMENTATION LAYOUT OF THE ICAL TRIGGER SYSTEM		69
4.1	Trigger system layout	69	
4.1.1	Scheme A	70	
4.1.2	Scheme B	73	
4.2	Study of LVDS transmission	76	
4.2.1	Experimental set-up	77	
4.2.2	Results	78	
4.3	Delay offset calibration	82	
5	DESIGN OF TRIGGER BOARDS FOR THE ICAL DETECTOR		87
5.1	The ICAL Engineering Module	87	
5.2	Trigger system layout for the Engineering Module	87	
5.3	The Local Trigger Module	90	
5.4	The Global Trigger Module	95	
5.5	Component selection for design of trigger boards	97	
5.5.1	FPGA	97	
5.5.2	LVDS drivers	98	
5.5.3	Connectors	98	
5.5.4	Back-end interface	101	
5.6	LTM board design	101	
5.7	GTM board design	101	
	<b>III CONCLUSIONS</b>	105	
6	SUMMARY AND FUTURE SCOPE		107
6.1	Summary	107	
6.2	Future scope	109	
	<b>IV APPENDIX</b>	111	
A	PUBLICATIONS AND PROCEEDINGS		113
A.1	Peer-reviewed research papers	113	
A.2	Conference proceedings	113	
A.3	Technical notes	114	
	<b>BIBLIOGRAPHY</b>	115	

## SYNOPSIS

---

### 1 PROPOSED CONTENTS OF THE THESIS

This thesis reports the work on the development, validation and implementation of the trigger system for the INO-ICAL detector. The thesis is proposed to comprise six chapters. Chapter 1 contains a brief history of neutrino and its salient features. The major experiments that have been carried out for the detection and understanding of this fundamental particle are reviewed. The physics potential of the Iron Calorimeter detector, proposed to be built by the India-based Neutrino Observatory collaboration, is summarized. Chapter 2 describes the architecture of the proposed trigger scheme for the ICAL detector and its validation results. The design of an FPGA-based trigger module for the ICAL prototype detector and its performance validation are discussed in Chapter 3. Chapter 4 illustrates the overall layout for the hardware implementation of the trigger system for the ICAL detector. Chapter 5 deals with the conceptual design of the trigger boards proposed to constitute the ICAL trigger system. The work is finally summarized and the future scope is discussed in Chapter 6. The publications produced as the outcome of this work, which include peer-reviewed research articles, conference proceedings and technical notes, are listed in Appendix A.

### 2 INTRODUCTION

The elusive neutrino has always perplexed the scientific community. It has turned out to be of fundamental importance in comprehending the underlying laws of nature in particle physics, nuclear physics, astronomy and cosmology [1]. Neutrinos can be classified based upon their source, like, solar neutrinos, supernova neutrinos, atmospheric neutrinos, geoneutrinos, reactor neutrinos, accelerator neutrinos, etc., and are detected in a wide energy range. The existence of neutrino was postulated by Pauli in 1930 [2] as a desperate attempt to save the laws of conservation of energy and momentum in nuclear  $\beta$ -decay. The first experimental detection of neutrino was achieved by Reines and Cowan in 1956 [3][4]. Results from subsequent experiments, like, Homestake, Sudbury Neutrino Observatory (SNO), Super-Kamiokande and KamLAND, established the phenomenon of neutrino oscillation [5]. This discovery, in turn, led to the concept of neutrino mass. This is in contradiction with the Standard Model of particle physics, that describes neutrino as a weakly interacting particle, which is massless and electrically neutral. This observation, therefore, paved the way

for further experiments world-wide. They are aimed at exploring the physics beyond the Standard Model, like, precision measurement of neutrino oscillation parameters, study of charge-conjugation and parity (CP) violation in the leptonic sector, determining the neutrino mass hierarchy and the absolute mass scale of neutrino, etc.

In this context, a multi-institutional venture, called the India-based Neutrino Observatory (INO), has been initiated in India to participate in this exciting area of experimental particle physics by building a world-class underground facility for studying neutrinos.

### 3 THE IRON CALORIMETER DETECTOR

The INO collaboration has proposed to build a 50 kton magnetized Iron Calorimeter (ICAL) detector to study atmospheric neutrinos and to make precision measurements of the neutrino oscillation parameters [6]. The detector will mostly look for muon neutrino induced charged current interactions using magnetized iron as the target mass and around 28,800 Resistive Plate Chambers (RPCs) as sensitive detector elements. The ICAL detector will consist of three identical modules, each of dimension 16 m x 16 m x 14.5 m. Each detector module will be made up of 151 horizontal layers of 56 mm thick low carbon iron plates interleaved with 40 mm gaps to house the RPC units. The detector will be located inside a cavern with rock cover of more than 1 km in order to reduce the cosmic muon background.

The ICAL detector is envisaged as a detector for atmospheric neutrinos as well as a future far detector for a neutrino factory beam. The major physics goals of the ICAL detector are listed below.

- Unambiguous and more precise estimation of the neutrino oscillation parameters using atmospheric neutrinos.
- Study of matter effects for  $\nu_\mu$  and  $\bar{\nu}_\mu$  through electric charge identification of muons in charged current interactions in order to determine the mass ordering, otherwise known as the neutrino mass hierarchy.
- Study of charge-conjugation and parity (CP) violation in the leptonic sector as well as possible charge-conjugation, parity, time-reversal (CPT) violation.
- Exploring the possible existence of sterile neutrinos.
- Constraining long range leptonic forces.
- Study of multi-TeV cosmic ray muons through pair-meter technique.

## 4 RESEARCH WORK

### 4.1 *Neutrino interactions in ICAL*

Neutrino interactions in iron produce charged particles like muon and/or hadrons. A muon typically produces a long track inside the detector, traversing many layers, while hadrons give rise to shower, confined within a few layers. The energy of the neutrino can be estimated from the momentum of the tracked muon and the hit distribution of the hadron shower.

The trigger criteria should be decided considering the characteristic hit pattern of such events so as to achieve an optimization of the detection efficiency of the desired events and the chance trigger rates. The trigger scheme should also ensure feasibility of hardware implementation considering the vast volume of the detector.

### 4.2 *The trigger criteria*

The trigger decision for the ICAL detector will be based on the event topology and is defined as  $M \times N / P$ , where  $M$  is the minimum strip multiplicity per RPC plane and  $N$  is the minimum number of layers out of a group of  $P$  consecutive layers having such  $M$ -fold multiplicity. There will be a number of trigger criteria with different combinations of the trigger parameters for different types of physics events. Hence, the goal of the trigger system is to ensure that if an event satisfies one or more of the user-specified trigger criteria in any part of the detector, a trigger signal should be generated to initiate the data acquisition system to record the event.

### 4.3 *The trigger scheme*

The design of the trigger scheme follows a distributed and hierarchical architecture. The RPC forms the base level of trigger generation, where the Level 0 and the Level 1 trigger signals are formed. The next level in the hierarchy is segment, which is a logical unit consisting of a group of RPCs, and generates the Level 2 and the Level 3 trigger signals. A number of such logical segments together constitute the detector module, which is the final level for global trigger generation.

#### 4.3.1 *RPC level*

The RPC has two orthogonal readout planes, namely the X and the Y plane, each having 64 pick-up strips, which are treated as two independent and identical systems.

The signals from every 8th pick-up strip out of 64 strips on one plane of the RPC are OR-ed to generate 8 Level 0 trigger signals ( $T_{01}, \dots, T_{08}$ ), as shown below.

$$T_{0i} = S_{0+i} + S_{8+i} + S_{16+i} + S_{24+i} + S_{32+i} + S_{40+i} + S_{48+i} + S_{56+i}, \quad i = 1, 2, \dots, 8 \quad (1)$$

The Level 1 trigger ( $T_{1M}$ ) signals are obtained by  $M$ -fold coincidence of the consecutive  $T_0$  signals from each RPC plane. The combinations for the  $T_{1M}$  signals for  $M = 1, 2, 3, 4$  are shown below.

- 1-Fold :  $T_{11} = T_{01} + T_{02} + \dots + T_{07} + T_{08}$
- 2-Fold :  $T_{12} = T_{01} \cdot T_{02} + T_{02} \cdot T_{03} + \dots + T_{07} \cdot T_{08} + T_{08} \cdot T_{01}$
- 3-Fold :  $T_{13} = T_{01} \cdot T_{02} \cdot T_{03} + T_{02} \cdot T_{03} \cdot T_{04} + \dots + T_{07} \cdot T_{08} \cdot T_{01} + T_{08} \cdot T_{01} \cdot T_{02}$
- 4-Fold :  $T_{14} = T_{01} \cdot T_{02} \cdot T_{03} \cdot T_{04} + T_{02} \cdot T_{03} \cdot T_{04} \cdot T_{05} + \dots + T_{07} \cdot T_{08} \cdot T_{01} \cdot T_{02} + T_{08} \cdot T_{01} \cdot T_{02} \cdot T_{03}$

Considering a coincidence window of  $T$  seconds and a  $T_0$  rate of  $R$  Hz,  $M$ -fold chance rate  $r_M$  is given by [7],

$$r_M = C \cdot (MR^M T^{M-1}) \text{ Hz}, \quad C = \text{total no. of combinations} \quad (2)$$

#### 4.3.2 Segment level

The detector module is logically sub-divided into identical segments for the purpose of trigger generation. Each segment is capable of generating a local trigger, which will in turn initiate a global trigger. The segment dimensions are chosen considering the expected hit pattern of the events, the associated chance trigger rates and the feasibility of implementation. Every two adjacent segments must have overlap between them in the horizontal and the vertical direction. Fig. 1 shows a three-dimensional view of the logical segmentation of the detector module.

The Level 1 trigger ( $T_{1S_M}$ ) signal for a horizontal layer of the segment is the OR of the  $T_{1M}$  signals from the constituent RPCs of that layer. Thus, there will be four  $T_{1S_M}$  ( $M = 1, 2, 3, 4$ ) signals per plane corresponding to each layer of a segment.

The Level 2 trigger ( $T_{2S_{M \times N/P}}$ ) signal for a segment should satisfy the trigger criterion  $M \times N/P$  and each segment will generate one  $T_{2S_{M \times N/P}}$  signal per plane for a particular trigger criterion. The  $M \times N/P$  chance rate for a  $T_{1S_M}$  rate of  $R_M$  Hz and coincidence window of  $T$  seconds is given by [7],

$$r_{M \times N/P} = C \cdot (NR_M^N T^{N-1}) \text{ Hz}, \quad C = \text{total no. of combinations} \quad (3)$$

The Level 3 trigger ( $T_{3S}$ ) signal for a segment is the OR of the  $T_{2S_{M \times N/P}}$  signals of that segment for a set of trigger criteria involving

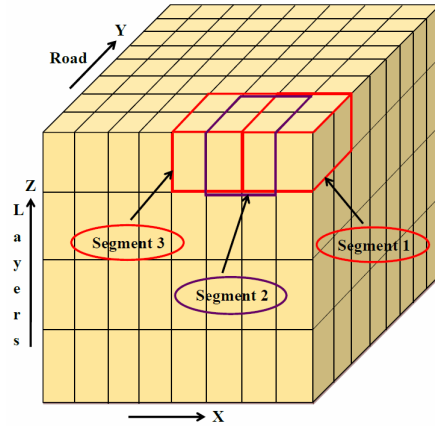


Figure 1: Three-dimensional view of logical segmentation of the detector module with overlap between the adjacent segments.

different combinations of  $M$  and  $N$ . Hence each segment will have two Level 3 trigger signals,  $T3S_X$  and  $T3S_Y$ , for the  $X$  and the  $Y$  plane respectively.

#### 4.3.3 Module Level

The global trigger ( $GT_X$  and  $GT_Y$ ) signal for the  $X$  and the  $Y$  plane is the OR of the  $T3S_X$  and the  $T3S_Y$  signals respectively, from all the constituent segments of the module. The global trigger ( $GT$ ) signal for the detector module is obtained as the OR of the  $GT_X$  and the  $GT_Y$  signals, which initiates the data acquisition system to register the event data.

#### 4.4 Chance coincidence rates

The signal pick-up rate for all strips has been assumed to be identical and uniform. The average noise rate for an RPC strip of dimension  $200\text{ cm} \times 3\text{ cm}$  is observed to be  $200\text{ Hz}$  on the earth surface [8] and is assumed to be  $10\text{ Hz}$  in the underground<sup>1</sup>. The coincidence window is taken as  $100\text{ ns}$  for all levels of trigger generation. Table 1 shows two different sets of trigger criteria. Each set consists of multiple trigger criteria with different combinations of  $M$  and  $N$ , represented as  $M \times N / P$ .

The associated chance trigger rates have been calculated for different segment dimensions and for both sets of trigger criteria, as shown in Table 2, and are found to be acceptable for an optimal combination of

<sup>1</sup> The RPC noise rate in the underground, as reported by the OPERA experiment, at a depth of  $1.4\text{ km}$  and using RPCs of area  $3.2\text{ m}^2$ , is  $17\text{ Hz/m}^2$  [9]. The rock overburden for the INO site is similar to that of OPERA and RPCs of area  $4\text{ m}^2$  will be used [6]. Hence, the underground noise rate for the ICAL RPCs can be safely assumed to be within 10 times that of the OPERA RPCs, i.e.,  $170\text{ Hz/m}^2$ . This amounts to a pick-up rate of about  $10\text{ Hz}$  for an RPC strip of dimension  $200\text{ cm} \times 3\text{ cm}$ .

Trigger criteria Set 1	1x5/8	2x4/8	3x3/8	4x2/8
Trigger criteria Set 2	1x4/8	2x3/8	3x2/8	

Table 1: Two different sets of trigger criteria.

the trigger parameters. It is observed that loosening the trigger criteria by a single layer leads to substantial increase in the chance trigger rates. This is because  $N$  comes in the exponent while calculating the  $M \times N / P$  chance rate (Eq. 3) and hence a small change in  $N$  causes a significant variation in the chance trigger rate.

Segment dimension	Segments	Rates for trigger criteria Set 1		Rates for trigger criteria Set 2	
		Surface (Hz)	Underground (Hz)	Surface (Hz)	Underground (Hz)
4m x 4m x 4m	196	87	$2.7 \times 10^{-5}$	$1.4 \times 10^4$	$8.5 \times 10^{-2}$
6m x 6m x 6m	108	$3.7 \times 10^3$	$1.1 \times 10^{-3}$	$2.6 \times 10^5$	1.6
8m x 8m x 8m	50	$4.5 \times 10^4$	$1.4 \times 10^{-2}$	$1.8 \times 10^6$	11.1

Table 2: Chance trigger rates on the surface and underground for different sets of trigger criteria and different segment dimensions.

#### 4.5 Trigger simulation framework

A simulation framework has been developed in order to determine the trigger efficiency of the proposed scheme for different events of interest for the ICAL detector. Muon events as well as neutrino events have been studied. The simulation package based on GEANT4 [10] and ROOT, developed in order to study the physics potential of the ICAL detector, has its own Monte-Carlo event generator using which muon events have been generated while Nuance [11] has been used for generating neutrino events, over a wide energy range and different incident directions. These events are simulated using the INO-ICAL simulation code and the output of the digitization stage, which provides hit position information in the detector in the same format as that which will be available from the detector data acquisition system, has been used as the input for the analysis.

The algorithm to determine whether an event has satisfied the trigger criteria has been developed in compliance with the hierarchy of the proposed trigger scheme. The trigger efficiency  $\eta$  is defined as,

$$\eta = \frac{N_E}{N_T} \quad (4)$$

where  $N_E$  is the number of events satisfying the trigger criteria and  $N_T$  is the total number of events, and is determined for the trigger criteria Set 1 (Table 1) and the segment size of 4 m x 4 m x 4 m.

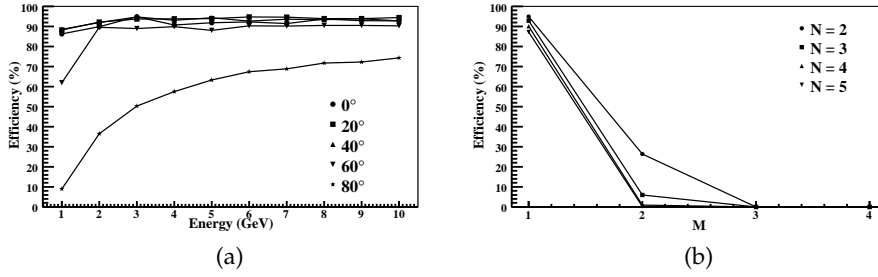


Figure 2: (a) Trigger efficiency vs. energy for muon events of energy 1 to 10 GeV and (b) trigger efficiency vs. trigger parameters (M, N) for muon events of energy 1 GeV and incident direction  $10^\circ$ .

#### 4.5.1 Muon events

Muon events in the energy range of 1 to 10 GeV with the incident direction varying from  $0^\circ$  to  $90^\circ$  have been analyzed. Fig. 2(a) shows the variation of trigger efficiency with muon energy for incident directions  $0^\circ$ ,  $20^\circ$ ,  $40^\circ$ ,  $60^\circ$  and  $80^\circ$ . The efficiency increases with the increase in energy because a particle with higher energy traverses a longer path through the detector and therefore has a greater probability of satisfying the trigger criteria. Since the particles incident at a large angle traverse lesser number of layers, their chance of satisfying the trigger criteria is lower and hence the efficiency deteriorates even at higher energy for larger angles of incidence. The variation of trigger efficiency as a function of different combinations of the trigger parameters M and N is shown in Fig. 2(b). It is evident that in case of muon events, the efficiency is dominated by the 1-Fold and the 2-Fold criteria. The trigger efficiency is found to remain almost unchanged with variations in other trigger parameters like P and segment dimensions for muon events as well as neutrino events.

#### 4.5.2 Charged current neutrino events

Charged current neutrino events in the energy range of 1 to 10 GeV with the incident direction varying from  $0^\circ$  to  $90^\circ$  have been studied. Fig. 3(a) shows the trigger efficiency varying as a function of neutrino energy for incident directions  $0^\circ$ ,  $20^\circ$ ,  $40^\circ$ ,  $60^\circ$  and  $80^\circ$ . The efficiency clearly goes up with the increase in energy and comes down for larger incident angles. The variation of trigger efficiency for different combinations of the trigger parameters M and N is shown in Fig. 3(b). The contribution of trigger criteria with  $M > 2$  seems to be significant for charged current neutrino events in comparison with muon events (Fig. 2(b)). This is due to the hadron shower produced as a result of the interaction which satisfies the 3-Fold and the 4-Fold trigger criteria.

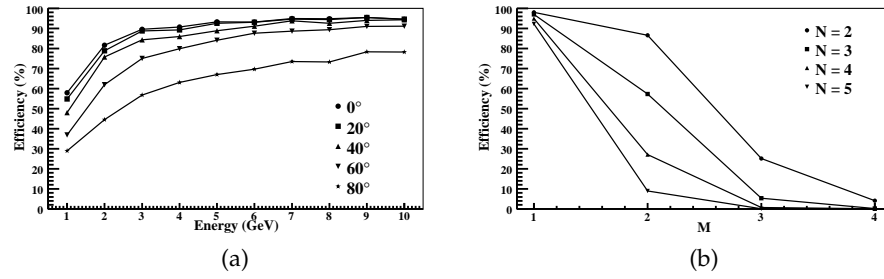


Figure 3: (a) Trigger efficiency vs. energy for charged current neutrino events of energy 1 to 10 GeV and (b) trigger efficiency vs. trigger parameters ( $M$ ,  $N$ ) for charged current neutrino events of energy 5 GeV and incident direction  $10^\circ$ .

Hence, the simulation results provide a good assessment of the detection efficiency of the trigger scheme for the events of interest for the ICAL detector and also help to understand the nature of variation of trigger efficiency as a function of the trigger parameters.

#### 4.6 Trigger module for ICAL prototype detector

The hardware implementation of the trigger scheme is initiated by designing an FPGA-based trigger module for the prototype of the ICAL detector. The prototype detector (without the magnet) consists of 12 layers of  $1\text{ m} \times 1\text{ m}$  RPCs and is continuously tracking cosmic ray muons [12]. The trigger system for the prototype detector has a hierarchical structure conforming to the proposed ICAL trigger scheme. The Level 0 and the Level 1 trigger signals are produced in the front-end electronics [13]. The Final Trigger Module (FTM) receives the Level 1 trigger signals as input and generates the final trigger signal which invokes the data acquisition system to register the event data.

##### 4.6.1 The design

The architecture of the FTM has been designed in VHDL with an Altera Cyclone FPGA (EP1C20F400C6) [14] as the target device. The CAEN V1495 General Purpose Module [15] is programmed with the design logic and is used as the FTM. Due to the input port constraints of the V1495 board, the trigger logic consists of a set of two trigger criteria ( $1 \times 5/8$  and  $2 \times 4/8$ ). The logic for detecting the coincidence of the Level 1 trigger signals has been implemented following the classical look-up table based approach. The advantage of using such technique is that the inner hardware remains same irrespective of the input pattern which ensures that the processing time does not vary with the change in input. The look-up table based trigger logic has

been implemented utilizing the block RAMs inside the FPGA. The design of the FTM is schematically shown in Fig. 4.

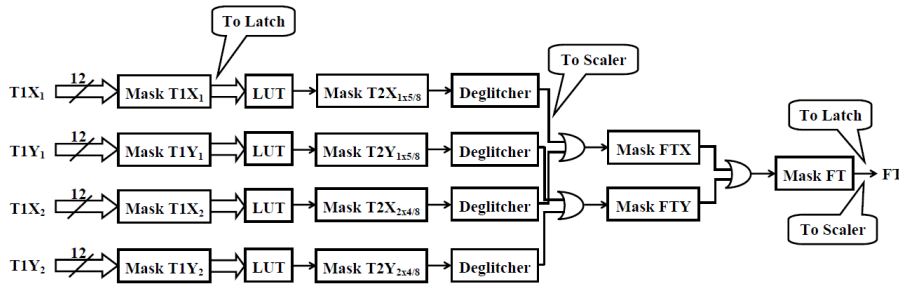


Figure 4: Schematic diagram of the design of the Final Trigger Module for the ICAL prototype detector.

There are user programmable registers using which the Level 1 trigger signal from any layer or any intermediate coincidence signal can be selectively masked by the user. The deglitching circuit removes glitches, if present, from the output signal of the FTM. The rates of the coincidence signals as well as the final trigger signal are recorded using built-in scalers. The Level 1 trigger signals and the final trigger signal are also latched internally, which may be useful for debugging and commissioning the module.

#### 4.6.2 Performance validation

In the first step, the FTM is used to generate the trigger for the prototype detector. The event data recorded is analysed offline to look for false triggers, i.e., the events for which the hit pattern does not satisfy the trigger criteria but trigger is generated by the FTM. The fraction of false triggers should be as low as possible. Under the normal situation, the noise level of the detector is well below the discriminator threshold level ( $\sim 20$  mV) and the average signal pick-up rate per RPC strip ( $100$  cm  $\times$   $3$  cm) is about  $60$  Hz. The system is said to be stable and the false trigger rate is found to be less than  $1\%$ , under such a scenario. However, occasionally, the external electromagnetic interference (EMI) elevates the ground level of the detector and the noise level becomes high enough to cross the discriminator threshold. The RPC noise rate goes up drastically in such a situation, resulting in an average strip pick-up rate of about  $1$  MHz. The false trigger rate goes up to about  $8 - 10\%$  for such a noisy system.

The next step is to check for the fraction of missed events, i.e., the events whose hit pattern satisfy the trigger criteria but are missed by the FTM and hence are not recorded by the data acquisition system. It is desirable to have the fraction of missed triggers as low as possible, especially for a low event rate experiment like ICAL. In order to determine the missed trigger rate for the FTM, the trigger signal for the data acquisition system is generated independently using a set of

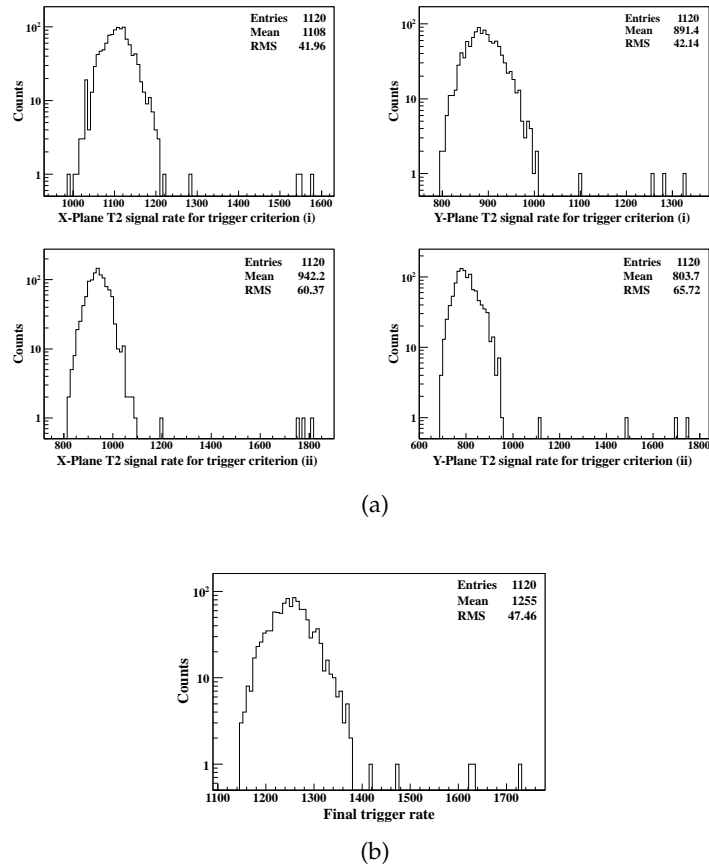


Figure 5: Rates for (a) the coincidence signals and (b) the final trigger signal of the FTM for a counting period of 10 seconds.

scintillator paddles. The data acquisition system records the event data on receiving a paddle trigger. The data is analysed offline to check for events with sufficient hits to satisfy the trigger criteria for which trigger was not generated by the FTM. The response of the FTM for an event is obtained from the latched final trigger signal corresponding to that event. The missed trigger rate is observed to be about 0.01%.

The rates for the four coincidence signals and the final trigger signal, as obtained from the FTM scalars, are shown in Fig. 5(a) and Fig. 5(b) respectively, for a counting period of 10 seconds. The final trigger signal is the combination of all the coincidence signals and hence has higher rate compared to the individual coincidence signals. All the plots show a few counts with values much higher than the mean value which may be attributed to the occasionally high chance coincidence rate as a result of correlated noise.

Hence, the trigger module is working satisfactorily in the prototype detector, with negligible fraction of missed triggers and false triggers when the system is operating in stable condition. The performance validation of the trigger module offers a proof of principle that such

technique can be successfully and reliably used for implementing the trigger system for the ICAL detector.

#### 4.7 Layout for implementation of the ICAL trigger system

The RPC level trigger signals are processed in the trigger section of the RPC-DAQ board where the Level 0 and the Level 1 trigger signals are formed. The next level in the implementation hierarchy is the segment trigger station, namely, the Local Trigger Module (LTM), which takes the pre-trigger signals produced by the RPC-DAQ board of each constituent RPC of the segment as input and finally generates the Level 3 or local trigger signals. The Global Trigger Module (GTM) receives the output of all the LTMs and produces the global trigger signal which is fed back to the RPC-DAQ board of each RPC of the detector module, via the LTMs, for recording the event data.

The RPC-DAQ board is mounted inside the RPC unit. The physical placement of the LTMs and the GTM should conform to the mechanical constraints associated with the detector structure in order to ensure the feasibility of implementation of the trigger scheme. Fig. 6 schematically represents a befitting way of positioning the trigger modules along with other back-end modules at one end of the detector. This placement scheme offers the maximum available physical space for the trigger modules and simultaneously adapts to the structural constraints of the detector.

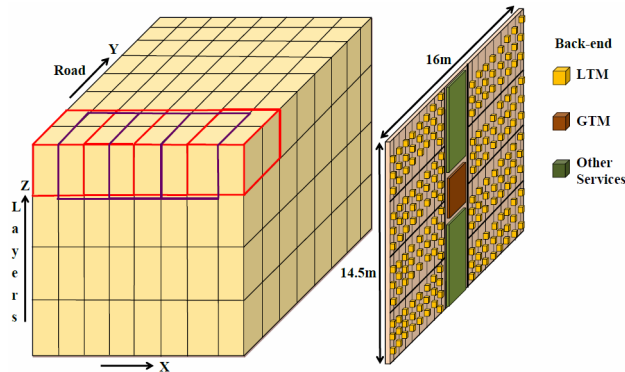


Figure 6: Schematic of the placement of the Local Trigger Modules and the Global Trigger Module at one end of the detector.

##### 4.7.1 Trigger latency estimation

Since the global trigger signal will be used for latching the event data, an estimate of the latency involved in trigger generation is essential for determining parameters like, minimum width of shaped strip pulses, full scale range of TDC etc. This is also necessary in order to fix the width of the coincidence window for trigger generation.

Various routing and processing delays involved in the generation of the local trigger signal, starting from the RPC strip signal up to the output of the LTM, are listed in Table 3. The overall latency involved in the generation of the global trigger signal in the GTM and its propagation to the RPC-DAQ board, for one module of the ICAL detector, is shown in Table 4.

Path	Delay (ns)
Cable length from RPC front-end to RPC-DAQ board : 3 m	15
Processing in RPC-DAQ board	20
Cable length from RPC-DAQ board to LTM input : 50 m	250
Track length (diagonal length for a volume of 4 m x 4 m x 1 m) : 6 m	20
Fan-out generation (max. 3 steps)	60
Cable length for fan-out : 5 m (max.)	25
Processing in LTM	50
Delay introduced for deglitching	20
Tolerance	50
<b>Net delay in local trigger generation</b>	<b>510</b>

Table 3: Various delays incorporated in local trigger generation.

Path	Delay (ns)
Generation of local trigger	510
Propagation of local trigger from LTM output to GTM input : 13 m	65
Processing in GTM	25
Propagation of global trigger from GTM output to LTM input : 13 m	65
Fan-out generation	25
Propagation of global trigger from LTM output to RPC-DAQ board : 50 m	250
Tolerance	100
<b>Global trigger latency</b>	<b>1040</b>

Table 4: Global trigger latency for one module of the ICAL detector.

Table 5 shows the maximum relative delay between the input signals of an LTM, incorporated in different stages of propagation of the trigger signal from the output of RPC-DAQ board up to the input of LTM. Hence, a coincidence window of width  $\sim 200$  ns needs to be used for the generation of the Level 2 trigger signal in the LTM.

Path	Delay (ns)
Cable length difference from RPC-DAQ board to LTM : 8 m + 4 m = 12 m	60
Track length (diagonal-length for a volume of 4 m x 4 m x 1 m) : 6 m	20
Fan-out generation (max. 3 steps)	60
Cable length for fan-out : 5 m (max.)	25
Tolerance	20
<b>Net relative delay between LTM inputs</b>	<b>185</b>

Table 5: Maximum relative delay between the LTM input signals.

#### 4.7.2 Study of LVDS transmission over long distance

Under the proposed trigger scheme, the trigger signals need to be driven over a path of length around 50 m for one module of the ICAL detector. The LVDS standard is being preferred for transmitting the trigger signals because of the advantages offered by LVDS, like high speed, low EMI and less cost, in comparison with other signal standards. However, it also needs to be ensured that the signal characteristics are preserved well after being transmitted over such a long distance.

A study has been undertaken by transmitting LVDS signal over different lengths of CAT5 cable and also using different input pulse widths. Fig. 7 describes the experimental set-up. The input and output signal characteristics are studied at point 1 and 2 respectively, as shown in the figure.

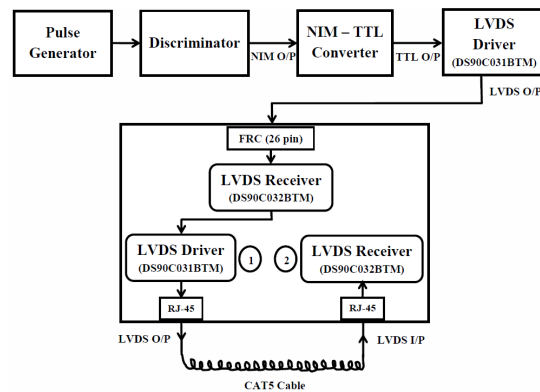


Figure 7: Experimental set-up to study LVDS transmission using different lengths of CAT5 cable and different input pulse widths.

Parameters like amplitude, pulse width, rise time, baseline and input-output delay have been studied for the signal at the transmitting as well as the receiving end. The signal amplitude remains almost unchanged and the baseline is observed to be stable. A too narrow input pulse results in the formation of triangular pulse at the output as the rise time of the output pulse, which is determined by the capacitance of the cable, becomes larger than the input pulse width. Fig. 8(a) shows the variation of the input-output delay ( $\delta$ ) as a function of the cable length ( $L$ ) for different input pulse widths. The deviation of the input-output delay from an estimated value, assuming the average delay per unit cable length to be 5 ns/m [16], is observed to be within  $\pm 2$  ns. The rise time ( $t_r$ ) of the LVDS output varying as a function of the cable length ( $L$ ) is shown in Fig. 8(b). A longer cable offers larger capacitance and hence the rise time increases with increase in the cable length. The TTL pulse, corresponding to an LVDS pulse with higher rise time, also becomes narrower.

The afore-mentioned study provides us with a good understanding of signal transmission over long distance using the LVDS standard.

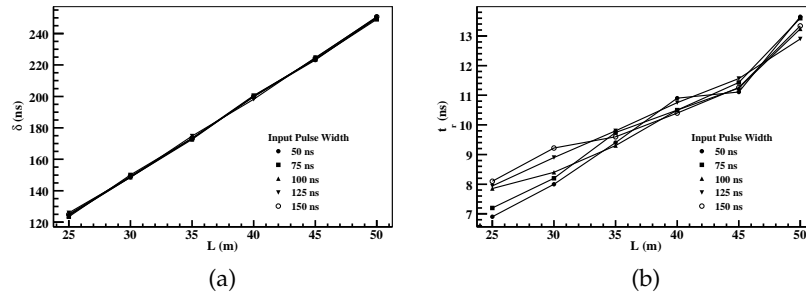


Figure 8: (a) Input-output delay vs. cable length for different input LVDS pulse widths and (b) rise time of LVDS output vs. cable length.

The results obtained ensure that this standard can be reliably used for the transmission of the trigger signals for the ICAL detector under the proposed trigger scheme.

#### 4.7.3 Delay offset calibration

The global trigger signal will be used as the reference for the measurement of timing of the RPC signals in the RPC-DAQ board. Hence, accurate estimation of the delay offset of the return-path of the global trigger signal from the output of the GTM up to the input of each RPC-DAQ board is absolutely necessary. The RPC-DAQ board has a pair of signals, one input and another output, for the purpose of delay offset calibration. The GTM generates the calibration signals which are fed to the LTMs and simultaneously used as the *Start* signals for a TDC. The delay offsets for the constituent RPCs of an LTM are calibrated sequentially using a multiplexer and a demultiplexer, both having the same select lines. The LTM receives the input calibration signal from the GTM and sends it to the RPC-DAQ board selected by the demultiplexer. The RPC-DAQ board sends an output calibration signal back to the LTM, on receiving the input calibration signal. The LTM, in turn, transmits the calibration signal received from the RPC-DAQ board to the GTM, using the multiplexer. The input calibration signals received by the GTM from the LTMs are used as the *Stop* signals for the TDC. The time-intervals between the respective *Start* and *Stop* signals, recorded by the TDC, gives an estimate of the delay offset associated with the corresponding RPC for each LTM. The delay offset for one RPC per LTM is calibrated at a time and repetitive cycles complete the calibration process for the entire detector.

#### 4.8 Design of trigger boards for the ICAL detector

A bigger prototype of the ICAL detector, known as the ICAL Engineering Module, is being built to serve as a testbench for the development of various integral components, like RPCs, magnet, gas system, front-

end electronics, data acquisition system, etc., which will be finally deployed in the ICAL detector. The trigger boards, proposed to constitute the ICAL trigger system, will be used to build the trigger system for the Engineering Module in order to authenticate their performance. The board-level designs for the LTM and the GTM have been conceived.

#### 4.8.1 *The Local Trigger Module*

Fig. 9(a) illustrates the conceptual layout of different sub-sections in the LTM board. There are 8 identical blocks, each of which receives the Level 1 trigger signal of a particular type from the constituent RPC-DAQ boards, generates the requisite number of fan-outs to take care of overlap with the adjacent segments and produces the corresponding Level 2 trigger signal. The Level 3 or local trigger signals, generated by combining the Level 2 trigger signals, are fed to the GTM. The LTM also transmits the global trigger, global clock and calibration signals from the GTM to the constituent RPC-DAQ boards. The LTM accepts user inputs to selectively mask the pre-trigger signals from any RPC or any intermediate coincidence signal. The I/O specifications of the LTM imply that the board with the requisite functionalities can be designed using a total of 10 FPGAs. The board-level schematic of the LTM, designed with a form-factor of 367 mm x 400 mm (9U) is shown in Fig. 9(b).

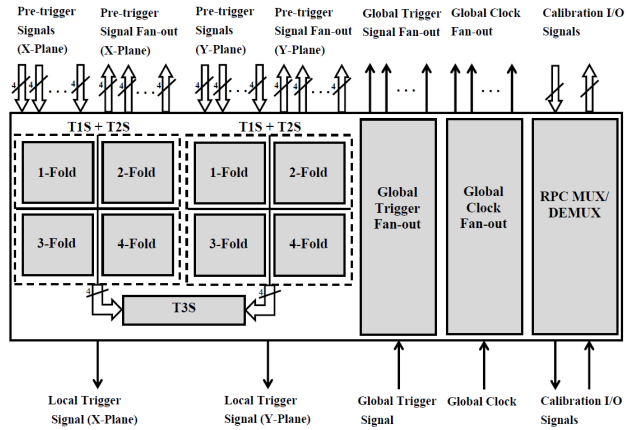
#### 4.8.2 *The Global Trigger Module*

The signal flow in the GTM is described in Fig. 10(a). The GTM combines the output of all the LTMs to produce the global trigger signal and sends it back to the LTMs. The GTM also transmits the global clock and the calibration signals to the LTMs and receives the calibration signals from the LTMs for delay offset calibration. The local trigger signal from any segment or the global trigger signal at any intermediate stage can be individually masked by the user. It is evident that the necessary functionalities of the GTM for the ICAL Engineering Module can be implemented using 1 FPGA, 1 16-channel TDC chip and 1 oscillator<sup>2</sup>. Fig. 10(b) shows the board-level schematic of the GTM, designed with a form-factor of 367 mm x 400 mm (9U).

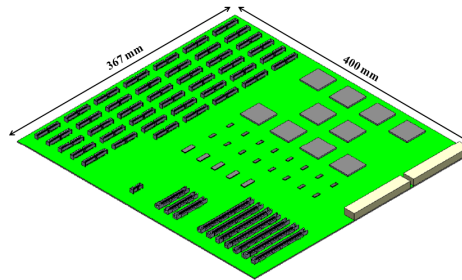
#### 4.8.3 *Component selection for design of LTM and GTM boards*

Since the trigger boards need to handle huge number of LVDS I/Os (~2000), the most important factor in selecting the suitable FPGA for designing the trigger boards is the number of LVDS I/Os supported by the chip. Other deciding factors are the logic capacity, block RAM capacity, power consumption, physical dimension and cost of the

<sup>2</sup> The GTM for the ICAL detector module will be implemented using multiple FPGAs and also multiple boards, as it needs to deal with huge number of I/O connectors.

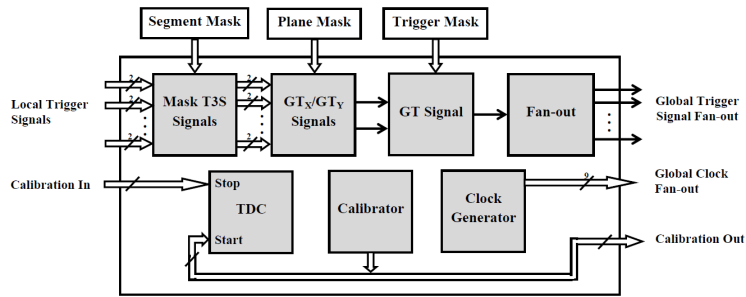


(a)

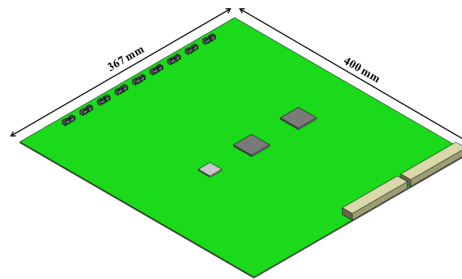


(b)

Figure 9: (a) Conceptual layout of different sub-sections in the LTM and (b) schematic of the LTM board designed with a 9U (367 mm x 400 mm) form factor.



(a)



(b)

Figure 10: (a) Signal flow in the GTM and (b) schematic of the GTM board designed with a 9U (367 mm x 400 mm) form factor.

FPGA. Different families of FPGAs from both Altera and Xilinx have been studied. Finally, the Cyclone 5 FPGA (5CEBA7F31) from Altera and the Spartan 6 FPGA (XC6SLX150FQG900) from Xilinx are found to be the most suitable candidates for designing the ICAL trigger boards.

The FPGAs can drive LVDS signals up to a length of 5 – 10 m. Since the LTM needs to drive the trigger signals over a length of 50 m for one module of the ICAL detector, LVDS drivers should be used. Appropriate driver chips have been selected to be deployed in the LTM boards.

Handling of large number of LVDS I/Os demands the use of high density connectors in the trigger boards. A survey of connectors from different vendors has been undertaken and suitable connectors are chosen. The LTM board will use different types of connectors, viz., 50 pin, 16 pin and 114 pin connectors. The relatively simpler GTM board uses only 16 pin connectors.

The trigger boards should be equipped with a back-end interface which is essential for the configuration of the LTM FPGAs to implement new trigger criteria, selective masking of signals at different levels of trigger generation, readout of information like trigger rates and latch data, etc. A standard crate structure is also essential to accommodate the trigger boards making efficient use of the available space. A commercial bus system such as VME or  $\mu$ TCA is the favourable option due to the availability of standard bus protocol and electrical and mechanical specifications.

## 5 SUMMARY AND FUTURE SCOPE

### 5.1 Summary

The INO collaboration is presently conducting a full-fledged R&D program aimed at building the 50 kton ICAL detector with the goal of studying atmospheric neutrino oscillations. The detector will be housed inside a cavern with rock overburden of more than 1 km in order to ensure minimal cosmic muon background. Considering the extremely low rate of neutrino interactions, the trigger scheme for such an experiment should achieve maximal detection efficiency for the desired events while minimizing the chance coincidence rates. The vast detector volume, consisting of 28,800 RPCs, also poses serious design challenges concerning the feasibility of hardware implementation of the trigger system.

A trigger scheme with a distributed and hierarchical architecture, which will satisfy these criteria, has been developed for the ICAL detector. Chance coincidence rates are calculated for different combinations of the trigger parameters which help to fix the criteria for an admissible chance trigger rate. A simulation framework is developed

to estimate the trigger efficiency of the scheme for the events of interest for the ICAL detector. The results ensure that substantially high detection efficiency can be obtained for the desired events under the proposed trigger scheme.

As a first step toward the implementation of the trigger scheme, an FPGA-based trigger module is designed using the look-up table based technique. The module has delivered satisfactory performance in the prototype detector with acceptable spurious trigger rate and trigger inefficiency. This ascertains the credibility of the technique in designing the ICAL trigger system.

The overall layout for the implementation of the proposed trigger scheme for the ICAL detector has been devised. A study is carried out to assess the reliability of LVDS standard in signal transmission over long distance. The results ensure the deployment of this standard in transmitting the trigger signals for the ICAL detector. The trigger latency is estimated and a technique for calibrating the delay offsets associated with the return-path of the trigger signal is proposed. The design of the trigger boards are contemplated and the design components have been selected.

### *5.2 Future scope*

The immediate plan of action includes procurement of the components chosen for designing the trigger boards, board fabrication and their performance validation in the Engineering Module. The proposed technique for delay offset calibration, which is crucial for estimating the timing of the RPC signals, also needs to be evaluated at the system level. Another important goal is to accomplish the integration of the trigger system with the ICAL detector system. This includes routing of the pre-trigger signals from the RPC-DAQ boards to the LTMs, interconnection between adjacent LTMs and between the LTMs and the GTM and the propagation of the global trigger signal from the GTM to the RPC-DAQ boards. A successful system integration would cater to the physical constraints associated with the detector structure without hindering the functionalities of the trigger system.

## LIST OF FIGURES

---

- Figure 1 Standard Model of Particle Physics with 12 fermions and 5 bosons. The mass (in eV), electric charge and spin of each particle are shown at the top left, top right and bottom right corners respectively. 5
- Figure 2 The normal (left) and inverted (right) mass hierarchy for neutrinos. The coloured bands represent the respective contributions of the flavour components in the mass eigen states. 8
- Figure 3 Neutrino fluxes of different origins as a function of energy. 12
- Figure 4 Schematic diagram of the ICAL detector module (16 m x 16 m x 14.5 m) with top view of the magnet coils. 23
- Figure 5 Neutrino-induced charged current and neutral current interactions producing muon and/ or hadrons. 25
- Figure 6 Hierarchy of the trigger scheme and the signals associated with each level of trigger generation. 30
- Figure 7 Formation of Level 0 trigger signals by combining signals from every 8th and 16th strip out of 64 pick-up strips per RPC plane. 32
- Figure 8 Horizontal segmentation pattern for  $H_{SX} = 2$ ,  $H_{SY} = 2$  with overlap between adjacent segments. Overlap along only the X direction is shown here and similar overlap exists in the Y direction as well. 34
- Figure 9 Logical segmentation of the detector module with overlap between adjacent segments. Overlap along only the X direction is shown here and similar overlaps exist in the Y and the Z directions as well. 35
- Figure 10 Two different sets of trigger criteria. Each set consists of multiple trigger criteria with different combinations of M and N, represented as MxN/P. 37

- Figure 11 Diagonal track through a segment hitting RPC B in the top layer and RPC C in the bottom layer. The trigger scheme caters for such events as the  $T1S_M$  signal for a particular layer of a segment is the OR of the  $T1_M$  signals from all the constituent RPCs of that layer. 37
- Figure 12 Complete flow of generation of the global trigger signal from the RPC strip signals through different levels of trigger generation. 40
- Figure 13 Hit position information obtained from the digitization output of the INO-ICAL simulation code, in the same format as that which will be available from the detector data acquisition system. 43
- Figure 14 Two-dimensional and three-dimensional display of a neutrino induced event. 44
- Figure 15 Analysis algorithm to determine whether an event has satisfied the trigger criteria. 45
- Figure 16 Trigger efficiency vs. energy for muon events of energy 1 to 10 GeV and incident direction  $0^\circ$ ,  $20^\circ$ ,  $40^\circ$ ,  $60^\circ$ ,  $80^\circ$ . The efficiency increases with energy and comes down for larger incident angles. 46
- Figure 17 Trigger efficiency vs. trigger parameters ( $M$ ,  $N$ ) for muon events of energy 1 GeV and incident direction  $10^\circ$ . Rest of the trigger parameters are fixed as  $P = 8$ ,  $H_{SX} = 2$ ,  $H_{SY} = 2$ ,  $V_S = 40$ . The trigger efficiency for muon events is dominated by the 1-Fold and the 2-Fold criteria. 46
- Figure 18 Trigger efficiency vs. trigger parameters ( $P$ ,  $H_{SX}$ ,  $H_{SY}$ ,  $V_S$ ) for muon events of energy 1 GeV and incident direction  $10^\circ$ . The trigger efficiency is independent of these parameters. 47
- Figure 19 Trigger efficiency vs. trigger parameter  $P$  for muon events of energy 1 GeV and incident direction  $10^\circ$  and for different values of detector efficiency. Rest of the trigger parameters are fixed as  $M = 1$ ,  $N = 5$ ,  $H_{SX} = 2$ ,  $H_{SY} = 2$ ,  $V_S = 40$ . The variation is observed to be minimal ( $\sim 1\%$ ). 47
- Figure 20 Trigger efficiency vs. energy for charged current neutrino events of energy 1 to 10 GeV and incident direction  $0^\circ$ ,  $20^\circ$ ,  $40^\circ$ ,  $60^\circ$ ,  $80^\circ$ . The efficiency goes up with energy and comes down for larger incident angles. 48

- Figure 21 Trigger efficiency vs. trigger parameters ( $M$ ,  $N$ ) for charged current neutrino events of energy 5 GeV and incident direction  $10^\circ$ . Rest of the trigger parameters are fixed as  $P = 8$ ,  $H_{SX} = 2$ ,  $H_{SY} = 2$ ,  $V_S = 40$ . Trigger criteria with  $M > 2$  are more significant for charged current neutrino events compared to muon events. 49
- Figure 22 Trigger efficiency vs. energy for quasi-elastic neutrino events of energy 1 to 10 GeV and incident direction  $0^\circ$ ,  $20^\circ$ ,  $40^\circ$ ,  $60^\circ$ ,  $80^\circ$ . The efficiency is higher for higher energy and lower for larger angles of incidence. 49
- Figure 23 Trigger efficiency vs. trigger parameters ( $M$ ,  $N$ ) for quasi-elastic neutrino events of energy 5 GeV and incident direction  $10^\circ$ . Rest of the trigger parameters are fixed as  $P = 8$ ,  $H_{SX} = 2$ ,  $H_{SY} = 2$ ,  $V_S = 40$ . Trigger efficiency for quasi-elastic neutrino events is dominated by the 1-Fold and the 2-Fold trigger criteria. 50
- Figure 24 Trigger efficiency vs. energy for resonant neutrino events of energy 1 to 10 GeV and incident direction  $0^\circ$ ,  $20^\circ$ ,  $40^\circ$ ,  $60^\circ$ ,  $80^\circ$ . The efficiency goes up with energy and comes down for larger incident angles. 50
- Figure 25 Trigger efficiency vs. trigger parameters ( $M$ ,  $N$ ) for resonant neutrino events of energy 5 GeV and incident direction  $10^\circ$ . Rest of the trigger parameters are fixed as  $P = 8$ ,  $H_{SX} = 2$ ,  $H_{SY} = 2$ ,  $V_S = 40$ . Contribution of trigger criteria with  $M > 2$  appears to be slightly higher for the resonant neutrino events than that for the quasi-elastic neutrino events. 51
- Figure 26 Trigger efficiency vs. energy for deep-inelastic neutrino events of energy 2 to 10 GeV and incident direction  $0^\circ$ ,  $20^\circ$ ,  $40^\circ$ ,  $60^\circ$ ,  $80^\circ$ . The efficiency is higher for higher energy and lower for larger angles of incidence. 51
- Figure 27 Trigger efficiency vs. trigger parameters ( $M$ ,  $N$ ) for deep-inelastic neutrino events of energy 5 GeV and incident direction  $10^\circ$ . Rest of the trigger parameters are fixed as  $P = 8$ ,  $H_{SX} = 2$ ,  $H_{SY} = 2$ ,  $V_S = 40$ . Contribution of trigger criteria with  $M > 2$  is much higher for deep-inelastic neutrino events in comparison with that for quasi-elastic and resonant neutrino events. 52

- Figure 28 Trigger efficiency vs. energy for reconstructed charged current neutrino events. The trigger efficiency is greater than 95% for the reconstructed events over the entire range of energy and incident direction. 53
- Figure 29 The prototype detector with the front-end read-out electronics on either side. 56
- Figure 30 Formation of 8 Level 0 trigger signals by combining signals from every 8th strip out of 32 pick-up strips per RPC plane. 57
- Figure 31 Complete flow of generation of the final trigger signal from the RPC strip signals through different levels of trigger generation. 58
- Figure 32 Schematic of the look-up table based trigger logic implemented using the block RAMs inside the FPGA. 59
- Figure 33 Schematic diagram of the design of the Final Trigger Module. 60
- Figure 34 Schematic of the circuit used for deglitching the coincidence signals. 61
- Figure 35 Distributions of false trigger for the FTM with system operating under stable and noisy situation. 62
- Figure 36 Arrangement of scintillator paddles for trigger generation in the prototype detector. There are total 9 paddles, each of dimension 96 cm x 32 cm x 1 cm, arranged in three layers. The bottom layer of paddles is placed below the bottommost RPC, the middle layer is placed on the middle (6th) RPC and the top layer is placed on the topmost RPC. The trigger signal for the data acquisition system is generated by combining the signals from the paddles. 63
- Figure 37 Distributions of missed trigger for the FTM for two configurations of the paddle trigger. 65
- Figure 38 Rates for coincidence signals and the final trigger signal generated by the FTM. 66
- Figure 39 Layout for implementation of the ICAL trigger system and the signals associated with each level of trigger generation. 69

- Figure 40 Placement of the trigger modules under Scheme A. The LTMs are placed on the front as well as the back face of the detector, i.e., the faces located on opposite sides, perpendicular to the direction of the road. The GTM is placed along with the back-end system at one corner of the detector module. 70
- Figure 41 Placement of the trigger modules under Scheme B. The LTMs as well as the GTM are placed at one end of the detector, which offers the maximum physical space for positioning the trigger modules and also adapts to the structural constraints of the detector. 74
- Figure 42 Experimental set-up to study LVDS transmission using different lengths of CAT5 cable and different input pulse widths. The input and the output signal characteristics are studied at point 1 and 2 respectively. 78
- Figure 43 LVDS and TTL input-output pulses for a cable length of 40 m and input pulse width of 100 ns. 79
- Figure 44 LVDS and TTL input-output pulses for a cable length of 50 m and input pulse width of 25 ns. A too narrow input pulse results in the formation of triangular pulse at the output whose rise time, determined by the cable capacitance, becomes larger than the input pulse width. 80
- Figure 45 Input-output delay ( $\delta$ ) as a function of cable length ( $L$ ) for input LVDS pulse width of 100 ns. The average delay per unit cable length is about 5 ns/m. 81
- Figure 46 Variation of the input-output delay ( $\delta$ ) with cable length ( $L$ ) for different input LVDS pulse widths. 81
- Figure 47 Deviation ( $\delta_r$ ) of the input-output delay from an estimated value, assuming the average delay per unit cable length to be 5 ns/m, as a function of cable length ( $L$ ) for different input LVDS pulse widths. The maximum deviation is observed to be within  $\pm 2$  ns. 82
- Figure 48 Variation of rise time ( $t_r$ ) of LVDS output with cable length ( $L$ ). A longer cable offers larger capacitance and hence the rise time of the output signal increases with cable length. 83

Figure 49	TTL input-output pulse width difference ( $\Delta_{PW}$ ) as a function of cable length (L). Due to the increase in the rise time of LVDS output with cable length, the output TTL pulse becomes narrower and hence the difference goes up. 83	
Figure 50	Proposed technique for delay offset calibration.	84
Figure 51	Schematic diagram of the ICAL Engineering Module (8 m x 8 m x 2 m) with top view of the magnet coils. 88	
Figure 52	Three-dimensional view of the logical segmentation of the ICAL Engineering Module with overlap between adjacent segments. Overlap along only the X direction is shown here and similar overlaps exist in the Y and the Z directions as well. 89	
Figure 53	Signal flow and conceptual layout of different sub-sections in the LTM. 92	
Figure 54	Scheme for interconnecting and feeding input signals to the LTMs. 94	
Figure 55	Signal flow in the GTM. 95	
Figure 56	Schematic of the LTM boards of two types, designed with a 9U (367 mm x 400 mm) form factor, showing the design components like the FPGAs, LVDS driver and fan-out chips, I/O and VME connectors. 102	
Figure 57	Schematic of the GTM board designed with a 9U (367 mm x 400 mm) form factor, showing the design components like the FPGA, TDC and oscillator chips, I/O and VME connectors. 103	

## LIST OF TABLES

---

Table 1	Best-fit values of the $3\nu$ oscillation parameters derived from global analyses of the current neutrino oscillation data, excluding the results from Daya Bay and RENO experiments. At present, no experimental information are available on the Dirac and the Majorana phases. 20
Table 2	Salient parameters of the ICAL detector structure. 23
Table 3	Level 0 and Level 1 chance trigger rates per RPC plane for $L = 8, 16$ . 33
Table 4	Level 1 chance trigger rates per layer of a segment for different values of $H_S$ . 35
Table 5	Level 2 and Level 3 chance trigger rates for different segment dimensions for trigger criteria set 1. 38
Table 6	Level 2 and Level 3 chance trigger rates for different segment dimensions for trigger criteria set 2. 39
Table 7	Chance trigger rates on the surface and underground for different sets of trigger criteria and different segment dimensions. The GT rates are found to be the same for segments with different values of $V_S$ but having a fixed value of $H_S$ . A comparison of the chance trigger rates for the trigger criteria of set 1 and set 2 indicates that loosening the trigger criteria by a single layer leads to a substantial increase in the chance trigger rates. 41
Table 8	Various delays incorporated in local trigger generation under Scheme A. The tolerance is taken as $\sim 10\%$ of the total delay. 71
Table 9	Local trigger latency considering no LTMs for the segments lying across the half-road boundary and no interconnection between the segments lying on opposite halves of the road. 72
Table 10	Local trigger latency assuming that it is possible to handle the segments lying across the half-road boundary using respective LTMs, overcoming the mechanical constraints. 72
Table 11	Global trigger latency under Scheme A. 73

Table 12	Maximum relative delay between LTM input signals under Scheme A, which implies that a coincidence window of width $\sim 200$ ns needs to be used for the generation of the Level 2 trigger signal. 74
Table 13	Various delays incorporated in local trigger generation under Scheme B. 75
Table 14	Local trigger latency under Scheme B. 75
Table 15	Global trigger latency under Scheme B. 76
Table 16	Maximum relative delay between LTM input signals under Scheme B, which indicates that the generation of the Level 2 trigger signal will require a coincidence window of width $\sim 200$ ns. 77
Table 17	Different cable lengths and input pulse widths used in the study. 77
Table 18	Comparative study of the structural parameters of the Engineering Module and the ICAL detector. 88
Table 19	Comparison of the trigger system parameters of the Engineering Module with those of the ICAL detector. 89
Table 20	Various delays incorporated in local trigger generation for the Engineering Module. The tolerance is taken as $\sim 10\%$ of the total delay. 90
Table 21	Global trigger latency for the Engineering Module. 91
Table 22	Maximum relative delay between LTM input signals for the Engineering Module which implies that a coincidence window of width $\sim 200$ ns is required for the generation of the Level 2 trigger signal. 91
Table 23	Categorization of the LTMs into two types based on functionality. 95
Table 24	I/O specifications for the LTM. The quoted figures represent the maximum requirement. 96
Table 25	I/O specifications for the GTM. 97
Table 26	List of suitable FPGAs from different families of Altera and Xilinx for designing the LTM and the GTM boards. 99
Table 27	LVDS driver and fan-out chips selected for designing the type I LTM board. 100
Table 28	Different types of high density connectors selected for designing the trigger boards. 100
Table 29	Design components for the two types of LTM boards. 101

## ACRONYMS

---

LEP	Large Electron Positron collider
CERN	European Organization for Nuclear Research
LHC	Large Hadron Collider
SSM	Standard Solar Model
GZK	Greisen-Zatsepin-Kuzmin
CMB	Cosmic Microwave Background
GALLEX	Gallium Experiment
GNO	Gallium Neutrino Observatory
SAGE	Soviet American Gallium Experiment
Kamiokande	Kamioka Nucleon Decay Experiment
PMT	Photomultiplier tube
SNO	Sudbury Neutrino Observatory
CC	charged current
NC	neutral current
ES	elastic scattering
KamLAND	Kamioka Liquid Scintillator Anti-Neutrino Detector
GPS	Global Positioning System
MINOS	Main Injector Neutrino Oscillation Search
NuMI	Neutrinos at the Main Injector
TPC	Time Projection Chamber
INO	India-based Neutrino Observatory
ICAL	Iron Calorimeter
RPC	Resistive Plate Chamber
EMI	electromagnetic interference
GUI	Graphical User Interface
FPGA	Field Programmable Gate Array

VME VERSA-Module Eurocard

FTM Final Trigger Module

VHDL VHSIC Hardware Development Language

RAM Random Access Memory

LTM Local Trigger Module

GTM Global Trigger Module

TDC Time to Digital Converter

LVDS Low Voltage Differential Signaling

TTL Transistor-transistor logic

GPU Graphics Processing Unit

Part I

INTRODUCTION



## NEUTRINO PHYSICS

---

A brief overview of the history of neutrino physics marks the beginning of this chapter. The salient features of this fundamental particle, as predicted in the Standard Model of particle physics, are illustrated and the concept of neutrino oscillation is introduced. The various sources of neutrinos are described and the major experiments that have yielded crucial results in the field of neutrino oscillation are reviewed. Finally, the open questions in this arena of particle physics are summarized and the physics potential of the Iron Calorimeter detector, proposed to be built by the India-based Neutrino Observatory collaboration, is discussed.

*Chapter  
summary*

### 1.1 HISTORY OF NEUTRINO

The history of weak interactions dates back to the discovery of radioactivity of uranium by Becquerel in 1896. The continuous energy spectrum in nuclear  $\beta$ -decay, first demonstrated by Chadwick in 1914, was in contradiction with the discrete energy spectrum expected in a two-body decay. The observation was subsequently confirmed by other experiments [17] and failed attempts in ascribing the missing energy to neutral  $\gamma$  rays [18] even led N. Bohr speculate abandoning the conservation laws of energy and momentum in subatomic processes [19]. However, in 1930, W. Pauli postulated that the beta decay might be a three-body decay where an electrically neutral and extremely light particle was being emitted from the decaying nucleus which was escaping detection and was sharing the final energy with the electron [2]. The sacred conservation laws were thus safeguarded from facing a serious challenge. The term 'neutrino' was coined by E. Fermi who formulated an effective quantum theory of the  $\beta$ -decay in 1934 [20][21].

*The  $\beta$ -decay  
puzzle*

Although Fermi's theory was remarkably successful, the experimental observation of neutrino seemed impossible as H. Bethe and R. Peierls predicted that the strength of neutrino interactions ( $\sigma \sim 10^{-44} \text{ cm}^2$ ) is about 20 orders of magnitude lower than that of typical nuclear reactions [22]. Nevertheless, F. Reines and C.L. Cowan finally succeeded in detecting neutrino through a series of experiments in 1956 [3][4], using the inverse  $\beta$ -decay process.

*First experimental  
detection of electron  
antineutrino*



They used a huge flux of antineutrino from a nuclear reactor. Prompt photon signals coming from positron annihilation along with delayed

photon signals originating from neutron capture on cadmium in the liquid scintillator detector provided the detection signature.

*Lepton flavour  
conservation*

Another intriguing question for the physicists in the 1960's was whether the neutrinos emitted from the primary decay modes of  $\pi^\pm$  mesons were identical to those produced from  $\beta$  decay. Had they been the same, the branching ratio of the decay process shown in Eq. 1.2 would be several orders of magnitude higher than the experimental upper bound [23].

$$\mu \rightarrow e + \gamma \quad (1.2)$$

*Discovery of muon  
and tau neutrinos*

This implied a new conservation law which assigns unique conserved lepton number to each lepton family, and thus forbidding the above decay process. It also suggested that the neutrinos produced as a result of  $\pi^\pm$  decay were different from those emitted during  $\beta$  decay. This assumption was experimentally verified by L.M. Lederman et al., in 1962 [24]. They detected muon neutrino  $\nu_\mu$  produced from the decay of charged pions in the first high-energy accelerator neutrino experiment at the Brookhaven National Accelerator Laboratory.

The tau neutrino  $\nu_\tau$  was naturally expected to exist after the discovery of the  $\tau$  lepton and the observation of missing energy in  $\tau$  decay by M. Perl et al. in 1975 [25]. The direct experimental detection of  $\nu_\tau$  was finally accomplished in 2000 by the DONuT collaboration [26].

This provided the complete picture of the three lepton families, consisting of three charged leptons ( $e, \mu, \tau$ ) and the associated neutral leptons ( $\nu_e, \nu_\mu, \nu_\tau$ ). Precise estimation of the invisible decay width of the Z boson by the LEP experiments at CERN in 1989 [27][28][29][30] also restricted the number of active neutrino species, with mass less than half the mass of Z, to three.

## 1.2 NEUTRINO IN THE STANDARD MODEL

*12 fermions and  
5 bosons*

The Standard Model of Particle Physics is a theoretical framework developed in the 1970s [31][32][33] containing a description of the elementary particles and the fundamental forces of nature, excluding gravity. Fig. 1 illustrates the intrinsic building blocks of the universe comprising 12 spin-1/2 fermions (6 quarks and 6 leptons) and their antiparticles, which interact via 4 spin-1 gauge bosons, termed as force carriers. The fermions as well as 2 of the gauge bosons (W and Z) acquire mass through interactions with the Higgs field, the associated particle being referred to as the Higgs boson, predicted to be a massive and scalar particle. The existence of all the particles (except Higgs boson) have been proved experimentally and the latest results from the LHC experiments at CERN [34][35] strongly indicate the discovery of a *Higgs-like* boson.

The fermions are grouped in three generations, with the lightest and the most stable particles making up the first generation and the

heavier and less stable particles belonging to the second and the third generations. All stable matter in the universe are made up of the first generation particles and the heavier particles quickly decay to the next most stable level.

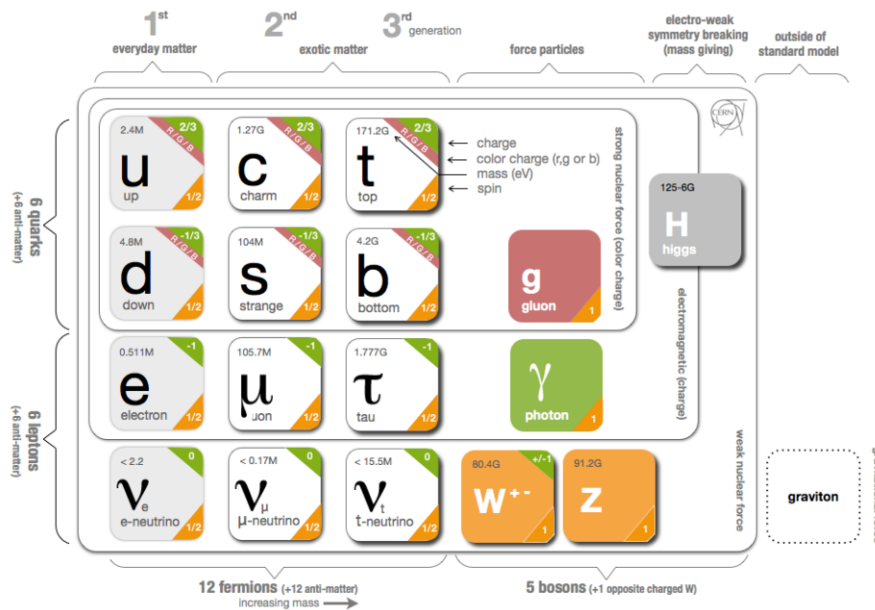


Figure 1: Standard Model of Particle Physics with 12 fermions and 5 bosons. The mass (in eV), electric charge and spin of each particle are shown at the top left, top right and bottom right corners respectively. The figure is adopted from Ref. [36].

Interactions between the elementary particles are governed by four fundamental forces, namely, the strong force, the weak force, the electromagnetic force and the gravitational force. They work over different ranges and have different strengths. Gravity is the weakest of all the forces but has an infinite range. The electromagnetic force also has infinite range but it is many times stronger than gravity. The weak and strong forces are effective only in the subatomic range. As the name indicates, the strong force is the strongest among all the fundamental interactions. The fundamental forces result from the exchange of force carriers. The strong force is carried by the gluon, the electromagnetic force is mediated through the photon, and the W and Z bosons are responsible for the weak force. Gluon and photon are massless, while W and Z bosons are massive. Gravity stays beyond the scope of the Standard Model till date. The corresponding force carrier, if exists, is named graviton. Although all matter interact through gravity, its effect is negligible in the microscopic domain because of its extremely low strength.

*The fundamental forces of nature*

Quarks are the fermions carrying fractional charge and are always observed in bound state, as triplets or doublets. They primarily interact via the strong force, which results in the formation of protons, neutrons and all hadrons, and also participate in electromagnetic and

*Quarks and leptons*

weak interactions. The fermions that carry integral charge and can exist independently are called leptons. The charged leptons interact electromagnetically as well as via weak interaction whereas the neutral leptons interact only weakly.

*Standard Model  
description of  
neutrinos*

Within the Standard Model, the neutrinos can interact only through weak interactions and are not sensitive to electromagnetic or strong interactions, which makes it extremely difficult to detect them experimentally. They participate in two modes of weak interactions, charged current (CC), mediated by W boson, and neutral current (NC), mediated by Z boson. All neutrinos have left-handed helicity and all antineutrinos have right-handed helicity. The Standard Model predicts the neutrinos to be massless and electrically neutral and advocates lepton flavour conservation which implies that neutrinos cannot undergo flavour transformation. The predictions of the Standard Model have been largely proved to be infallible from the experimental results. Observation of neutrino oscillation and the resultant concept of massive neutrino have therefore turned out to be the first conspicuous evidence of the Physics beyond the Standard Model.

### 1.3 NEUTRINO OSCILLATION

Neutrino oscillation is a quantum-mechanical phenomenon proposed in the late 1950s by B. Pontecarvo [37][38]. The flavour eigen states participating in the weak interaction processes are linear superpositions of the mass eigen states via a mixing matrix, called the PMNS matrix, named after Pontecarvo, Maki, Nakagawa and Sakata, who are credited with formulating the model for mixing of different neutrino flavours [39]. The coupling between the flavour and the mass eigenstates can be represented as,

$$\begin{pmatrix} \nu_e \\ \nu_\mu \\ \nu_\tau \end{pmatrix} = U \begin{pmatrix} \nu_1 \\ \nu_2 \\ \nu_3 \end{pmatrix} \quad (1.3)$$

where  $\nu_e, \nu_\mu, \nu_\tau$  are the flavour eigen states and  $\nu_1, \nu_2, \nu_3$  are the mass eigen states. The mixing matrix U is a 3x3 unitary matrix parameterized in terms of four independent variables as,

*The mixing matrix  
coupling the flavour  
and the mass eigen  
states*

$$U = \begin{pmatrix} U_{e1} & U_{e2} & U_{e3} \\ U_{\mu1} & U_{\mu2} & U_{\mu3} \\ U_{\tau1} & U_{\tau2} & U_{\tau3} \end{pmatrix} = U(\theta_{12}, \theta_{23}, \theta_{13}, \delta) \quad (1.4)$$

where  $\theta_{ij}$  is the mixing angle between the mass eigen states  $\nu_i$  and  $\nu_j$  and  $\delta$  is the phase characterizing possible CP violation.

In addition, the neutrinos can be 'Dirac' or 'Majorana' particles, identified by whether the neutrinos and the anti-neutrinos are different

or the same, respectively. For Majorana neutrinos, the mixing matrix becomes,

$$U_M = U \times \text{diag}(1, e^{i\phi_1}, e^{i\phi_2}) \quad (1.5)$$

where  $\phi_1$  and  $\phi_2$  are the Majorana phases. They do not affect neutrino oscillation.

Neutrino oscillation is feasible if the neutrino are not massless and if the mass eigenstates differ in their mass. As the neutrino propagates after being emitted from the source, the mass eigen states travel with different velocities and thereby get out of phase with each other. As a consequence, a neutrino emitted from the source in the flavour  $\alpha$ ,  $\nu_\alpha$ , is detected as a neutrino of flavour  $\beta$ ,  $\nu_\beta$ , at the detector with a certain probability which depends on the distance between the neutrino source and the detector and the energy of the neutrino. If the neutrinos were massless or if the mass eigen states were identical, they would always propagate with the same velocity and hence would never get out of phase. The phenomenon of neutrino oscillation thus leads to the perception of neutrino mass.

*Idea of massive neutrino from neutrino oscillation*

The probability of an initial neutrino  $\nu_\alpha$  of flavour  $\alpha$  and energy  $E$  being detected as a neutrino  $\nu_\beta$  of same energy but with different flavour  $\beta$ , after traversing a distance  $L$  in vacuum, is given by,

$$P_{\alpha\beta} = \delta_{\alpha\beta} - 4 \sum_{i>j} \text{Re}[U_{\alpha i}^* U_{\beta i} U_{\alpha j} U_{\beta j}^*] \sin^2 \left( \frac{\Delta m_{ij}^2 L}{4E} \right) + 2 \text{Im}[U_{\alpha i}^* U_{\beta i} U_{\alpha j} U_{\beta j}^*] \cos \left( \frac{\Delta m_{ij}^2 L}{2E} \right) \quad (1.6)$$

where  $\Delta m_{ij}^2 = m_i^2 - m_j^2$  is the mass-squared difference between the mass eigenstates  $m_i$  and  $m_j$ . Eq. 1.6 holds for vacuum. The oscillation probability is, however, drastically modified for neutrino propagating in matter where it is subjected to a potential due to coherent forward elastic scattering with the particles in the medium. Matter effect arises because of  $\nu_e$  having an extra mode of interaction in matter (both CC and NC) compared to  $\nu_\mu$  and  $\nu_\tau$  (only NC) and the consequent modification of the propagation of different flavours. Even if the mixing angle in vacuum is small, matter effects can give rise to large effective mixing angle. When the condition

*Matter effect*

$$\sqrt{2} \cdot G_F \cdot \rho_e = \frac{\Delta m^2}{2E} \cdot \cos 2\theta \quad (1.7)$$

is satisfied, where  $G_F$  is the Fermi constant and  $\rho_e$  is the electron density in matter, the mixing angle is maximal ( $\pi/4$ ) and the mechanism is known as MSW resonance [40][41].

Hence, the probability of neutrino oscillation depends on six independent parameters, viz., two independent mass-squared differences ( $\Delta m_{21}^2$  and  $\Delta m_{32}^2$ ), three mixing angles ( $\theta_{12}$ ,  $\theta_{23}$  and  $\theta_{13}$ ) and one

*Neutrino oscillation parameters*

Dirac phase ( $\delta$ ), apart from the source-detector distance, the density of matter through which it propagates and the neutrino energy. The last three factors are specific to an experiment and determine the sensitivity of the experiment. Oscillation experiments yield information on the values of the mixing angles and the mass-squared differences but not on the absolute values of neutrino masses.

Estimate of  $\Delta m_{21}^2$  and  $\theta_{12}$  can be obtained from solar neutrino experiments and hence they are commonly referred as  $\Delta m_{\text{sol}}^2$  and  $\theta_{\text{sol}}$  respectively. Similarly, atmospheric neutrino experiments provide measurements of  $\Delta m_{32}^2$  and  $\theta_{23}$  which are thus named as  $\Delta m_{\text{atm}}^2$  and  $\theta_{\text{atm}}$  respectively. However, till now, only the absolute value of  $\Delta m_{32}^2$  could be obtained from atmospheric neutrino observations and not its sign. This results in two possible mass orderings for neutrinos which are called normal ( $m_1 < m_2 < m_3$ ) and inverted ( $m_3 < m_1 < m_2$ ) mass hierarchy, as shown in Fig. 2.

Neutrino mass  
hierarchy

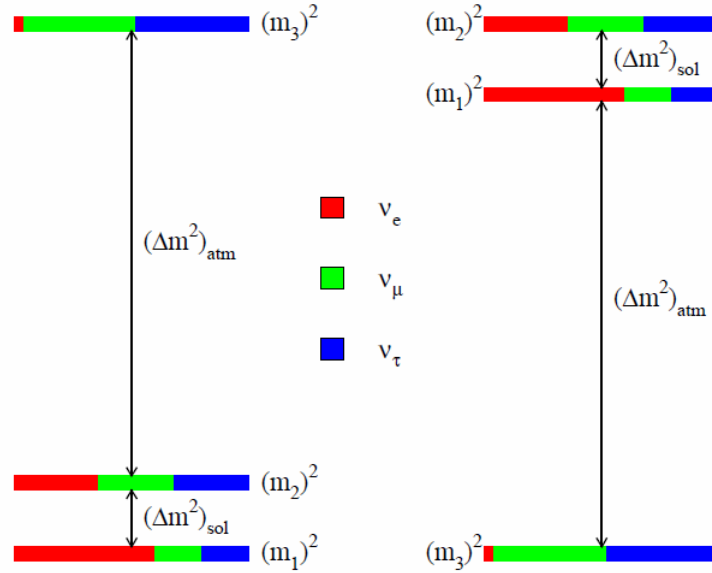


Figure 2: The normal (left) and inverted (right) mass hierarchy for neutrinos. The coloured bands represent the respective contributions of the flavour components in the mass eigen states. The figure is adopted from Ref. [42].

The absolute value of neutrino mass can be obtained from cosmological constraints and from non-oscillation experiments, like distortion of the  $\beta$ -spectra, neutrinoless double beta decay etc. Cosmological constraints on neutrino masses come from the observation of the Cosmic Microwave Background (CMB) anisotropies and from the study of large scale structures. These observations are sensitive to the sum of the three neutrino masses and are dependent on cosmological models. Study of distortions of the end-point of the  $\beta$ -decay spectrum provides direct measurement of the 'effective mass' of  $\nu_e$ , which is a combination of the mass eigenvalues and the mixing angles. Tritium  $\beta$ -decay experiments, having the lowest Q-value of all known  $\beta$ -decays,

Measurement of  
absolute mass of  
neutrino

are the most sensitive to such measurements and have obtained an upper limit of 2.2 eV on the  $\nu_e$  mass [43][44]. Similarly, kinematics of charged pion decay and  $\tau$ -decay provide information about the effective masses of  $\nu_\mu$  and  $\nu_\tau$  respectively. Neutrinoless double beta decay is the most promising avenue to identify the Dirac or Majorana nature of neutrinos, since this process is possible only for Majorana neutrinos. The decay rate is proportional to the effective Majorana mass of  $\nu_e$ . When coupled with the input from oscillation results, detection of such process would help to distinguish the two possible mass hierarchies.

#### 1.4 SOURCES OF NEUTRINOS

Neutrinos are emitted from a variety of sources, both natural and artificial, spanning over a wide energy range. Due to their extremely low interaction cross-section, the neutrinos serve as excellent messengers of the characteristic features of the source.

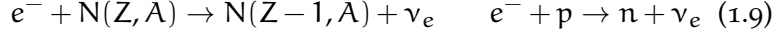
- **Relic neutrinos** – As predicted by the Standard Cosmological Model, relic neutrinos are an important product of the Big Bang. The relic neutrinos had decoupled from matter at a much earlier time (1 sec) than the CMB ( $3 \times 10^5$  years), and hence are, in principle, better probes to the early Universe. They are the second most abundant particle in the Universe with a number density of 336 neutrinos per  $\text{cm}^3$ . However, the kinetic energy of the relic neutrinos is predicted to be only about  $10^{-4}$  eV at the current epoch. This implies an extremely small interaction cross-section ( $\sigma \sim 10^{-64} \text{ cm}^2$ ), rendering the experimental detection with today's technology, an extremely difficult task.
- **Solar neutrinos** – According to the Standard Solar Model, energy inside the Sun is emitted by the exothermal thermonuclear fusion of hydrogen to helium, as shown below.



The energy released per  ${}^4\text{He}$  fusion process is about 26.7 MeV, out of which only 2% is transferred to the two  $\nu_e$  and the rest is emitted in the form of thermal energy. The energy production mechanism inside the Sun is divided into several sub-cycles, viz., the pp,  ${}^7\text{Be}$ , pep,  ${}^8\text{B}$ , hep and CNO cycle, as described in the Standard Solar Model (SSM) developed by Bahcall [45]. The total solar neutrino flux on the Earth is about  $6.5 \times 10^{10} \text{ cm}^{-2}\text{s}^{-1}$ , which offers a unique direct probe of the interior of the Sun.

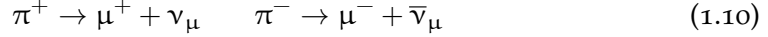
- **Supernova neutrinos** – Supernova produced by the collapse of the core of the massive stars generate huge flux of neutrinos

which carry away most of the energy of the explosion. Neutrino is emitted through electron capture of nuclei and free protons.

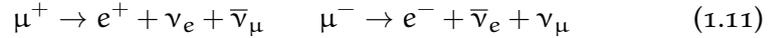


The hot core of the resultant proto-neutron star also produces neutrinos through processes like electron-positron pair annihilation, photoannihilation, electron-nucleon bremsstrahlung, nucleon-nucleon bremsstrahlung and plasmon decay. The neutrinos are the only known particles that can escape the collapsing and the extremely dense core and therefore are the exclusive source of information on the stellar evolution and explosion mechanisms. The analysis of neutrino propagation through the matter of the supernova and the Earth, combined with the observation of neutrino burst from a galactic supernova, enables us to put constraints on the neutrino mass, the mixing angle  $\theta_{13}$  and also identify whether the mass hierarchy is normal or inverted. The Supernova SN1987A is the only one of its kind to have been detected through the neutrino burst by three neutrino telescopes on Earth and has yielded pioneering results in neutrino astronomy [46][47][48].

- Atmospheric neutrinos – Cosmic ray interactions with the nuclei in the Earth's atmosphere produce atmospheric neutrinos. Primary cosmic rays, mainly composed of protons, interact with the nuclei in the atmosphere to generate secondary cosmic rays, which consist of hadrons like pions and kaons. The pions decay to produce muons and muon neutrinos.



At high energies, kaons also contribute to the production of muons and neutrinos. The muons which decay before reaching the Earth surface give rise to electrons, electron neutrinos and muon neutrinos.



Energy of the neutrinos generated through the above processes range from 100 MeV to  $10^8$  GeV. Depending on where the atmospheric neutrinos are created with respect to the position of the detector, the oscillation baselines vary from 20 to 13,000 km, thus allowing sensitivity over a broad range of the oscillation parameters.

- Ultra-high energy neutrinos – Astrophysical sources like, active galactic nuclei and gamma ray bursts, emit neutrinos at very high energy range. Extragalactic cosmic rays cannot travel more than 50 Mpc without suffering energy attenuation due to the GZK

cutoff. The neutrinos do not interact with the CMB and hence can reach the Earth from distant astrophysical sources. Moreover, being electrically neutral, neutrino trajectories cannot be bent by the interstellar magnetic fields. Thus, high-energy cosmic neutrinos serve as unique cosmic messengers complementary to photons and protons. However, due to their extremely low rate, detection of high-energy cosmic neutrino events require extraordinarily large neutrino detectors, called neutrino telescopes.

- **Geo-neutrinos** – Antineutrinos are emitted in the decay chains of radioactive isotopes, like  $^{238}\text{U}$ ,  $^{232}\text{Th}$  and  $^{40}\text{K}$ , embedded in the Earth's crust and mantle. Radioactive decay of these isotopes is one of the major sources of heat production in the Earth's core. Precise measurement of the geo-neutrino flux and spectrum provide deep insight into the Earth's chemical composition and radiogenic heat production.
- **Reactor neutrinos** – Nuclear reactors are the major sources of artificially produced neutrinos which were used for the first experimental confirmation of the existence of neutrino [3][4]. Power generation in nuclear reactor takes place through the fission of neutron-rich isotopes like  $^{235}\text{U}$ ,  $^{238}\text{U}$ ,  $^{239}\text{Pu}$  and  $^{241}\text{Pu}$ . Electron antineutrinos are produced by the chain of  $\beta$ -decays of the fission products in the energy range of 0.1 – 10 MeV. Each fission produces about 200 MeV energy with the release of 6  $\bar{\nu}_e$ s and hence a 3 GW reactor yields about  $6 \times 10^{20}$   $\bar{\nu}_e$ /sec.
- **Accelerator neutrinos** – Neutrino beam, composed mainly of muon neutrinos, is produced in particle accelerators by the decay of charged pions and kaons initially produced by a proton beam hitting a target. The mesons, being focused using a magnetic horn, enter an evacuated decay tunnel where they decay to produce muons and neutrinos. The muons and the remaining mesons are absorbed in a beam dump at the end of the tunnel, producing a neutrino beam. Focusing positive mesons produces neutrino beam while antineutrino beam can be obtained by focusing negative mesons. Semi-leptonic decays of charmed particles have also been used to produce neutrinos where a high-energy proton beam is stopped in a thick target to generate heavy hadrons. The charmed heavy hadrons decay promptly emitting equal fluxes of high-energy electron and muon neutrinos. Efforts are currently underway to build accelerator with muon storage ring where intense and high-energy neutrino beam can be obtained through decay of muons, the facility being known as neutrino factory.

Fig. 3 gives an overview of neutrino fluxes of different origins as a function of energy.

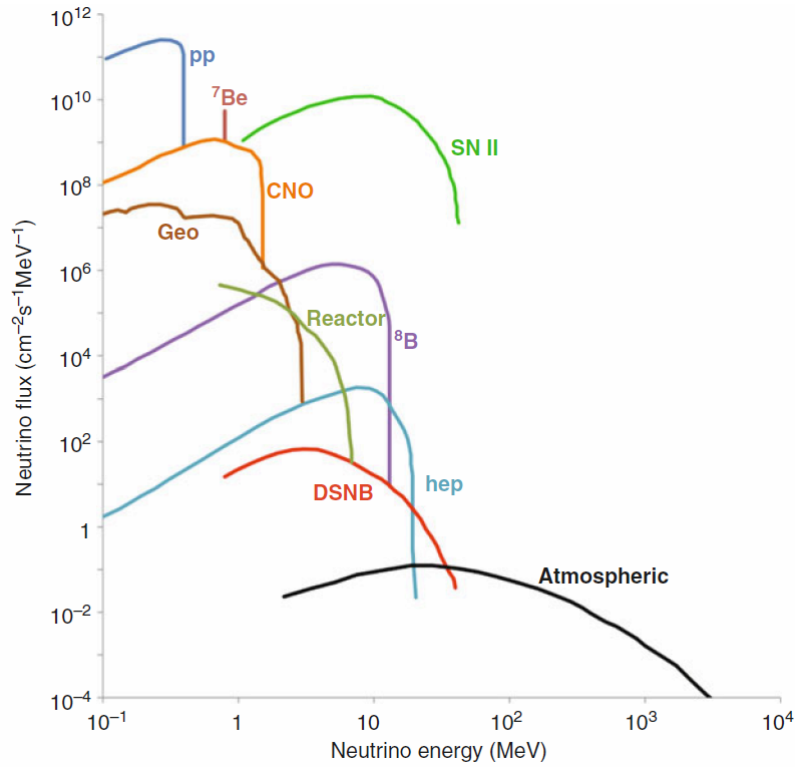


Figure 3: Neutrino fluxes of different origins as a function of energy. The figure is adopted from Ref. [5].

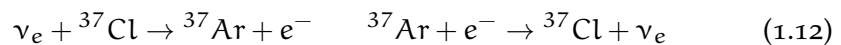
## 1.5 NEUTRINO OSCILLATION EXPERIMENTS

The first experimental detection of neutrino is highlighted in Section 1.1. Several experiments have been conducted thereafter to probe neutrinos originating from different sources and in different energy ranges. Results from such experiments have revealed fascinating information about this elementary particle and thus aided in improving our understanding of the laws of nature.

### 1.5.1 Solar neutrino experiments

The radiochemical experiment by R. Davis et al., located in the Homestake mine, USA at a depth of 1480 m, detected solar neutrinos for the first time in the 1960s [49]. The detector was a tank filled with 600 tonnes of liquid perchloroethylene ( $C_2Cl_4$ ). Solar neutrinos,  $\nu_e$ , interact with  $^{37}Cl$  nucleus producing  $^{37}Ar$  which is unstable and decays via electron capture back to  $^{37}Cl$ , emitting X-rays and Auger electrons. The  $^{37}Ar$  atoms were extracted from the tank and counted using proportional counters which detected the Auger electrons.

*Homestake  
experiment – the  
solar neutrino  
problem*



Precise measurement of the decay rate provides an estimation of the solar neutrino flux. Due to the high energy threshold (5.8 MeV) of the Cl-Ar reaction, the experiment was mainly sensitive to the high-energy  $^8\text{B}$  neutrinos. The results yielded only about one-third of the neutrino flux predicted by the SSM [50]. The flux of the  $^8\text{B}$  neutrinos constitutes a small fraction ( $\sim 9\%$ ) of the total solar neutrino flux and its predicted value is strongly dependent on the model. Hence, this observation necessitated experiments capable of detecting the pp and  $^7\text{Be}$  neutrinos, the major constituents ( $\sim 54\%$  and  $\sim 27\%$  respectively) of the solar neutrino flux.

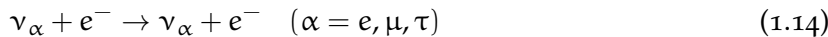
Radiochemical gallium experiments, with an energy threshold of 233 keV, turned out to be an attractive option as they provide information on the low-energy, model-independent and predominant part of the solar neutrino spectrum. Two radiochemical gallium detectors, GALLEX (later upgraded to GNO) in Gran Sasso, Italy [51][52] and SAGE in Baksan, Russia [53], became operational in the early 1990s. These experiments detected solar neutrinos through the decay of radioactive  $^{71}\text{Ge}$  produced by neutrino interaction with  $^{71}\text{Ga}$ .

*GALLEX/GNO and  
SAGE experiments*



The solar neutrino flux measured by both the experiments is about half of that predicted by the SSM [54][55]. The gallium experiments have recorded the solar  $\nu_e$  flux at the Earth which led to the determination of the solar neutrino luminosity. The results also shed light on the relative contributions of the various sub-processes to the solar luminosity and on the agreement of the thermonuclear energy production derived from the photon and the neutrino luminosities.

The Kamioka Nucleon Decay Experiment (Kamiokande) was a 3000 ton water Cherenkov detector, constructed in 1983 in the Kamioka mine, Japan under a rock cover of 1000 m, primarily aimed at the search for proton decay [56]. It was also capable of detecting solar  $^8\text{B}$  and hep neutrinos via the elastic scattering (ES) of neutrino off target electron.



The reaction is mainly sensitive to  $\nu_e$  with cross-section about 6 times than those of  $\nu_\mu$  and  $\nu_\tau$ . The Cherenkov light emitted by the recoil electron in water was detected by large number of PMTs surrounding the water target. The energy threshold was 9.3 MeV initially and was later improved to 7.5 MeV. The solar neutrino events were distinguished from the isotropic background by measuring the directional correlation of the recoil electron and the Sun. The experiment measured only half of the predicted  $^8\text{B}$  neutrino flux [57]. In 1996, the Kamiokande detector was upgraded to a 50 kton water Cherenkov detector with energy threshold of 5 MeV, called the Super-Kamiokande detector. The measured flux of  $^8\text{B}$  neutrino was less than half of the SSM flux [58]. The experiment also aimed at measuring the possible

*Kamiokande and  
Super-Kamiokande  
experiments*

day-night asymmetry in the solar neutrino flux as a result of the Earth matter effect. However, no significant asymmetry was observed.

The deficit of the observed solar neutrino flux from the SSM prediction, as evident from the results of the aforesaid experiments, became famously known as the *solar neutrino problem*.

The Sudbury Neutrino Observatory (SNO) detector is a 1000 ton heavy-water Cherenkov detector built in 1999 in the Creighton mine, Canada at a depth of 2092 m [59]. Neutrinos crossing the detector volume were detected through three different processes.

$$\text{CC : } \nu_e + \text{d} \rightarrow \text{p} + \text{p} + e^- \quad (1.15)$$

$$\text{NC : } \nu_\alpha + \text{d} \rightarrow \text{p} + \text{n} + \nu_\alpha \quad (\alpha = e, \mu, \tau) \quad (1.16)$$

$$\text{ES : } \nu_\alpha + e^- \rightarrow \nu_\alpha + e^- \quad (\alpha = e, \mu, \tau) \quad (1.17)$$

*SNO experiment –  
solution to the solar  
neutrino problem*

The CC and the ES processes were observed through the detection of the Cherenkov light produced by the electrons in heavy water. The NC process was observed by detecting the  $\gamma$ -rays emitted as a result of neutron capture. SNO had three phases of operation which employed different techniques for detecting the NC process, using D, NaCl and  $^3\text{He}$  respectively for neutron absorption. The energy threshold for the detection of the CC and the ES processes was 5.5 MeV while that for the NC process was 2.2 MeV. The experiment was thus mostly sensitive to the high-energy solar  $^8\text{B}$  neutrinos.

The NC reaction helps to determine the total flux of all active neutrino flavours from the Sun whereas the CC reaction provides the  $\nu_e$  flux alone. The ES reaction offers an additional measurement of neutrino interaction and a cross-check of the other two reactions, however, with less statistical significance. The total active neutrino flux so obtained was in agreement with the total flux of the  $^8\text{B}$  neutrinos predicted by the SSM which rejected the possibility of transition of solar neutrinos into sterile states. However, a comparison of the CC and NC fluxes demonstrated a relative excess in the NC rate. Since only  $\nu_e$  is produced in the Sun, this observation could only be attributed to a  $\nu_\mu$  or  $\nu_\tau$  component in the solar neutrino flux originating from the flavour transitions of  $\nu_e$ . The measurements indicated that about 2/3 of the solar  $\nu_e$ s undergo flavour transformation to  $\nu_\mu$  or  $\nu_\tau$  on their way from the center of the Sun to the Earth [60]. The long-standing *solar neutrino problem* was thus solved by the SNO experiment which provided the first model-independent evidence in support of neutrino oscillation. The experiment also did not record any significant day-night asymmetry in the solar neutrino flux.

A 280 ton liquid scintillator detector, called Borexino, was constructed in 2007 in Gran Sasso, Italy with the aim of detecting  $^7\text{Be}$

solar neutrinos [61]. Similar to water Cherenkov detectors, the detection mechanism is based on the neutrino-electron ES. Liquid scintillator detectors are advantageous to water Cherenkov detectors in terms of reaching a lower energy threshold ( $\sim 250$  keV). The observed flux of  ${}^7\text{Be}$  neutrinos was in good agreement with the flux predicted considering the neutrino oscillation parameters obtained from the previous solar neutrino experiments.

*Borexino  
experiment*

The following best-fit oscillation parameters, with  $1\sigma$  uncertainties, are obtained combining all solar neutrino data [60].

$$\Delta m_{\text{sol}}^2 = 6.5_{-2.3}^{+4.4} \times 10^{-5} \text{eV}^2 \quad \tan^2 \theta_{\text{sol}} = 0.45_{-0.08}^{+0.09} \quad (1.18)$$

### 1.5.2 Atmospheric neutrino experiments

The Super-Kamiokande detector, discussed in Section 1.5.1, was also capable of detecting atmospheric neutrinos. At energies of several hundred MeVs, neutrino undergoes CC interaction with the nuclei in the detector to produce the corresponding charged lepton.

$$\nu_e + n \rightarrow p + e^- \quad \bar{\nu}_e + p \rightarrow n + e^+ \quad (1.19)$$

$$\nu_\mu + n \rightarrow p + \mu^- \quad \bar{\nu}_\mu + p \rightarrow n + \mu^+ \quad (1.20)$$

The Cherenkov radiation emitted by the charged lepton in water creates a ring-like image on the surface of the PMTs. The shape of the ring can be used to discriminate between electron and muon and hence identify the initial neutrino. Muons being much heavier than electrons follow a straight track in water and therefore create a sharp ring. On the other hand, electrons undergo scattering repeatedly and also produce electromagnetic shower which result in the formation of a diffused ring.

*Super-Kamiokande  
experiment*

The mechanism of atmospheric neutrino production illustrated in Eq. 1.10 and Eq. 1.11 imply that at low energies ( $E \leq 1$  GeV), for which most muons decay before reaching the Earth surface, the neutrino fluxes satisfy the following ratio.

$$r = \frac{\phi_{\nu_\mu} + \phi_{\bar{\nu}_\mu}}{\phi_{\nu_e} + \phi_{\bar{\nu}_e}} \simeq 2 \quad (1.21)$$

At higher energies, lesser muons decay before hitting the ground and hence the flavour ratio  $r$  goes up. Real experiments cannot measure  $r$  directly as the detector acceptance is different for electrons and muons. Thus, the experimental observation is reported in terms of the double-ratio  $R$  defined as,

*Atmospheric  
neutrino anomaly*

$$R = \frac{(N_\mu/N_e)_{\text{data}}}{(N_\mu/N_e)_{\text{MC}}} \quad (1.22)$$

where  $N_\mu$  and  $N_e$  are the respective numbers of muon and electron events. The numerator in Eq. 1.22 is the ratio observed experimentally and the denominator is the one obtained from Monte-Carlo predictions. The Super-Kamiokande experiment obtained  $R$  significantly lesser than unity [62] which indicates a deficit in the measured muon neutrino flux while the electron neutrino flux matched well with prediction. This observation became known as the *atmospheric neutrino anomaly*.

*Up-down  
asymmetry*

Another significant result from the Super-Kamiokande experiment is the zenith-angle dependence of the muon neutrino flux [62]. A substantial deficit of upward-going muons was observed at energies greater than 400 MeV. The distribution of the electron events was, however, in agreement with the expectation in the sub-GeV as well as the multi-GeV range. This observation is referred to as the *up-down asymmetry*.

*The  
solution*

Neutrino oscillation provides an obvious solution to both the afore-said discrepancies. Disappearance of atmospheric muon neutrinos due to flavour transformation caters for the observed deficit in the muon neutrino flux. The downward-going neutrinos produced in the atmosphere travel tens of kms to reach the detector whereas the distance covered by the upward-going neutrinos is several thousand kms. Consequently, the upward-going neutrinos have greater probability of flavour transition which explains the suppression of the upward-going flux compared to the downward-going one. The Super-Kamiokande experiment thus provided model-independent evidence in favour of neutrino oscillation.

*Oscillation  
channel*

The oscillation  $\nu_\mu \leftrightarrow \nu_e$  was disfavoured since no anomaly was observed in the  $\nu_e$  flux. The transition of  $\nu_\mu$  to sterile neutrino was also rejected due to the observed absence of matter effect and the up-down symmetry of NC events. The favoured oscillation channel was therefore the transformation of  $\nu_\mu$  to  $\nu_\tau$  [62].

The Super-Kamiokande data provided the following best-fit values of the oscillation parameters [62].

$$\Delta m_{\text{atm}}^2 = 2.1 \times 10^{-3} \text{eV}^2 \quad \sin^2 2\theta_{\text{atm}} = 1 \quad (1.23)$$

### 1.5.3 Reactor neutrino experiments

*KamLAND  
experiment*

The first convincing evidence in support of neutrino oscillations, using reactor neutrinos, was obtained in the Kamioka Liquid Scintillator Anti-Neutrino Detector (KamLAND) experiment [63] in 2002. It deployed a 1000 ton liquid scintillator detector located in the Kamioka mine, Japan. Electron antineutrinos from 55 nuclear reactors, situated at an average distance of 180 km, were detected using the inverse  $\beta$ -decay reaction (Eq. 1.1). The signature of  $\bar{\nu}_e$  capture was provided by a delayed coincidence between the prompt  $\gamma$ -pulses produced by the  $e^+e^-$  annihilation and the  $\gamma$ -pulses produced  $\sim 200 \mu\text{s}$  later by the capture of thermal neutron on hydrogen atom. Since the  $\bar{\nu}_e$ -spectra

from a reactor is well-known, a deformation of the observed neutrino spectrum, in addition to the deficit in the detected  $\bar{\nu}_e$ -flux, served as an indication of neutrino oscillation.

Results from the KamLAND experiment have reconfirmed the oscillation solution of the *solar neutrino problem*. A combined analysis of the KamLAND data and those obtained from the solar neutrino experiments results in improved accuracy of the oscillation parameter values [64].

$$\Delta m_{21}^2 = 7.9_{-0.5}^{+0.6} \times 10^{-5} \text{eV}^2 \quad \tan^2 \theta_{12} = 0.40_{-0.07}^{+0.10} \quad (1.24)$$

KamLAND is also the first experiment to detect geo-neutrinos originating from the decay chains of radioactive  $^{238}\text{U}$  and  $^{232}\text{Th}$  embedded in the Earth's crust.

Reactor neutrino experiments with source-detector distances  $\sim 1$  km are sensitive to the region of  $\Delta m^2$  corresponding to atmospheric neutrino oscillations. The first experiment of this kind was the CHOOZ experiment carried out in France in 1997 which looked for  $\nu_\mu \leftrightarrow \nu_e$  oscillation [65]. 5 ton of Gd-loaded liquid scintillator detector with a rock cover of 100 m was used to detect the  $\bar{\nu}_e$  beam from two nuclear reactors. The CHOOZ experiment did not observe any significant evidence for  $\bar{\nu}_e$  disappearance which rejected the  $\nu_\mu \leftrightarrow \nu_e$  solution of the *atmospheric neutrino anomaly* and provided an upper limit for  $\theta_{13}$  at 90% CL [66].

CHOOZ  
experiment

$$\sin^2 2\theta_{13} \lesssim 0.1 \quad (1.25)$$

Three reactor neutrino experiments, namely Double Chooz, Daya Bay and RENO, with detection principle same as that of KamLAND and CHOOZ, obtained better limits on  $\theta_{13}$  in 2012.

The Double Chooz experiment [67], with an improved radioactive shielding compared to the CHOOZ experiment, obtained the best-fit value of  $\theta_{13}$  as,

Double Chooz  
experiment

$$\sin^2 2\theta_{13} = 0.086 \pm 0.041 \pm 0.030 \quad (1.26)$$

The Daya Bay experiment [68] in China measured  $\bar{\nu}_e$  flux from 6 reactors using 6 functionally identical detectors, each of mass 20 ton, deployed in two near (470 m and 576 m) and one far (1648 m) underground locations. The following best-fit value of  $\theta_{13}$  was obtained.

Daya Bay  
experiment

$$\sin^2 2\theta_{13} = 0.092 \pm 0.016 \pm 0.005 \quad (1.27)$$

The RENO experiment [69] in Korea detected  $\bar{\nu}_e$ s from 6 reactors with a near (294 m) and a far (1383 m) detector, each of mass 16 ton, and obtained the following best-fit value of  $\theta_{13}$ .

RENO  
experiment

$$\sin^2 2\theta_{13} = 0.113 \pm 0.013 \pm 0.019 \quad (1.28)$$

## 1.5.4 Accelerator neutrino experiments

K2K  
experiment

The K2K experiment, which became operational in Japan in 1999, was the first experiment to confirm the phenomenon of neutrino oscillation using artificially produced neutrinos [70]. The mechanism for the production of accelerator neutrino beam is narrated in Section 1.4.  $\nu_\mu$  beam with a mean energy of 1.3 GeV, produced by the KEK-PS accelerator, was detected using a near and a far detector. The near detector system, located at a distance of 300 m from the pion production target, consisted of two detectors, a 1 kton water Cherenkov detector and a fine-grained detector system. Measurement of neutrino energy spectrum in the near detectors was used to predict the same in the far detector in case of no oscillation. The Super-Kamiokande detector, situated at a distance of 250 km, served as the far detector where the K2K events were selected by synchronization with proton extraction from the KEK-PS through the Global Positioning System (GPS).

Disappearance of  $\nu_\mu$  was identified by the suppression of the detected flux and the distortion of the neutrino energy spectrum in the far detector which yielded the following best-fit values of the oscillation parameters [71].

$$\Delta m_{32}^2 = 2.8 \times 10^{-3} \text{ eV}^2 \quad \sin^2 2\theta_{23} = 1 \quad (1.29)$$

Results from the K2K experiment reconfirm the oscillations observed in atmospheric neutrino experiments, excluding other explanations for the *atmospheric neutrino anomaly*, and also reject  $\nu_\mu \leftrightarrow \nu_e$  oscillation at 90% CL [72].

MINOS  
experiment

The Main Injector Neutrino Oscillation Search (MINOS) experiment, started in 2005, was the second long-baseline accelerator neutrino experiment with near and far detectors [73]. It detected  $\nu_\mu$  beam with energy range 1–5 GeV produced by the Neutrinos at the Main Injector (NuMI) facility at Fermilab, USA. The 1 kton near detector is located at a depth of 100 m at a distance of 1 km from the target. The far detector with a mass of 5.4 kton is situated at a distance of 735 km and 700 m underground. Both the detectors are iron-scintillator tracking calorimeters with a toroidal magnetic field of 1.3 T. The detection of  $\nu_\mu$  was via the CC interaction of neutrino with iron nuclei which results in the production of charged lepton and hadrons.

$$\nu_\mu + \text{Fe} \rightarrow \mu^- + X \quad (X = \text{hadrons}) \quad (1.30)$$

Results from the MINOS experiment provide convincing evidence in support of neutrino oscillations observed in atmospheric neutrino experiments and also measured the neutrino oscillation parameters with better accuracy [74].

$$\Delta m_{32}^2 = 2.32_{-0.08}^{+0.12} \times 10^{-3} \text{ eV}^2 \quad \sin^2 2\theta_{23} > 0.90 \quad (1.31)$$

The T2K experiment [75], which began operation in Japan in 2010, is the first off-axis long-baseline neutrino oscillation experiment. It detected a narrow-band  $\nu_\mu$  beam, produced by 30 GeV protons in the J-PARC Main Ring accelerator in Tokai, directed  $2.5^\circ$  off-axis. The advantage of using an off-axis configuration [76] is that it yields an almost monochromatic neutrino flux at the detector, irrespective of the pion energy. The near detector complex, located 280 m from the target, houses on-axis and off-axis detectors. The on-axis detector (INGRID), composed of an array of iron-scintillator sandwich modules, measures the  $\nu_\mu$  beam intensity, direction and profile. The off-axis detector, with a magnetic field of 0.2 T, consists of water-scintillator detector, tracker made up of Time Projection Chamber (TPC) and fine-grained detectors, and electromagnetic calorimeter. It measures the  $\nu_\mu$  flux and energy spectrum, intrinsic  $\nu_e$  contamination in the  $\nu_\mu$  beam in the direction of the far detector and reconstructs exclusive final states to study neutrino interactions in the far detector. The Super-Kamiokande detector, located at a distance of 295 km, operates as the far detector, with the T2K events identified by GPS-based synchronization with proton extraction at J-PARC.

T2K  
experiment

This experiment reported the first indication of  $\nu_\mu \rightarrow \nu_e$  appearance, at a significance of  $2.5\sigma$ , which provided the following limit on  $\theta_{13}$  at 90% CL, for  $\delta_{CP} = 0$  and normal (inverted) mass hierarchy [77].

$$0.03(0.04) < \sin^2 2\theta_{13} < 0.28(0.34) \quad (1.32)$$

### 1.5.5 Summary of results on oscillation parameters

Table 1 lists the best-fit values of the neutrino oscillation parameters obtained from global analyses of the existing neutrino oscillation data, excluding the results from Daya Bay and RENO experiments [78]. The values, determined using a 3- $\nu$  mixing framework, do not exhibit any significant deviation from the two-flavour analysis reported earlier because of small  $\theta_{13}$ . At present, no experimental information are available on the Dirac and the Majorana phases.

## 1.6 OPEN QUESTIONS

Spectacular results from various neutrino experiments, only a part of which is discussed in Sec. 1.5, have instigated many intriguing challenges that remain unresolved till date. This arises the need for conducting experiments that would surpass the current ones in volume, sensitivity and technological capabilities.

- High precision measurement of oscillation parameters – Observation of complete oscillation pattern demonstrating periodic changes in the neutrino flux with minima and maxima will lead

OSCILLATION PARAMETER	BEST-FIT VALUE ( $\pm 1\sigma$ )
$\Delta m_{\text{sol}}^2$	$7.58_{-0.26}^{+0.22} \times 10^{-5} \text{ eV}^2$
$ \Delta m_{\text{atm}}^2 $	$2.35_{-0.09}^{+0.12} \times 10^{-3} \text{ eV}^2$
$\sin^2\theta_{12}$	$0.306_{-0.015}^{+0.018}$
$\sin^2\theta_{23}$	$0.42_{-0.03}^{+0.08}$
$\sin^2\theta_{13}$	$0.021_{-0.008}^{+0.007}$

Table 1: Best-fit values of the 3- $\nu$  oscillation parameters derived from global analyses of the current neutrino oscillation data, excluding the results from Daya Bay and RENO experiments [78]. At present, no experimental information are available on the Dirac and the Majorana phases.

to improved estimation of the oscillation parameters, viz.,  $\Delta m_{21}^2$ ,  $\theta_{12}$ ,  $|\Delta m_{32}^2|$ ,  $\theta_{23}$ , etc.

- Precision measurement of the mixing angle  $\theta_{13}$  – More precise measurement of the smallest neutrino mixing angle  $\theta_{13}$  is of great importance in understanding the dynamics of neutrino oscillation. It determines the possibility of studying CP violation in the lepton sector and also revealing the neutrino mass spectrum.
- Neutrino mass hierarchy – Determining the sign of  $\Delta m_{32}^2$ , possibly through the study of neutrino matter effects, is absolutely necessary to identify the correct neutrino mass ordering.
- Absolute scale of neutrino mass – Significant constraints on the absolute scale of neutrino mass can be obtained through  $\beta$ -decay, neutrinoless double beta decay experiments and also from cosmology.
- Mechanism of neutrino mass generation – This necessitates understanding the physical origin of the patterns of  $\nu$ -mixing and  $\nu$ -masses, as obtained experimentally, and unraveling any underlying symmetry of particle interactions. The relationship between neutrino mixing and quark mixing also needs to be explored.
- Dirac or Majorana nature – If massive neutrinos are Dirac particles, they must be distinguishable from their antiparticles because of lepton number conservation. On the other hand, Majorana neutrino is its own antiparticle which can participate in lepton-number-violating processes. Only charge-neutral fermions can be Majorana and hence neutrinos stand out to be the only probable candidates within the Standard Model. This

can only be verified through the unambiguous observation of neutrinoless double beta decay.

- CP violation in the lepton sector – The possibility of leptonic CP violation, analogous to the quark sector, was invoked after the discovery of neutrino oscillation which may be probed in future long-baseline experiments.
- Existence of sterile neutrinos – Although current experimental results disfavour the existence of more than three neutrino species, further investigations are needed to rule out the theory of sterile or inert neutrinos (which cannot experience weak interactions) with better accuracy.
- Neutrino decay – Future experiments can improve current limits on sub-dominant mechanisms like neutrino decay and decoherence.
- Neutrino magnetic moment – Existence of neutrino mass implies non-zero magnetic moment which allows the possibility that neutrinos can also interact via electromagnetic force. Precise determination of its magnitude is, therefore, of utmost importance.
- Neutrino astronomy – Detection of ultrahigh-energy cosmic neutrinos can provide vital information about the astrophysical sources which serve as natural accelerators of the Universe. This will also shed light on the origin of ultrahigh-energy cosmic rays and help in understanding the observed *knee* and *ankle* features of the cosmic ray spectrum.
- Detection of relic neutrinos – Direct experimental detection of relic neutrinos, the messengers of the early Universe, seem to be far from reality because of their extremely low energy and interaction cross-section. This would require experiments with sensitivity orders of magnitude higher than that provided by the current technology.
- Neutrino in the evolution of the Universe – Progress in the theory of neutrino mixing might lead to a better understanding of the mechanism of generation of baryon number asymmetry in the early Universe.

## 1.7 PHYSICS POTENTIAL OF THE INO-ICAL DETECTOR

The history of Indian participation in experimental neutrino physics dates back to 1965 when atmospheric neutrino induced events were detected for the first time in the Kolar Gold Field underground detector in South India [79][80]. The legacy is carried forward in the shape

*The India-based  
Neutrino  
Observatory (INO)*

of the India-based Neutrino Observatory (INO), a multi-institutional effort to build an underground laboratory for neutrino experiments. The facility will be built inside a large underground cavern, with rock overburden of more than 1 km, to ensure minimal cosmic muon background. The major goal is to construct a massive magnetized neutrino detector, called the Iron Calorimeter (ICAL). There will also be smaller caverns to host other experiments like neutrinoless double beta decay, dark matter experiments, etc., which require low cosmic ray background environment. The observatory will be located at a distance of 110 km from the city of Madurai in South India.

*The Iron Calorimeter  
(ICAL) proposed by  
INO collaboration*

The INO collaboration has proposed to build a 50 kton magnetized ICAL detector to study atmospheric neutrinos and to make precision measurements of the neutrino oscillation parameters [6]. The detector will consist of three identical and adjacent modules, each of dimension 16 m x 16 m x 14.5 m. Each detector module will be made up of 151 horizontal layers of 56 mm thick low carbon iron plates interleaved with 40 mm gaps to house the Resistive Plate Chamber (RPC) units. The detector will mostly look for muon neutrino induced CC interactions using magnetized iron as the target mass and a total of 28,800 RPCs as sensitive detector elements. The detector will be magnetized to a field of 1.3 T to discriminate between the oppositely charged leptons produced as a result of neutrino and antineutrino interactions inside the detector volume. The total number of readout channels will be more than 3.6 million. Fig. 4 is a schematic of one module of the ICAL detector with top view of the magnet coils. Table 2 contains some important parameters of the ICAL detector structure. The ICAL detector is also being contemplated to be upgraded to a detector mass of 100 kton in future.

*Physics  
potential*

The ICAL detector is envisaged as a detector for atmospheric neutrinos as well as a future far detector for a neutrino factory beam. The major physics goals of the ICAL detector are listed below.

- Reconfirm atmospheric neutrino oscillation through explicit observation of the first oscillation swing in  $\nu_\mu$  disappearance as a function of L/E.
- Unambiguous and more precise estimation of neutrino oscillation parameters using atmospheric neutrinos.
- Study of matter effects for  $\nu_\mu$  and  $\bar{\nu}_\mu$  through electric charge identification of muons in CC interactions in order to determine the sign of  $\Delta m_{32}^2$ , which will resolve the neutrino mass hierarchy.
- Determine whether the mixing angle  $\theta_{23}$  is maximal and if not, explore how well its octant can be identified.
- Study of charge-conjugation and parity (CP) violation in the lepton sector as well as possible charge-conjugation, parity, time-reversal (CPT) violation.

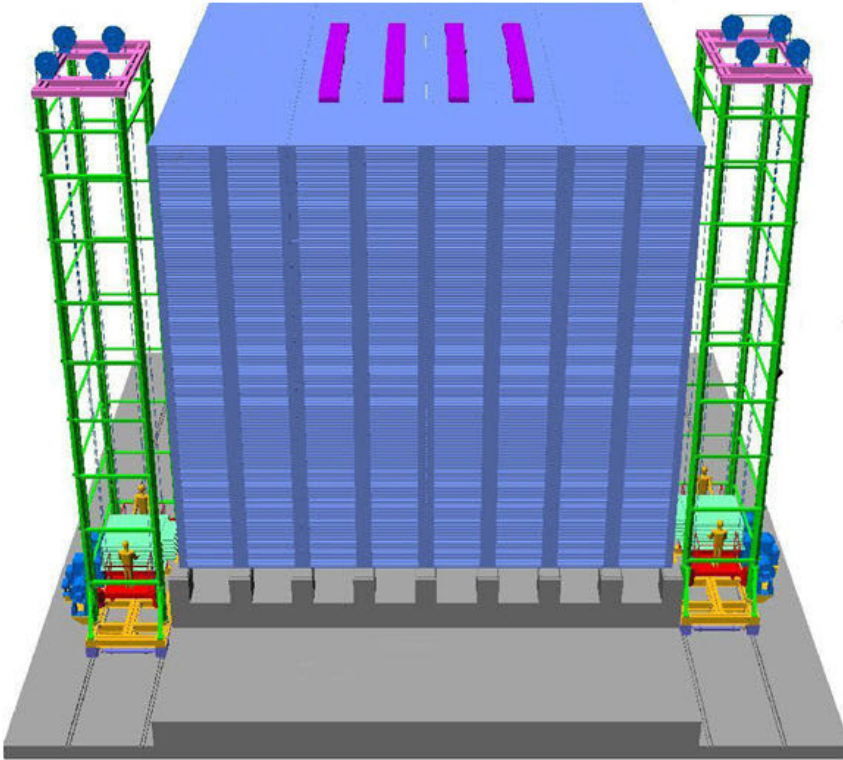


Figure 4: Schematic diagram of the ICAL detector module (16 m x 16 m x 14.5 m) with top view of the magnet coils.

Modules	3
Module dimension	16 m x 16 m x 14.5 m
Detector dimension	48 m x 16 m x 14.5 m
Iron layers	151
Iron plate thickness	56 mm
RPC layers	150
Gap for RPC units	40 mm
RPC dimension	1800 mm x 1910 mm x 20 mm
RPC units/ layer/ module	64
RPC units/ module	9600
Total RPC units	28,800
Total readout channels	$> 3.6 \times 10^6$
Magnetic field	1.3 T
Rock overburden	$> 1$ km

Table 2: Salient parameters of the ICAL detector structure.

- Exploring the possible existence of sterile neutrinos.
- Constraining long-range leptonic forces that distinguish between lepton flavours and hence have profound implications on neutrino oscillations.
- Study of multi-TeV cosmic ray muons using the pair-meter technique which can be helpful in comprehending the observed *knee* and *ankle* features of the cosmic ray spectrum..

### 1.8 TRIGGER SYSTEM FOR THE ICAL DETECTOR

The responsibility of the trigger system for an experiment lies with identifying the events of interest out of all the events to which the detector responds. The aim is to avoid loss of desired event during the dead time for acquiring an unwanted event as well as to ensure judicious consumption of data storage space. The physics requirements are translated in terms of the detector parameters to define the signature of an interesting event in the detector. The choice of the event signature, called the trigger criteria, should not be prone to accidental coincidence of random noise hits which will result in the storage of junk data. The trigger criteria for high energy physics experiments can vary from signal in certain number of channels within a specified time window to a particular mass of the end-products in a collision. Detection of an event bearing the characteristic signature results in the generation of a trigger signal which initiates the data acquisition system to record the information corresponding to the event. The delay in producing the trigger decision after the occurrence of the event plays a substantial role in determining the dead time for the data acquisition system. This limits the maximum event rate that can be handled by the experiment.

*Fundamentals of  
trigger system*

As mentioned in Section 1.7, the ICAL detector will use magnetized iron as the target volume for neutrino interactions and RPCs as sensitive detectors to track the resultant charged particles. Neutrino induced CC interactions in iron lead to the production of muon and hadrons at the interaction vertex in the final state, as shown in Fig. 5a. In case of NC neutrino events, as illustrated in Fig. 5b, only hadrons are produced at the interaction vertex and could result in muons due to hadronic decay.

*Neutrino  
interactions  
in ICAL*

A muon typically produces a long track inside the detector, traversing many layers, while hadrons give rise to shower of secondary particles, confined within a few layers. In case of CC neutrino events, the energy of the neutrino can be estimated from the momentum of the tracked muon and the hit distribution of the hadron shower. The neutrino direction can also be reconstructed from the direction of the muon. On the other hand, for NC neutrino events, the hit distribution

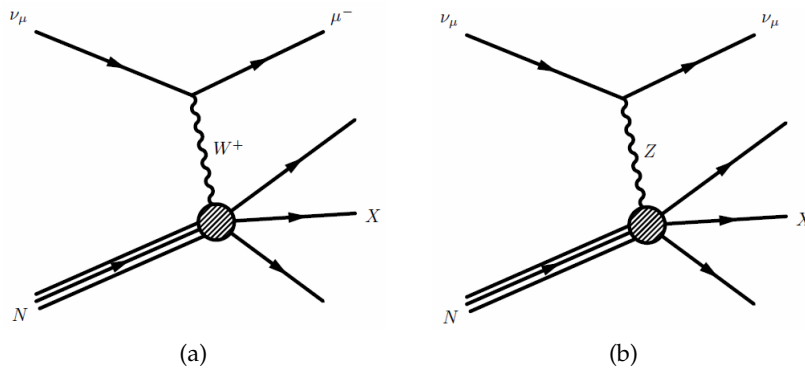


Figure 5: Neutrino-induced (a) charged current and (b) neutral current interactions producing muon and/ or hadrons ( $X$ ).

of the hadrons provides an estimation of the neutrino energy but there is no information about the direction of the neutrino.

The trigger criteria should be decided considering the characteristic hit pattern of such events so as to achieve an optimization of the detection efficiency of the desired events and the chance trigger rates. The trigger scheme should also ensure feasibility of hardware implementation taking into consideration the vast volume of the detector and the huge number of electronic channels to be dealt with.

This thesis is a documentation of the work on the development, validation and implementation of the ICAL trigger system, which meet the aforesaid benchmarks.

*Design goals of  
trigger system*



Part II

RESEARCH WORK



## DEVELOPMENT AND VALIDATION OF ICAL TRIGGER SCHEME

---

This chapter illustrates various aspects of the proposed architecture of the trigger scheme for one module of the ICAL detector. The associated chance coincidence rates are calculated at successive levels of trigger generation for different combinations of the trigger parameters which help to fix the criteria for an admissible chance trigger rate. A simulation framework has been developed in order to evaluate the trigger efficiency of the scheme for different events of interest for the ICAL detector. The simulation results are presented and their implications on the choice of the trigger parameters are also highlighted.

*Chapter  
summary*

### 2.1 SIGNAL FLOW IN THE DATA ACQUISITION SYSTEM

The structural details of the ICAL detector have been elucidated in Chapter 1, Section 1.7. The detector data acquisition system will record the event data on a global trigger. Typical signals produced by RPCs operated in avalanche mode, have an amplitude of about 2.5 mV across a 50  $\Omega$  load and a rise time of about 1 ns [8]. Hence, these signals need to undergo high speed, low noise pre-amplification before further processing in the RPC-DAQ board, which is the standalone data acquisition unit for each RPC [81]. The RPC-DAQ board records different information, like strip hit profile, timing, pulse profile etc., which together constitute the event data. A dedicated trigger system will generate a global trigger signal if the event topology satisfies the trigger criteria set by the user. The global trigger signal latches the event data in the RPC-DAQ board and invokes the data acquisition system to transfer the same to the back-end. The RPC-DAQ board also records the detector noise rate and the ambient parameters periodically in order to monitor the long-term stability of the detector. The digitized data is transferred from the RPC-DAQ board to the back-end servers through an in-built Ethernet-based network interface.

*RPC-DAQ board –  
the heart of ICAL  
data acquisition  
system*

### 2.2 THE TRIGGER CRITERIA

The trigger decision for the ICAL detector will be based on the event topology and is defined in terms of three trigger parameters, as listed below.

- (i) Multiplicity (M)
- (ii) Layer (N)
- (iii) Group (P)

*Trigger parameters  
which define the  
trigger criteria*

The trigger criterion is represented as  $M \times N / P$ , where  $M$  is the minimum strip multiplicity per RPC plane and  $N$  is the minimum number of layers out of a group of  $P$  consecutive layers having such  $M$ -fold multiplicity. The trigger menu will consist of a number of trigger criteria with different combinations of the trigger parameters corresponding to different types of physics events of interest. Hence, the goal of the trigger system is to ensure that if an event satisfies one or more of the user-specified trigger criteria in any part of the detector, a trigger signal should be generated to initiate the data acquisition system to record the event.

*Minimal detection  
threshold and  
negligible chance  
trigger rates*

The trigger criteria should be flexible enough so that the system is sensitive to the low-energy neutrino events, which produce hits only in few layers. However, the system also needs to refrain from generating spurious triggers as a consequence of chance coincidence of random noise hits. The choice of the trigger criteria which attains minimal detection threshold for the events of interest and simultaneously ensures negligible chance coincidence rates, is, therefore, the optimal one.

### 2.3 THE TRIGGER SCHEME

*The trigger  
pyramid*

The design of the trigger scheme follows a distributed and hierarchical architecture as illustrated in Fig. 6. The RPC forms the base level of trigger generation, where the Level 0 and the Level 1 trigger signals are produced. The next level in the hierarchy is segment, which is a logical unit consisting of a cluster of RPCs, and generates the Level 2 and the Level 3 trigger signals. A number of such logical segments together constitute the detector module, which is the final level for global trigger generation.

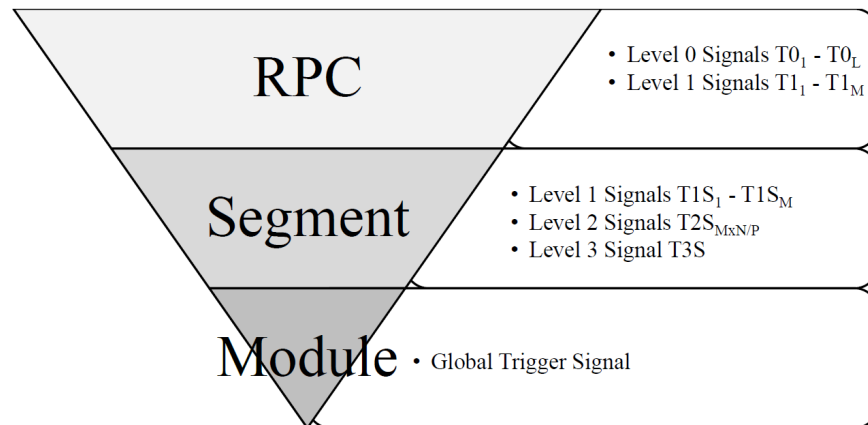


Figure 6: Hierarchy of the trigger scheme and the signals associated with each level of trigger generation.

The signal pick-up rate for all strips has been assumed to be identical and uniform for estimating the chance coincidence rates. The average

noise rate for an RPC strip of dimension 200 cm x 3 cm is observed to be 200 Hz on the Earth surface [8].

The choice of the coincidence window plays an important role in determining the performance of the trigger system. The minimum width of the coincidence window is decided by the delay incorporated in the processing and propagation of the signal in various stages of trigger generation. A too narrow coincidence window would thus lead to the loss of genuine events. Selection of a coincidence window too wide, on the other hand, results in increased chance coincidence rates. Considering both the factors, the coincidence window is taken as 100 ns, for all levels of trigger generation, in order to estimate the associated chance trigger rates.

*RPC strip noise rate  
200 Hz on surface  
and coincidence  
window 100 ns for  
chance trigger rate  
estimation*

### 2.3.1 RPC level

The RPC has two orthogonal planes, namely the X and the Y plane, each having 64 pick-up strips. The signals from the orthogonal readout planes are treated as two independent and identical systems.

The total number of RPC strips per module of the ICAL detector is more than 1.2 million. Therefore, using the RPC strip signals directly for generating the global trigger will result in enormous consumption of hardware resources and will also give rise to integration issues. Hence, the RPC strip signals are folded at successive levels to produce fewer number of signals which are exclusively used for the purpose of trigger generation. Since the hits produced in an RPC by a neutrino induced event are confined within a small volume of the same, there is no risk of losing genuine hits in such approach.

*Folding of RPC strip  
signals to produce  
fewer trigger signals*

#### 2.3.1.1 Level 0 trigger signal

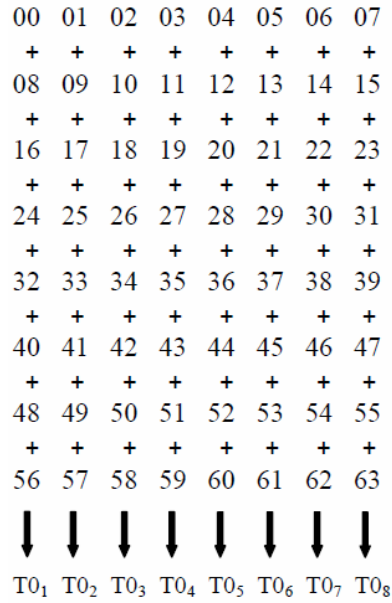
The signals from every L-th pick-up strip out of 64 strips on one plane of the 2 m x 2 m RPC are OR-ed to generate L Level 0 trigger ( $T_0$ ) signals. The average strip multiplicity of the RPCs is observed to be  $\sim 1.4$  for cosmic ray muons [12]. It is therefore legitimate to produce the  $T_0$  signals by combining every 8th ( $L = 8$ ) or 16th ( $L = 16$ ) strip per RPC plane. The combinations for the signals  $T_{01}$  to  $T_{0L}$  are shown in Fig. 7 for two different values of L (8, 16).

*8/16 Level 0 trigger  
signals per RPC  
plane*

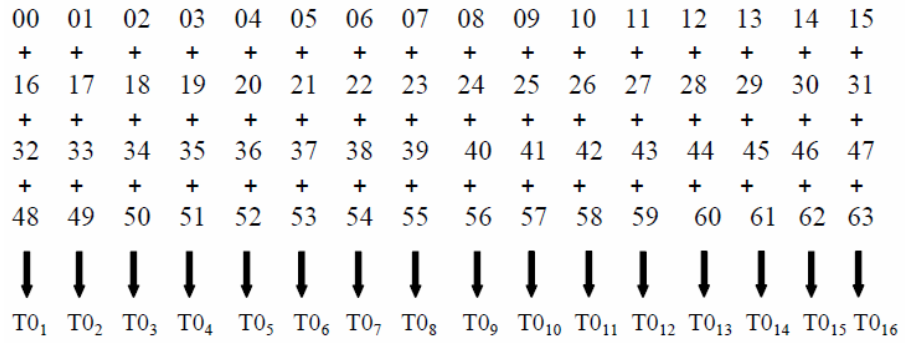
#### 2.3.1.2 Level 1 trigger signal

The Level 1 trigger ( $T_{1M}$ ) signals, which correspond to M – fold ( $M = 1, 2, 3, 4$ ) strip multiplicity per RPC plane, are formed by combining the Level 0 trigger signals. 1-fold strip multiplicity refers to a single strip being hit per RPC plane, 2-fold strip multiplicity implies any two consecutive strips per RPC plane being fired together, etc. The  $T_{1M}$  signals are obtained by M-fold coincidence of the consecutive  $T_0$  signals from each RPC plane, as shown below for  $L = 8$ .

*4 Level 1 or  
pre-trigger signals  
per RPC plane*



(a)



(b)

Figure 7: Formation of Level 0 trigger signals by combining signals from every (a) 8th and (b) 16th strip out of 64 pick-up strips per RPC plane.

- (i) 1-fold :  $T1_1 = T0_1 + T0_2 + \dots + T0_7 + T0_8$
- (ii) 2-fold :  $T1_2 = T0_1 \cdot T0_2 + T0_2 \cdot T0_3 + \dots + T0_7 \cdot T0_8 + T0_8 \cdot T0_1$
- (iii) 3-fold :  $T1_3 = T0_1 \cdot T0_2 \cdot T0_3 + T0_2 \cdot T0_3 \cdot T0_4 + \dots + T0_7 \cdot T0_8 \cdot T0_1 + T0_8 \cdot T0_1 \cdot T0_2$
- (iv) 4-fold :  $T1_4 = T0_1 \cdot T0_2 \cdot T0_3 \cdot T0_4 + T0_2 \cdot T0_3 \cdot T0_4 \cdot T0_5 + \dots + T0_7 \cdot T0_8 \cdot T0_1 \cdot T0_2 + T0_8 \cdot T0_1 \cdot T0_2 \cdot T0_3$

Considering a coincidence window of T seconds and a T0 rate of R Hz, M-fold chance rate  $r_M$  is given by [7],

$$r_M = C \cdot (MR^M T^{M-1}) \text{ Hz} \quad (2.1)$$

where C is the total number of combinations for each M-fold signal.

The  $T1_M$  rates for two different T0 rates (L = 8, 16) are shown in Table 3. It can be seen that the T0 and the  $T1_M$  (except 1-Fold) rates are slightly higher for L = 8 than that for L = 16 but the number of T0 signals is double in the later case. Adoption of a lower value of L (L = 4) will, on the other hand, restrict the hit pattern within 4 consecutive strips only which may not be acceptable in some cases. Thus, L = 8 is the optimal choice for the formation of the Level 0 trigger signals.

L	T0 RATE (Hz)	T1 <sub>1</sub> RATE (Hz)	T1 <sub>2</sub> RATE (Hz)	T1 <sub>3</sub> RATE (Hz)	T1 <sub>4</sub> RATE (Hz)
8	1600	$1.28 \times 10^4$	4.1	$9.8 \times 10^{-4}$	$2.1 \times 10^{-7}$
16	800	$1.28 \times 10^4$	2.05	$2.5 \times 10^{-4}$	$2.6 \times 10^{-8}$

Table 3: Level 0 and Level 1 chance trigger rates per RPC plane for L = 8, 16.

The four Level 1 trigger signals constitute the pre-trigger signals per RPC plane and are further processed in the trigger system.

According to the current design of the detector, there is a minimum gap of 20 cm between two adjacent RPCs and therefore it is unlikely that a particular event will have the hits distributed over neighboring RPCs within a layer. Hence, it is assumed that for any event, the track remains confined within a single RPC along a horizontal layer.

### 2.3.2 Segment level

The events of interest for the ICAL detector are expected to be localized within a small portion of the total volume of the detector module. Hence, the design of the trigger scheme follows a distributed approach, where a local boundary is defined for the purpose of trigger generation. The detector module is logically sub-divided into a number of identical segments, each of which is capable of generating

*Logical segmentation  
of the detector for  
trigger generation*

a local trigger, which will in turn initiate a global trigger. The segment dimensions are chosen considering the expected hit pattern of the events, the associated chance trigger rates and the feasibility of implementation.

*Segment  
dimensions*

The dimension of a segment in the horizontal direction is termed as horizontal spread ( $H_S$ ) and is defined as the number of RPCs per layer per segment.  $H_S$  can be further interpreted as the combination of two terms,  $H_{SX}$  and  $H_{SY}$ , which are the number of RPCs per layer per segment along the X and the Y direction respectively, as shown in Fig. 8.

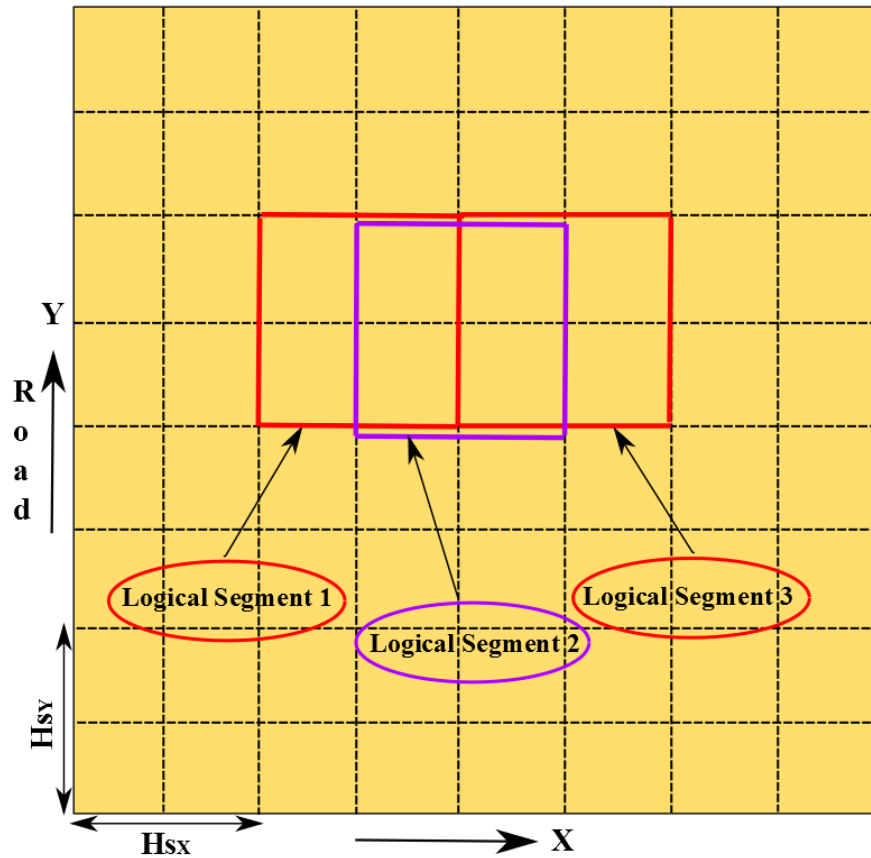


Figure 8: Horizontal segmentation pattern for  $H_{SX} = 2$ ,  $H_{SY} = 2$  with overlap between adjacent segments. Overlap along only the X direction is shown here and similar overlap exists in the Y direction as well.

The vertical dimension of a segment is defined as the number of layers per segment and is termed as vertical spread ( $V_S$ ). Every two adjacent segments must have overlap between them in the horizontal as well as the vertical direction. This is necessary to ensure that the trigger scheme is robust enough to cater for the events having hits shared between neighboring segments. Fig. 9 shows a three-dimensional view of the logical segmentation of the detector module with overlap between adjacent segments.

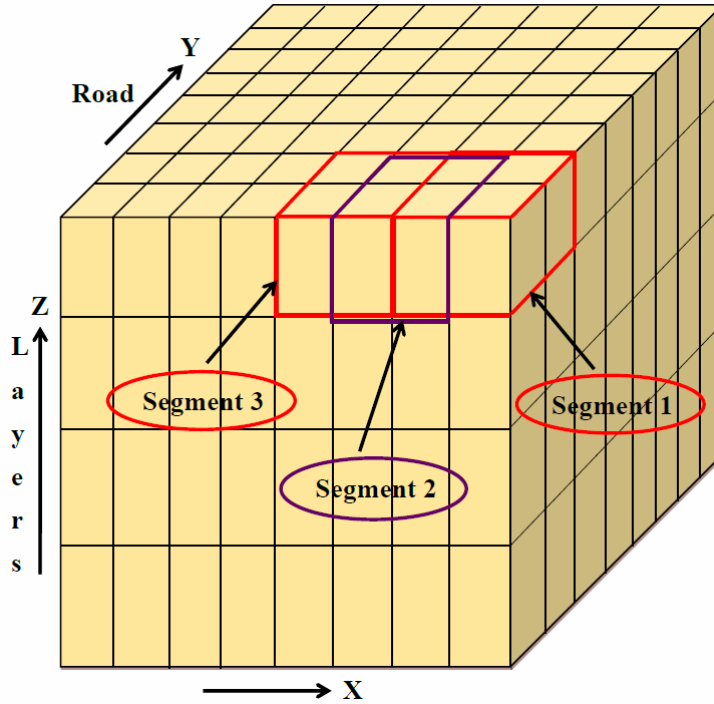


Figure 9: Logical segmentation of the detector module with overlap between adjacent segments. Overlap along only the X direction is shown here and similar overlaps exist in the Y and the Z directions as well.

The pre-trigger signals from the constituent RPCs of the segment are further folded to generate trigger signals at the segment level.

#### 2.3.2.1 Level 1 trigger signal

The Level 1 trigger ( $T1S_M$ ) signal for a horizontal layer of the segment is the OR of the  $T1_M$  signals from the constituent RPCs of that layer. Thus, there will be four  $T1S_M$  ( $M = 1, 2, 3, 4$ ) signals per plane corresponding to each layer of a segment.

*4 Level 1 trigger signals per segment layer per plane*

The  $T1S_M$  rates per segment layer for different values of  $H_S$  are listed in Table 4.

$H_S$	$T1S_1$ RATE (Hz)	$T1S_2$ RATE (Hz)	$T1S_3$ RATE (Hz)	$T1S_4$ RATE (Hz)
4 (2 × 2)	$5.12 \times 10^4$	16.4	$3.9 \times 10^{-3}$	$8.4 \times 10^{-7}$
9 (3 × 3)	$1.15 \times 10^5$	36.9	$8.8 \times 10^{-3}$	$1.9 \times 10^{-6}$
16 (4 × 4)	$2.05 \times 10^5$	65.5	$1.6 \times 10^{-2}$	$3.4 \times 10^{-6}$

Table 4: Level 1 chance trigger rates per layer of a segment for different values of  $H_S$ .

### 2.3.2.2 Level 2 trigger signal

*1 Level 2 trigger signal per trigger criterion per segment per plane*

The Level 2 trigger ( $T2S_{M \times N / P}$ ) signal for a segment should satisfy the trigger criterion  $M \times N / P$ . In order to take care of vertical overlap between successive segments, generation of the  $T2S_{M \times N / P}$  signal for a segment should consider the  $T1S_M$  signals from  $P - 1$  layers of the adjacent vertical segment. Thus, starting from the bottom, each segment, except the top ones, will have  $P - 1$  additional  $T1S_M$  signals from the segment lying immediately above. The total number of signals for the top segments depends on the value of  $V_S$  and might not be the same as that of the other segments. Hence the top segments will have partial or no overlap whereas all other segments will have full overlap in the vertical direction.

Considering  $T1S_M$  rate of  $R_M$  Hz and coincidence window of  $T$  seconds,  $M \times N / P$  chance rate  $r_{M \times N / P}$  is given by [7],

$$r_{M \times N / P} = C \cdot (NR_M^N T^{N-1}) \text{ Hz} \quad (2.2)$$

where  $C$  is the total number of combinations which is obtained as the product of the number of groups of  $P$  consecutive layers in a segment and the number of combinations of any  $N$  layers out of a group of  $P$  layers.

Thus, a segment will have one  $T2S_{M \times N / P}$  signal per plane corresponding to a particular trigger criterion.

### 2.3.2.3 Level 3 trigger signal

*2 Level 3 or local trigger signals per segment, one for each plane*

The Level 3 trigger ( $T3S$ ) signal for a segment is the OR of the  $T2S_{M \times N / P}$  signals of that segment for a set of trigger criteria involving different combinations of  $M$  and  $N$ . Over the range of trigger criteria, as  $M$  goes higher,  $N$  goes lower and ideally the value of  $P$  should also come down. Since the vertical overlap between successive segments depends on the value of  $P$ , varying  $P$  for different trigger criteria will pose practical problem regarding the routing of signals. Hence, it is decided to have the same value of  $P$  for all trigger criteria. This does not affect the chance coincidence rates as the rates corresponding to the criteria with  $M > 1$  are negligibly small and the overall chance trigger rate is dominated by the rate for the criterion with  $M = 1$ .

Hence each segment will have two Level 3 or local trigger signals,  $T3S_X$  and  $T3S_Y$ , for the  $X$  and the  $Y$  plane respectively.

*2 sets of trigger criteria*

Fig. 10 shows two different sets of trigger criteria. Each set consists of multiple trigger criteria with different combinations of  $M$  and  $N$ , represented as  $M \times N / P$ . It has been shown later that the 1-Fold and the 2-Fold trigger criteria mainly correspond to muon track while the criteria with  $M > 2$  represent hadron shower.

Table 5 and Table 6 contain the  $T2S_{M \times N / P}$  and the  $T3S$  rates calculated for different segment dimensions and for the two sets of trigger criteria respectively.

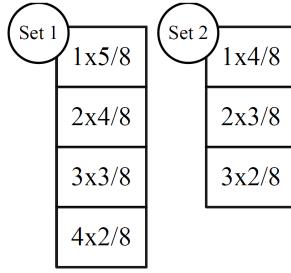


Figure 10: Two different sets of trigger criteria. Each set consists of multiple trigger criteria with different combinations of M and N, represented as  $M \times N / P$ .

The choice of logical segments takes into account the case of diagonal tracks too as the  $T1S_M$  signal for a particular layer of a segment is the OR of the  $T1_M$  signals from the constituent RPCs of that layer. Fig. 11 shows four RPCs in a segment, with RPCs A and B in one layer and C and D in another layer. The track goes diagonally through the segment, producing hits in RPC B in the top layer and RPC C in the bottom layer.

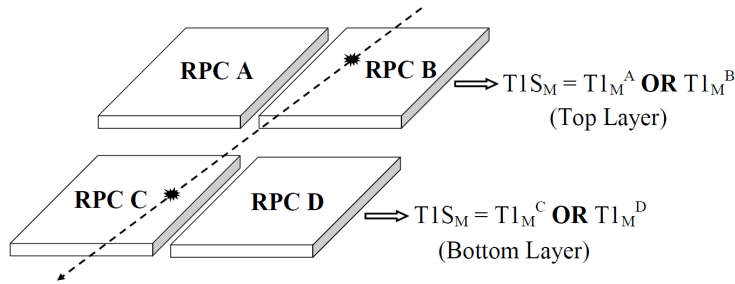


Figure 11: Diagonal track through a segment hitting RPC B in the top layer and RPC C in the bottom layer. The trigger scheme caters for such events as the  $T1S_M$  signal for a particular layer of a segment is the OR of the  $T1_M$  signals from all the constituent RPCs of that layer.

### 2.3.3 Module level

The local trigger signals generated at the segment level are eventually combined to produce the global trigger signal at the module level.

#### 2.3.3.1 Global trigger signal

The global trigger ( $GT_X$  and  $GT_Y$ ) signal for the X and the Y plane is the OR of the  $T3S_X$  and the  $T3S_Y$  signals respectively, from all the constituent segments of the module. The global trigger (GT) signal for the detector module is obtained as the OR of the  $GT_X$  and the  $GT_Y$  signals. A GT signal to the data acquisition system initiates the registering of the event data. The complete flow of generation of the global trigger signal from the RPC strip signals, is illustrated in Fig. 12.

*1 global trigger signal per detector module*

$H_S$	$V_S$	SEGMENT DIMENSION	$T2S_{1 \times 5/8}$ RATE (Hz)	$T2S_{2 \times 4/8}$ RATE (Hz)	$T2S_{3 \times 3/8}$ RATE (Hz)	$T2S_{4 \times 2/8}$ RATE (Hz)	T3S RATE (Hz)
4 (2 x 2)	10	4 m x 4 m x 1 m	0.06	$1 \times 10^{-13}$	$3.8 \times 10^{-19}$	$9.9 \times 10^{-18}$	0.06
	20	4 m x 4 m x 2 m	0.12	$2 \times 10^{-13}$	$7.7 \times 10^{-19}$	$2 \times 10^{-17}$	0.12
	40	4 m x 4 m x 4 m	0.25	$4 \times 10^{-13}$	$1.5 \times 10^{-18}$	$3.9 \times 10^{-17}$	0.25
9 (3 x 3)	30	6 m x 6 m x 3 m	10.7	$7.8 \times 10^{-12}$	$1.3 \times 10^{-17}$	$1.5 \times 10^{-16}$	10.7
	40	6 m x 6 m x 4 m	14.2	$1 \times 10^{-11}$	$1.8 \times 10^{-17}$	$2 \times 10^{-16}$	14.2
	60	6 m x 6 m x 6 m	21.3	$1.6 \times 10^{-11}$	$2.6 \times 10^{-17}$	$3 \times 10^{-16}$	21.3
16 (4 x 4)	40	8 m x 8 m x 4 m	252.2	$1 \times 10^{-10}$	$9.8 \times 10^{-17}$	$6.3 \times 10^{-16}$	252.2
	60	8 m x 8 m x 6 m	378.3	$1.6 \times 10^{-10}$	$1.5 \times 10^{-16}$	$9.5 \times 10^{-16}$	378.3
	80	8 m x 8 m x 8 m	504.4	$2.1 \times 10^{-10}$	$2 \times 10^{-16}$	$1.3 \times 10^{-15}$	504.4

Table 5: Level 2 and Level 3 chance trigger rates for different segment dimensions for trigger criteria set 1.

$H_S$	$V_S$	SEGMENT DIMENSION	$T2S_{1 \times 4/8}$ RATE (Hz)	$T2S_{2 \times 3/8}$ RATE (Hz)	$T2S_{3 \times 2/8}$ RATE (Hz)	$T3S$ RATE (Hz)
	10	4 m x 4 m x 1 m	9.6	$2.8 \times 10^{-8}$	$2.2 \times 10^{-10}$	9.6
4 (2 x 2)	20	4 m x 4 m x 2 m	19.2	$5.5 \times 10^{-8}$	$4.3 \times 10^{-10}$	19.2
	40	4 m x 4 m x 4 m	38.5	$1.1 \times 10^{-7}$	$8.7 \times 10^{-10}$	38.5
	30	6 m x 6 m x 3 m	$7.4 \times 10^2$	$9.5 \times 10^{-7}$	$3.3 \times 10^{-9}$	$7.4 \times 10^2$
9 (3 x 3)	40	6 m x 6 m x 4 m	$9.9 \times 10^2$	$1.3 \times 10^{-6}$	$4.4 \times 10^{-9}$	$9.9 \times 10^2$
	60	6 m x 6 m x 6 m	$1.5 \times 10^3$	$1.9 \times 10^{-6}$	$6.6 \times 10^{-9}$	$1.5 \times 10^3$
	40	8 m x 8 m x 4 m	$9.9 \times 10^3$	$7.1 \times 10^{-6}$	$1.4 \times 10^{-8}$	$9.9 \times 10^3$
16 (4 x 4)	60	8 m x 8 m x 6 m	$1.5 \times 10^4$	$1.1 \times 10^{-5}$	$2.1 \times 10^{-8}$	$1.5 \times 10^4$
	80	8 m x 8 m x 8 m	$2 \times 10^4$	$1.4 \times 10^{-5}$	$2.8 \times 10^{-8}$	$2 \times 10^4$

Table 6: Level 2 and Level 3 chance trigger rates for different segment dimensions for trigger criteria set 2.

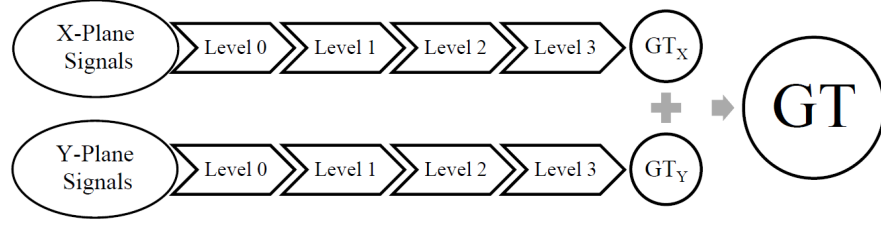


Figure 12: Complete flow of generation of the global trigger signal from the RPC strip signals through different levels of trigger generation.

#### 2.4 SURFACE AND UNDERGROUND CHANCE TRIGGER RATES

*RPC strip noise  
rate 10 Hz in  
underground*

The RPC noise rate in the underground, as reported by the OPERA experiment, at a depth of 1.4 km and using RPCs of area  $3.2 \text{ m}^2$ , is  $17 \text{ Hz/m}^2$  [9]. The rock overburden for the INO site is similar to that of OPERA and RPCs of area  $4 \text{ m}^2$  will be used [6]. Thus, a similar figure can be assumed for the underground noise rate of the RPCs in the ICAL detector. However, the exact scenario of the radioactive background and the correlated electronic noise, which are the two main sources of RPC pick-up, are not yet known for the ICAL detector. Hence, in order to tread a safer approach, the underground noise rate for the ICAL RPCs is assumed to be 10 times that of the OPERA RPCs, i.e.,  $170 \text{ Hz/m}^2$ . This amounts to a pick-up rate of about 10 Hz for an RPC strip of dimension  $200 \text{ cm} \times 3 \text{ cm}$ .

*Optimal trigger  
criteria and segment  
dimensions for  
admissible chance  
coincidence rates*

The chance trigger rates on the Earth surface and underground have been estimated for different segment dimensions and for both sets of trigger criteria (Fig. 10), as shown in Table 7. The GT rates are found to be the same for segments with different values of  $V_S$  but having a fixed value of  $H_S$ . Use of segments with smaller  $V_S$ , for a particular  $H_S$ , are likely to enhance the system complexity by increasing the number of segments without offering any advantage, either in terms of chance coincidence rates or detection efficiency, as shown subsequently in Section 2.5. On the other hand, use of segments with large  $V_S$  may not be feasible from the implementation perspective. A segment dimension of  $4 \text{ m} \times 4 \text{ m} \times 4 \text{ m}$  is found to be optimum considering the chance trigger rates as well as the feasibility of implementation. A comparison of the chance coincidence rates for the trigger criteria of set 1 and set 2 implies that loosening the trigger criteria by a single layer leads to substantial increase in the chance trigger rates. This is because  $N$  comes in the exponent while calculating the  $M \times N / P$  chance rate (Eq. 2.2) and hence a small change in  $N$  causes significant variation in the chance trigger rate. The expected overall event rate for the ICAL detector is around 10 Hz. Hence, the chance coincidence rates corresponding to the trigger criteria of set 1 seem to be acceptable but those for the trigger criteria of set 2 are higher than the tolerable limit.

$H_S$	$V_S$	SEGMENT DIMENSION	SEGMENTS	RATES FOR TRIGGER CRITERIA SET 1		RATES FOR TRIGGER CRITERIA SET 2	
				SURFACE (Hz)	UNDERGROUND (Hz)	SURFACE (Hz)	UNDERGROUND (Hz)
4 (2 x 2)	10	4 m x 4 m x 1 m	735	87	$2.7 \times 10^{-5}$	$1.4 \times 10^4$	$8.5 \times 10^{-2}$
	20	4 m x 4 m x 2 m	392	87	$2.7 \times 10^{-5}$	$1.4 \times 10^4$	$8.5 \times 10^{-2}$
	40	4 m x 4 m x 4 m	196	87	$2.7 \times 10^{-5}$	$1.4 \times 10^4$	$8.5 \times 10^{-2}$
9 (3 x 3)	30	6 m x 6 m x 3 m	180	$3.7 \times 10^3$	$1.1 \times 10^{-3}$	$2.6 \times 10^5$	1.6
	40	6 m x 6 m x 4 m	144	$3.7 \times 10^3$	$1.1 \times 10^{-3}$	$2.6 \times 10^5$	1.6
	60	6 m x 6 m x 6 m	108	$3.7 \times 10^3$	$1.1 \times 10^{-3}$	$2.6 \times 10^5$	1.6
16 (4 x 4)	40	8 m x 8 m x 4 m	100	$4.5 \times 10^4$	$1.4 \times 10^{-2}$	$1.8 \times 10^6$	11.1
	60	8 m x 8 m x 6 m	75	$4.5 \times 10^4$	$1.4 \times 10^{-2}$	$1.8 \times 10^6$	11.1
	80	8 m x 8 m x 8 m	50	$4.5 \times 10^4$	$1.4 \times 10^{-2}$	$1.8 \times 10^6$	11.1

Table 7: Chance trigger rates on the surface and underground for different sets of trigger criteria and different segment dimensions. The GT rates are found to be the same for segments with different values of  $V_S$  but having a fixed value of  $H_S$ . A comparison of the chance trigger rates for the trigger criteria of set 1 and set 2 indicates that loosening the trigger criteria by a single layer leads to a substantial increase in the chance trigger rates.

*Chance trigger rates  
in noisy situation*

The assumption of identical and uniform strip noise rate, however, does not hold in practice. Occasionally, the noise rate for few RPC strips in the prototype detector have been observed to go up to 1 MHz. This is most likely due to external electromagnetic interference (EMI) or additional instrumental noise, e.g., high current or local discharge in some detector units. The chance coincidence rates for such a noisy situation are estimated by considering about 100 RPC strips, out of a total of 9600 strips, with noise rate of 1 MHz, distributed over the detector module. In comparison with the figures shown in Table 7, the surface and the underground chance trigger rates are found to increase by a factor of about 3 and 30 respectively, which are still within the acceptable range.

## 2.5 TRIGGER SIMULATION FRAMEWORK

The design of the proposed trigger scheme should be substantiated by determining the trigger efficiency of the scheme for different events of interest for the ICAL detector. This necessitates development of a simulation framework to evaluate the performance of the trigger scheme as a function of different trigger parameters and over the range of all desired events.

### 2.5.1 Analysis input

*Hit position  
information from  
detector simulation  
of muon and  
neutrino events*

The simulation package based on GEANT4 [10] and ROOT, developed in order to study the physics potential of the ICAL detector, has been used to generate the input for the present analysis. Muon events as well as different types of neutrino events have been studied. The INO-ICAL simulation code has its own Monte-Carlo event generator using which muon events are generated while Nuance [11] is used for generating various kinds of neutrino events, over a wide energy range and different incident directions. The event vertices are randomly distributed over the volume of the detector module. These events are simulated using the INO-ICAL simulation code and the output of the digitization stage, which provides hit position information in the detector in the same format as that which will be available from the detector data acquisition system, is used as the input for the current analysis. The hit information content is shown in Fig. 13, which provides the actual geographical position of particle hit in the detector.

*C++ – based  
framework with  
event display*

The simulation framework has been developed in C++ using Qt libraries [82] for designing the front-end Graphical User Interface (GUI) and ROOT libraries for analysis. It also provides two-dimensional and three-dimensional event display, as demonstrated in Fig. 14, which is especially useful for debugging purpose.

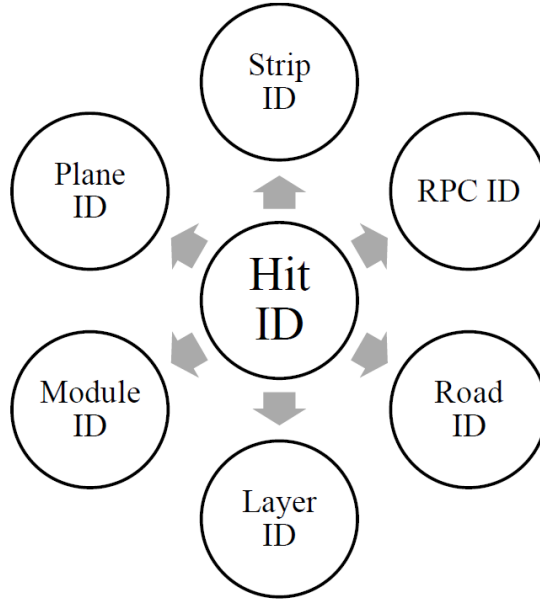


Figure 13: Hit position information obtained from the digitization output of the INO-ICAL simulation code, in the same format as that which will be available from the detector data acquisition system.

### 2.5.2 Results

Fig. 15 illustrates the algorithm to determine whether an event has satisfied the trigger criteria, which has been developed in compliance with the hierarchy of the proposed trigger scheme.

The trigger efficiency  $\eta$  is defined as,

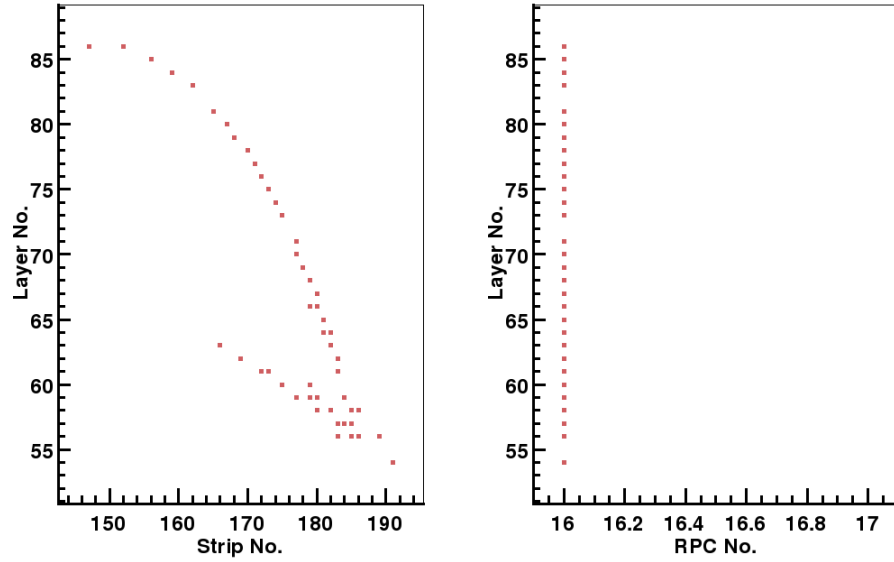
$$\eta = \frac{N_E}{N_T} \quad (2.3)$$

where  $N_E$  is the number of events satisfying the trigger criteria and  $N_T$  is the total number of events. The single hit efficiency of the RPCs is assumed to be 95%, as observed in the prototype detector [12]. The trigger efficiency is determined for the trigger criteria of set 1 (Fig. 10) and the segment size of 4 m  $\times$  4 m  $\times$  4 m, for muon events as well as neutrino events, as a function of energy and direction of the incident particle. The nature of variation of trigger efficiency with different trigger parameters, like  $M$ ,  $N$ ,  $P$ ,  $H_{SX}$ ,  $H_{SY}$  and  $V_S$ , has also been studied.

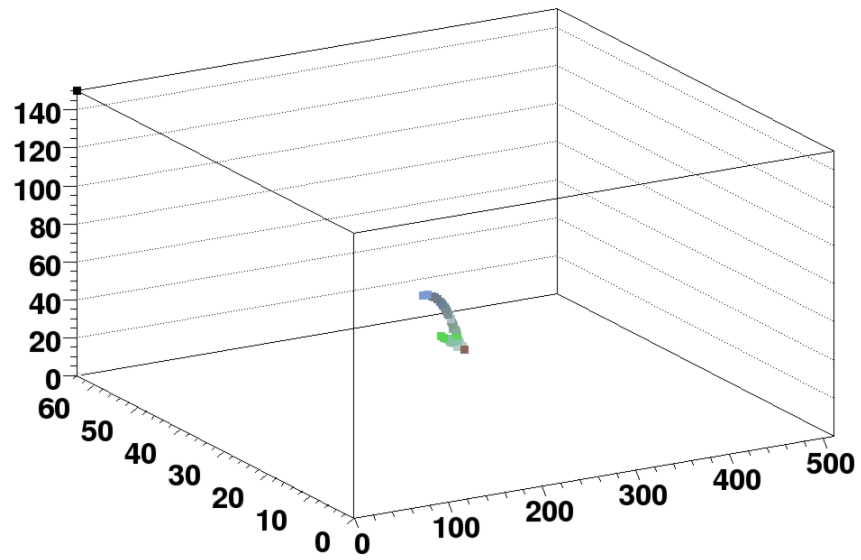
#### 2.5.2.1 Muon events

Muon events in the energy range of 1 to 10 GeV with the incident direction varying from  $0^\circ$  to  $90^\circ$  have been analyzed. Fig. 16 shows the variation of trigger efficiency with muon energy for incident directions  $0^\circ$ ,  $20^\circ$ ,  $40^\circ$ ,  $60^\circ$  and  $80^\circ$ . The efficiency increases with the increase in energy. This is because a particle with higher energy traverses a longer

*Trigger efficiency as a function of energy for different incident directions*



(a)



(b)

Figure 14: (a) Two-dimensional and (b) three-dimensional display of a neutrino induced event.

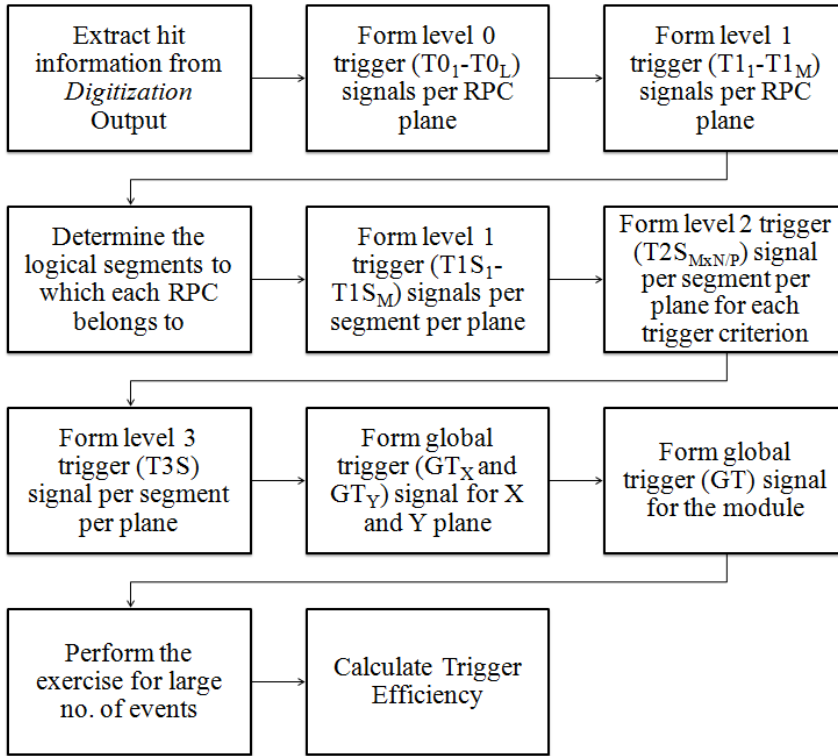


Figure 15: Analysis algorithm to determine whether an event has satisfied the trigger criteria.

path through the detector and therefore has a greater probability of satisfying the trigger criteria. The efficiency is, however, not 100% even at higher energy which is attributed to the fact that some events are always generated in the gap regions, producing less number of hits, insufficient to meet the trigger criteria. The efficiency deteriorates even at higher energy for angles of incidence greater than  $60^\circ$ . Since the particles incident at a large angle traverse lesser number of layers, their chance of satisfying the trigger criteria is lower. Hence at a particular energy, the efficiency is generally higher for smaller incident angles but becomes lower for larger incident angles.

The variation of trigger efficiency as a function of different combinations of the trigger parameters  $M$  and  $N$  is shown in Fig. 17. The plot represents the individual contribution of each trigger criterion in generating a trigger. It is evident that in case of muon events, the efficiency is dominated by the 1-Fold and the 2-Fold criteria.

The trigger efficiency remains almost unchanged with variations in other trigger parameters like  $P$ ,  $H_{SX}$ ,  $H_{SY}$  and  $V_S$ , as shown in Fig. 18. However, change in the detector efficiency is likely to have an impact on the trigger efficiency as a function of the parameter  $P$ . The variation of trigger efficiency with  $P$  for different values of detector efficiency is observed to be minimal ( $\sim 1\%$ ), as illustrated in Fig. 19.

*Dependence of trigger efficiency on trigger parameters and segment dimensions*

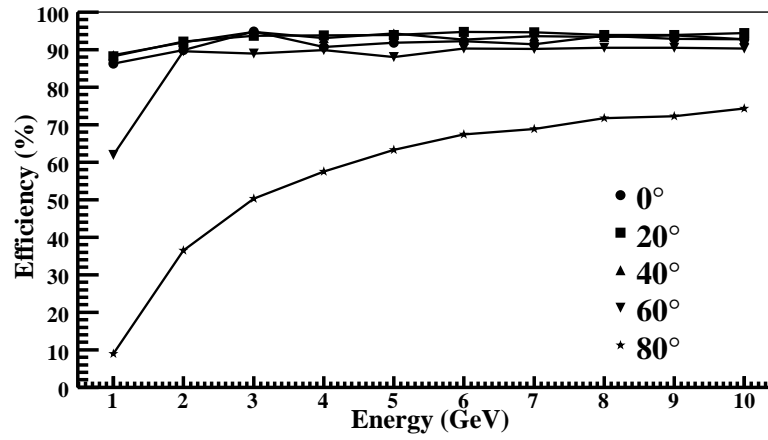


Figure 16: Trigger efficiency vs. energy for muon events of energy 1 to 10 GeV and incident direction 0°, 20°, 40°, 60°, 80°. The efficiency increases with energy and comes down for larger incident angles.

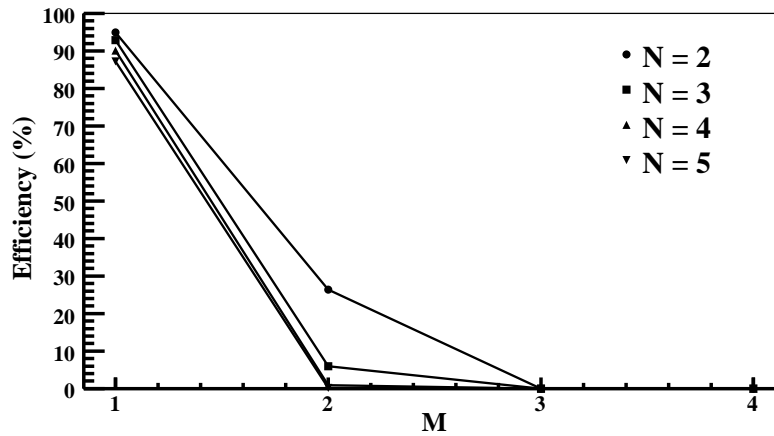


Figure 17: Trigger efficiency vs. trigger parameters (M, N) for muon events of energy 1 GeV and incident direction 10°. Rest of the trigger parameters are fixed as  $P = 8$ ,  $H_{SX} = 2$ ,  $H_{SY} = 2$ ,  $V_S = 40$ . The trigger efficiency for muon events is dominated by the 1-Fold and the 2-Fold criteria.

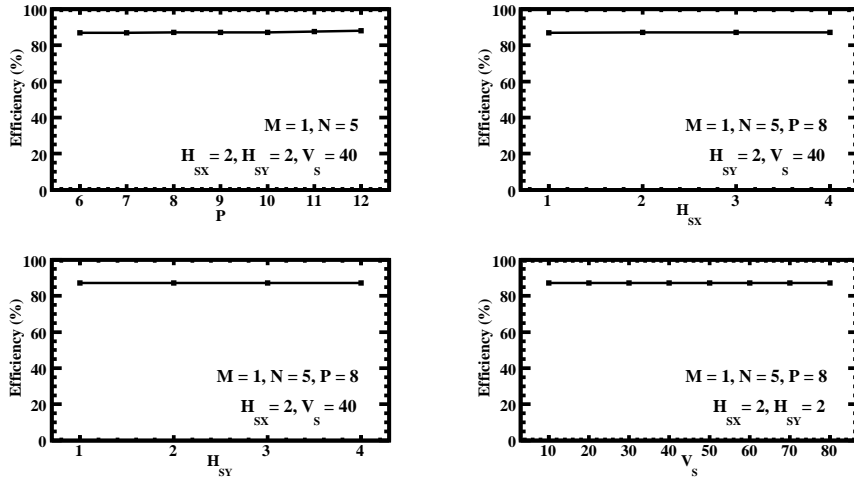


Figure 18: Trigger efficiency vs. trigger parameters ( $P, H_{SX}, H_{SY}, V_S$ ) for muon events of energy 1 GeV and incident direction  $10^\circ$ . The trigger efficiency is independent of these parameters.

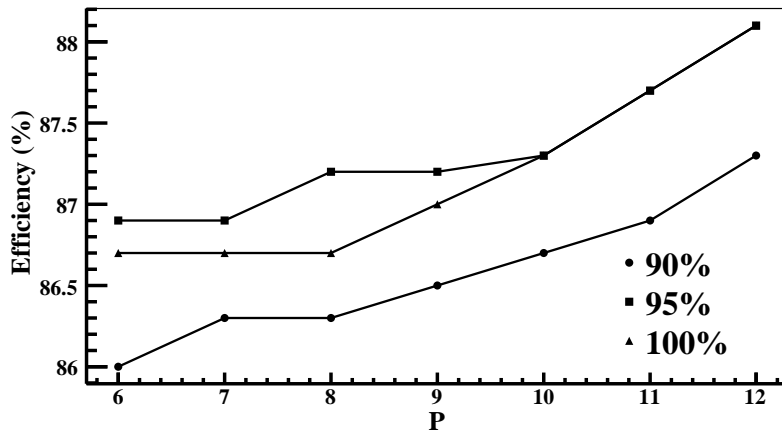


Figure 19: Trigger efficiency vs. trigger parameter  $P$  for muon events of energy 1 GeV and incident direction  $10^\circ$  and for different values of detector efficiency. Rest of the trigger parameters are fixed as  $M = 1, N = 5, H_{SX} = 2, H_{SY} = 2, V_S = 40$ . The variation is observed to be minimal ( $\sim 1\%$ ).

Section 2.5.2.2 deals with the estimation of trigger efficiency for different kinds of neutrino events. Nature of variation of trigger efficiency as a function of the trigger parameters like  $P$ ,  $H_{SX}$ ,  $H_{SY}$  and  $V_S$  for neutrino events are found to be similar to that observed in case of muon events. Hence those plots have not been included in the discussion that follows.

### 2.5.2.2 Charged current neutrino events

Charged current neutrino events in the energy range of 1 to 10 GeV with the incident direction varying from  $0^\circ$  to  $90^\circ$  have been studied. Fig. 20 shows trigger efficiency varying as a function of neutrino energy for incident directions  $0^\circ$ ,  $20^\circ$ ,  $40^\circ$ ,  $60^\circ$  and  $80^\circ$ . The efficiency clearly goes up with energy and comes down for larger incident angles. The variation of trigger efficiency for different combinations of the trigger parameters  $M$  and  $N$  is shown in Fig. 21. The contribution of trigger criteria with  $M > 2$  seems to be significant for charged current neutrino events in comparison with muon events (Fig. 17). This is due to the hadron shower produced as a result of the interaction which satisfies the 3-Fold and the 4-Fold trigger criteria.

*3-Fold, 4-Fold  
trigger criteria more  
significant for  
neutrino events than  
muon events*

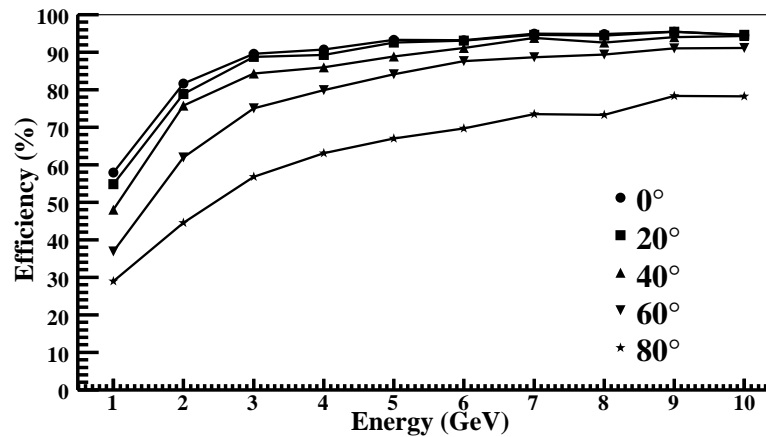


Figure 20: Trigger efficiency vs. energy for charged current neutrino events of energy 1 to 10 GeV and incident direction  $0^\circ$ ,  $20^\circ$ ,  $40^\circ$ ,  $60^\circ$ ,  $80^\circ$ . The efficiency goes up with energy and comes down for larger incident angles.

Charged current neutrino events are further classified as quasi-elastic, resonant and deep-inelastic events and the trigger efficiency has been determined for each of these types.

The variation of trigger efficiency with neutrino energy for different incident directions in case of quasi-elastic neutrino events is shown in Fig. 22. The efficiency is higher for higher energy and lower for larger angles of incidence. Fig. 23 shows trigger efficiency varying as a function of the trigger parameters  $M$  and  $N$ . Most of the neutrino energy is carried away by the muon in quasi-elastic neutrino events.

*Trigger efficiency for  
quasi-elastic  
neutrino events  
dominated by 1-Fold,  
2-Fold trigger  
criteria*

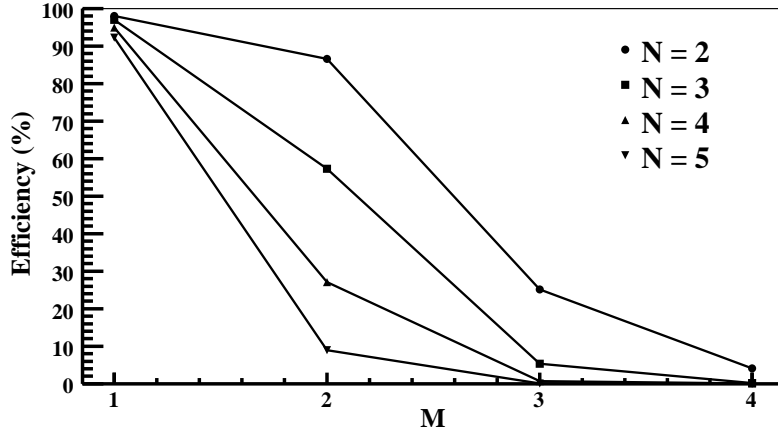


Figure 21: Trigger efficiency vs. trigger parameters (M, N) for charged current neutrino events of energy 5 GeV and incident direction  $10^\circ$ . Rest of the trigger parameters are fixed as  $P = 8$ ,  $H_{SX} = 2$ ,  $H_{SY} = 2$ ,  $V_S = 40$ . Trigger criteria with  $M > 2$  are more significant for charged current neutrino events compared to muon events (Fig. 17).

The trigger efficiency is, therefore, dominated by the 1-Fold and the 2-Fold trigger criteria and the contribution of criteria with  $M > 2$  is insignificant.

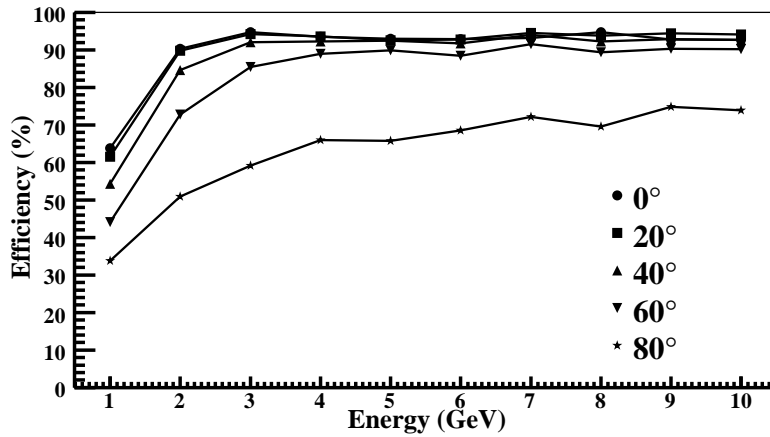


Figure 22: Trigger efficiency vs. energy for quasi-elastic neutrino events of energy 1 to 10 GeV and incident direction  $0^\circ$ ,  $20^\circ$ ,  $40^\circ$ ,  $60^\circ$ ,  $80^\circ$ . The efficiency is higher for higher energy and lower for larger angles of incidence.

Trigger efficiency varying as a function of neutrino energy and angle of incidence for resonant neutrino events is depicted in Fig. 24. The efficiency goes up with energy and comes down for larger incident angles. Fig. 25 shows the variation of trigger efficiency for different combinations of the trigger parameters M and N. Contribution of trigger criteria with  $M > 2$  appears to be slightly higher for the

*Trigger criteria with  $M > 2$  more dominant for resonant neutrino events*

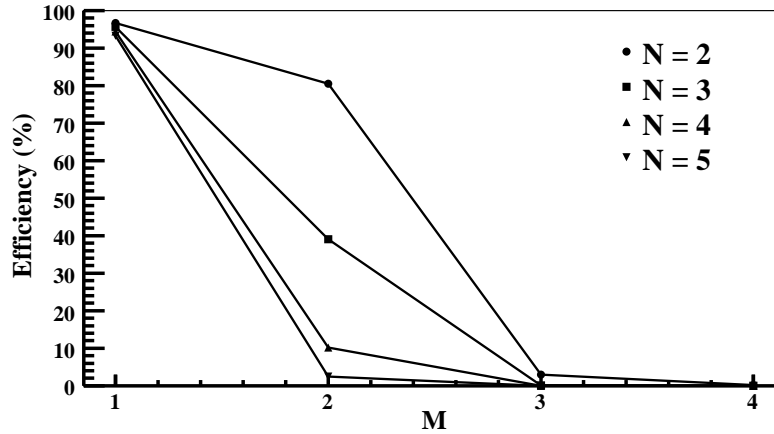


Figure 23: Trigger efficiency vs. trigger parameters (M, N) for quasi-elastic neutrino events of energy 5 GeV and incident direction 10°. Rest of the trigger parameters are fixed as  $P = 8$ ,  $H_{SX} = 2$ ,  $H_{SY} = 2$ ,  $V_S = 40$ . Trigger efficiency for quasi-elastic neutrino events is dominated by the 1-Fold and the 2-Fold trigger criteria.

resonant neutrino events than that for the quasi-elastic events (Fig. 23). This is because of the hadron produced in the resonant interaction which sometimes satisfies the 3-Fold and the 4-Fold criteria.

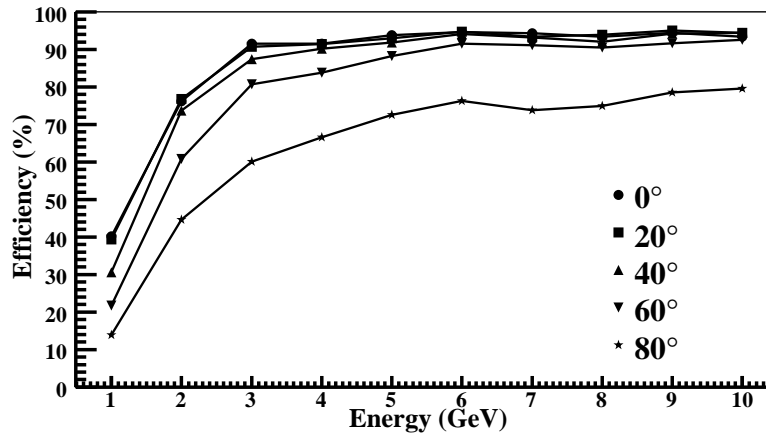


Figure 24: Trigger efficiency vs. energy for resonant neutrino events of energy 1 to 10 GeV and incident direction 0°, 20°, 40°, 60°, 80°. The efficiency goes up with energy and comes down for larger incident angles.

Fig. 26 illustrates the variation of trigger efficiency with neutrino energy for different incident directions in case of deep-inelastic neutrino events. The efficiency is higher for higher energy and lower for larger angles of incidence. The variation of trigger efficiency as a function of the trigger parameters M and N is shown in Fig. 27. Due to the production of hadron shower in deep-inelastic neutrino events, the contribution of trigger criteria with  $M > 2$  appears to be much higher

*3-Fold, 4-Fold trigger criteria most significant for deep-inelastic neutrino events*

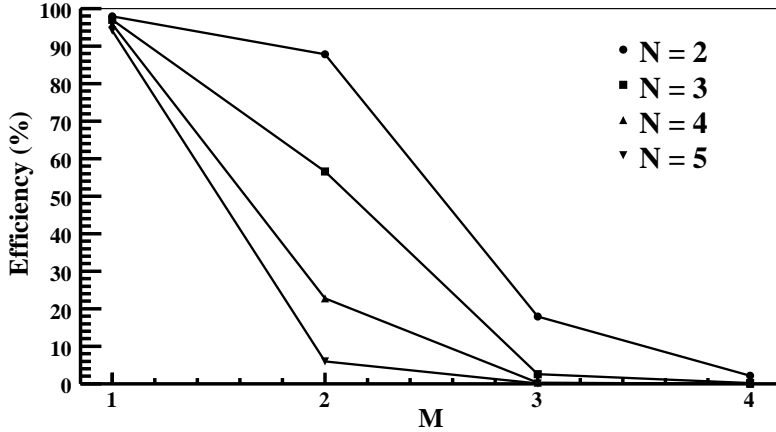


Figure 25: Trigger efficiency vs. trigger parameters ( $M$ ,  $N$ ) for resonant neutrino events of energy 5 GeV and incident direction  $10^\circ$ . Rest of the trigger parameters are fixed as  $P = 8$ ,  $H_{SX} = 2$ ,  $H_{SY} = 2$ ,  $V_S = 40$ . Contribution of trigger criteria with  $M > 2$  appears to be slightly higher for the resonant neutrino events than that for the quasi-elastic neutrino events (Fig. 23).

in comparison with that for the quasi-elastic (Fig. 23) and the resonant (Fig. 25) events.

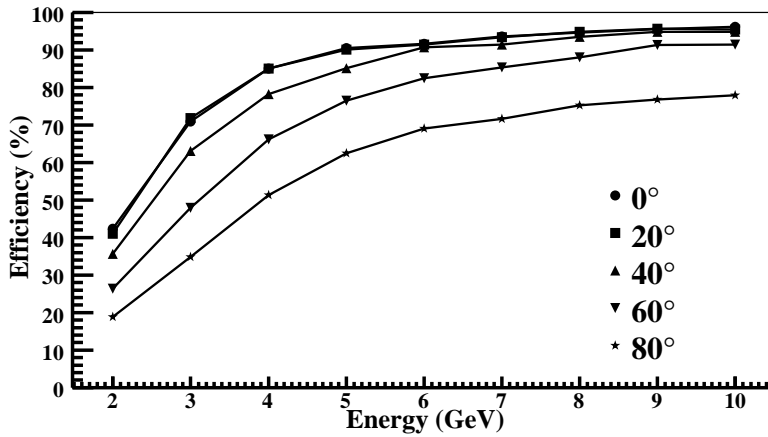


Figure 26: Trigger efficiency vs. energy for deep-inelastic neutrino events of energy 2 to 10 GeV and incident direction  $0^\circ$ ,  $20^\circ$ ,  $40^\circ$ ,  $60^\circ$ ,  $80^\circ$ . The efficiency is higher for higher energy and lower for larger angles of incidence.

The deterioration of trigger efficiency, as observed in the preceding results, is mostly attributed to two types of events, the events incident at large angles which do not traverse requisite number of layers and the events generated in the gap region which produce less number of hits, insufficient to meet the trigger criteria. However, such events with very few hits are of less interest as they cannot be reconstructed eventually even if they are recorded by the data acquisition system.

*Trigger efficiency  
w.r.t. reconstructed  
events*

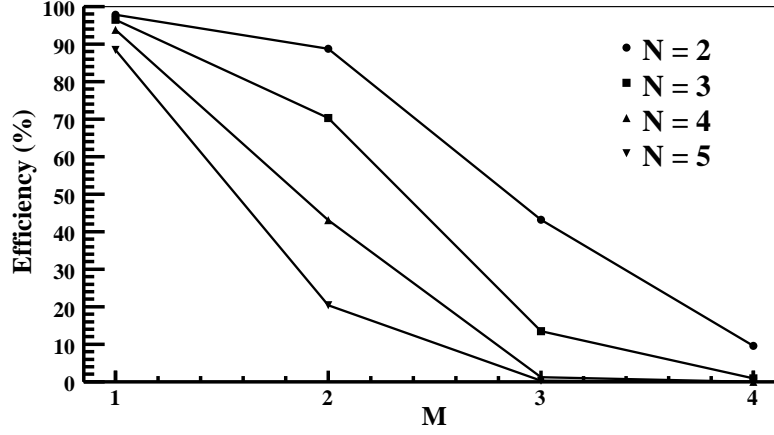


Figure 27: Trigger efficiency vs. trigger parameters ( $M$ ,  $N$ ) for deep-inelastic neutrino events of energy 5 GeV and incident direction  $10^\circ$ . Rest of the trigger parameters are fixed as  $P = 8$ ,  $H_{SX} = 2$ ,  $H_{SY} = 2$ ,  $V_S = 40$ . Contribution of trigger criteria with  $M > 2$  is much higher for deep-inelastic neutrino events in comparison with that for quasi-elastic (Fig. 23) and resonant (Fig. 25) neutrino events.

Thus, the trigger efficiency is expected to improve significantly if it is calculated with respect to the reconstructed events only instead of the whole set of events.

Reconstruction information for the events in the digitization output can be obtained from the corresponding reconstruction output of the INO-ICAL simulation code. Trigger efficiency  $\eta_r$  with respect to the reconstructed events is defined as,

$$\eta_r = \frac{N_E}{N_{RE}} \quad (2.4)$$

where  $N_E$  is the number of reconstructed events satisfying the trigger criteria and  $N_{RE}$  is the total number of reconstructed events.

Fig. 28 illustrates the trigger efficiency for reconstructed charged current neutrino events over the energy range of 1 to 10 GeV and different incident directions. The trigger efficiency is found to be greater than 95% for the reconstructed events over the entire range of energy and incident direction.

The above results are obtained without taking any detector noise into account. The detection efficiency of the proposed scheme in presence of detector noise also needs to be evaluated, similar to the estimation of chance coincidence rates for noisy circumstances in Section 2.4. The trigger efficiency is, therefore, also determined considering about 100 noise hits randomly distributed over the volume of the detector module, which comprises a total of 9600 RPC strips. A marginal improvement in the trigger efficiency is observed on addition of noise and is attributed to those few events where the trigger criteria is not

*Trigger efficiency in  
presence of detector  
noise*

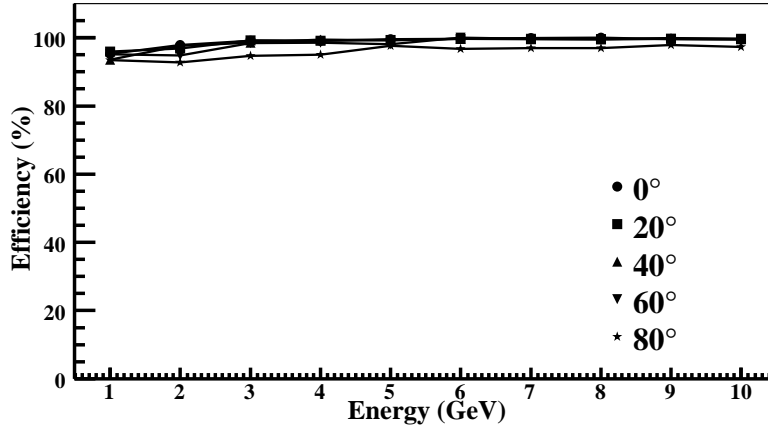


Figure 28: Trigger efficiency vs. energy for reconstructed charged current neutrino events. The trigger efficiency is greater than 95% for the reconstructed events over the entire range of energy and incident direction.

satisfied by the event hit pattern alone but by the combination of the event hits and the noise hits.

Hence, the results from the simulation framework provide us with a good assessment of the detection efficiency of the trigger scheme for different events of interest for the ICAL detector. It is evident that substantially high trigger efficiency can be obtained for the desired events under the proposed scheme. The nature of variation of trigger efficiency as a function of different trigger parameters are understood. The simulation results also help to correlate the trigger parameters with the characteristic features of different types of interactions. Such findings will be useful in the choice of these parameters to attain the desired efficiency for an event of interest.

The proposed trigger scheme is thus validated which motivates to proceed toward the implementation of the same.



## TRIGGER MODULE FOR ICAL PROTOTYPE DETECTOR

---

The hardware implementation of the proposed trigger scheme for the ICAL detector is initiated by designing a trigger module for the prototype of the ICAL detector. The trigger module has been designed with an FPGA-based technique and is deployed in the prototype detector in order to evaluate its performance. This chapter is centered around the description of the characteristic features of the design of the trigger module as well as its performance validation in the prototype detector.

*Chapter  
summary*

### 3.1 THE PROTOTYPE DETECTOR

A magnet-less prototype of the ICAL detector has been constructed to develop and study the individual detector components, including RPCs, gas system, front-end electronics and data acquisition system. The prototype detector consists of 12 layers of RPCs of 1 m x 1 m lateral area, and is continuously tracking cosmic ray muons [12]. Each RPC is made of 2 float glass plates of thickness 3 mm, with an intermediate gas gap of 2 mm, across which a differential voltage of  $\pm 4.9$  kV is applied. The RPCs are operated in avalanche mode using a gas mixture of Freon (R134a), Isobutane and SF<sub>6</sub> in the proportion of 95.5:4.2:0.3 by volume. Orthogonal pick-up panels are mounted on either side of the gas gap, each having 32 pick-up strips with a strip pitch of 30 mm, which provide the particle hit coordinates in a horizontal plane. The activities related to the fabrication and the characterization of glass RPCs, undertaken during the development of the prototype stack, are described in Ref. [83].

*12 layers of  
1m x 1m RPCs*

Fig. 29 shows the prototype detector with the front-end readout electronics on either side. The front-end electronics has been custom designed while the back-end of the data acquisition system is based on VME. A detailed description of the data acquisition system of the prototype detector can be found in Ref. [13].

*Custom front-end  
electronics and  
VME-based back-end  
system*

The trigger module generates a trigger signal on the passage of a charged particle through the detector provided the track hit pattern satisfies the trigger criteria set by the user. On receiving the trigger, the data acquisition system records the event data which comprises the RPC strip hit profile and the timing information. The data collected are used to characterize the detector performance by estimating RPC efficiency, strip multiplicity, timing resolution, etc. In addition, the detector noise rate and the ambient parameters are periodically recorded by the data acquisition system in order to monitor the long



Figure 29: The prototype detector with the front-end readout electronics on either side.

term stability of the detector. These results are also used to optimize a number of parameters related to the RPC design, gas mixture and readout electronics.

### 3.2 THE TRIGGER SYSTEM

The trigger decision for the prototype detector is based on the event topology and is represented as  $M \times N / P$ , in the same format as that to be used for the ICAL detector (Ref. Chapter 2, Section 2.2).

*Trigger signals associated with different levels of trigger generation*

The trigger system for the prototype detector has a hierarchical structure conforming to the proposed architecture of the ICAL trigger scheme (Ref. Chapter 2, Section 2.3). The trigger signals corresponding to different levels of trigger generation are listed below.

- (i) Level 0 (T0) signals
- (ii) Level 1 (T1) signals
- (iii) Level 2 (T2) signals
- (iv) Final trigger (FT) signal

The RPC has two orthogonal readout planes, namely the X and the Y plane, each having 32 pick-up strips, which are treated as two independent and identical systems. The RPC strip signals are folded

at consecutive stages to produce fewer signals, to be employed for trigger generation, identical to the approach pursued in case of the ICAL trigger scheme (Ref. Chapter 2, Section 2.3.1).

3.2.1 *Level 0 trigger signal*

The signals from every 8th pick-up strip out of 32 strips on one plane of the RPC are OR-ed to generate 8 level 0 trigger (T0) signals. The combinations for signals T0<sub>1</sub> to T0<sub>8</sub> are shown in Fig. 30.

8 Level 0 trigger signals per RPC plane

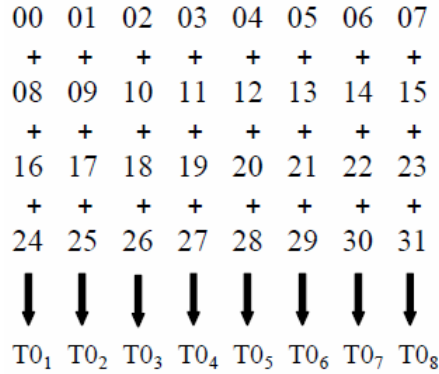


Figure 30: Formation of 8 Level 0 trigger signals by combining signals from every 8th strip out of 32 pick-up strips per RPC plane.

3.2.2 *Level 1 trigger signal*

The Level 1 trigger (T1<sub>M</sub>) signals, which correspond to M-fold strip multiplicity per RPC plane, are formed by M-fold coincidence of the consecutive T0 signals from each RPC plane. A total of 4 T1<sub>M</sub> signals, for M = 1, 2, 3, 4, are generated which constitute the pre-trigger signals per RPC plane. The combinations for the 4 T1<sub>M</sub> signals can be found in Chapter 2, Section 2.3.1.2.

4 Level 1 or pre-trigger signals per RPC plane

3.2.3 *Level 2 trigger signal*

The Level 2 trigger (T2<sub>MxN/P</sub>) signal is generated if the T1<sub>M</sub> signals satisfy the trigger criterion MxN/P. One T2<sub>MxN/P</sub> signal will be produced for each RPC plane corresponding to a particular trigger criterion.

1 Level 2 trigger signal per trigger criterion per RPC plane

3.2.4 *Final trigger signal*

The Level 2 trigger signals are ultimately combined together to generate the final trigger signal for the data acquisition system. The final trigger (FTX and FTY) signal for the X and the Y plane is the OR of

1 final trigger signal  
for the detector

the Level 2 trigger ( $T2_{M \times N/P}$ ) signals for different trigger criteria, belonging to the respective planes. The final trigger (FT) signal for the detector is obtained by OR-ing the FTX and the FTY signals. The FT signal invokes the data acquisition system to register the event data. The complete flow of generation of the final trigger signal, starting from the RPC strip signals, is illustrated in Fig. 31.

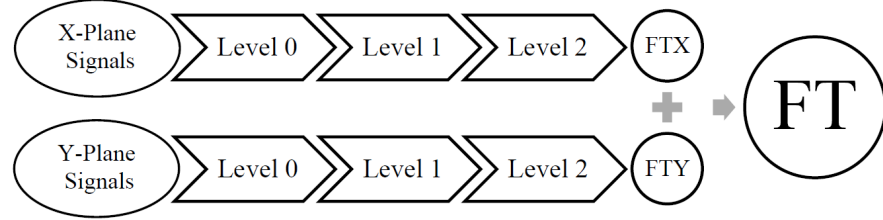


Figure 31: Complete flow of generation of the final trigger signal from the RPC strip signals through different levels of trigger generation.

The T0 and the T1 signals are generated in different stages of the front-end electronics, as described in Ref. [13]. The trigger module, to be elucidated in Section 3.3, receives the T1 signals from all 12 RPCs as input and produces the FT signal, employing an FPGA-based technique.

### 3.3 THE FINAL TRIGGER MODULE

Implemented using  
CAEN V1495  
module with Altera  
Cyclone FPGA

The architecture of the Final Trigger Module (FTM) has been designed in VHDL with an Altera Cyclone FPGA (EP1C20F400C6) [14] as the target device, using Quartus II 9.0 as the design software. The CAEN V1495 General Purpose Module [15] is programmed with the design logic and is used as the FTM. The width of the coincidence window for the formation of the  $T2_{M \times N/P}$  signal is 200 ns.

Although four  $T1_M$  signals ( $M = 1, 2, 3, 4$ ) are formed corresponding to each RPC plane, due to the port constraints of the V1495 board, two  $T1_M$  signals ( $M = 1, 2$ ) per RPC plane have been used as the inputs to the FTM. The trigger logic consists of the following trigger criteria.

- (i)  $1 \times 5/8$
- (ii)  $2 \times 4/8$

Look-up table based  
technique

The logic for detecting the coincidence of the  $T1_M$  signals has been implemented following the classical look-up table based approach. The  $T1_M$  signals are used as inputs to the look-up table which generates the  $T2_{M \times N/P}$  signal at the output. The advantage of using such technique is that the inner hardware remains same irrespective of the input pattern which ensures that the processing time does not vary with the change in input. On the other hand, the device needs to be re-configured every time the user wants to implement a new trigger criteria.

The look-up table based trigger logic has been implemented utilizing the block RAMs inside the FPGA. The design schematic is shown in Fig. 32. The Cyclone FPGA has block RAMs of size 4 K which implies that the maximum width of the RAM address can be 12 bits. This matches very well with our system requirement where there are a total of 12  $T1_M$  signals per readout plane for a particular trigger criterion, with 1  $T1_M$  signal per RPC plane. Since there are altogether four sets of  $T1_M$  signals for two sets of trigger criteria, four block RAMs are used to generate the respective  $T2_{M \times N/P}$  signals.

*Look-up tables  
designed using  
FPGA block RAMs*

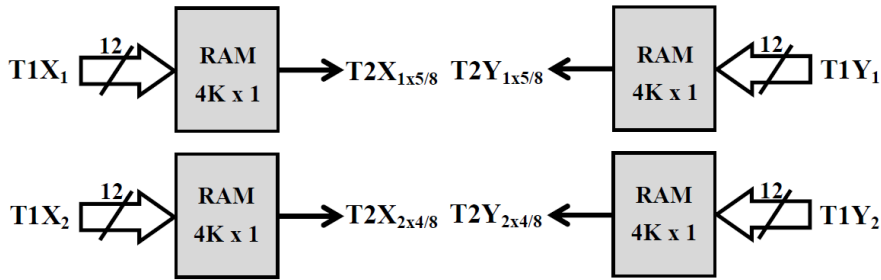


Figure 32: Schematic of the look-up table based trigger logic implemented using the block RAMs inside the FPGA.

The design of the FTM is schematically shown in Fig. 33. There are user programmable mask registers using which the  $T1_M$  signal from any layer or any intermediate coincidence signal can be enabled or disabled by the user. This is necessary to block the pre-trigger signal from any noisy RPC, the coincidence signal corresponding to a particular trigger criterion or the final trigger signal from any of the readout planes. The masked  $T1_M$  signals are fed to the RAM-based look-up tables to generate the respective coincidence output, i.e., the  $T2_{M \times N/P}$  signal, which is then masked. The output signal of the FTM was initially observed to have glitches which might result in spurious triggers. This is taken care of by using a deglitching circuit for the coincidence signals, as shown in Fig. 34, where a delay of about 20 ns is generated using the gate delays of the FPGA. The masked and deglitched coincidence signals are fed to internal scalers in order to count the coincidence rates. As shown in Fig. 33, the final trigger (FTX and FTY) signal for the X and the Y plane is the OR of the masked and deglitched coincidence signals of the respective planes. The final trigger (FT) signal is obtained as the OR of the FTX and the FTY signals. Each of the FTX, FTY and FT signals can also be masked by the user. The FT signal is fed to a built-in scaler in order to count the rate at which trigger is generated by the FTM. The  $T1_M$  signals as well as the FT signal are also latched internally. The latched data may be useful for debugging and commissioning of the module.

*Design features –  
bit-wise masking,  
deglitcher, scalers,  
latches*

The output signal of the FTM is shaped to a width of 160 ns with an external discriminator and is used to initiate the data acquisition system to record the event data.

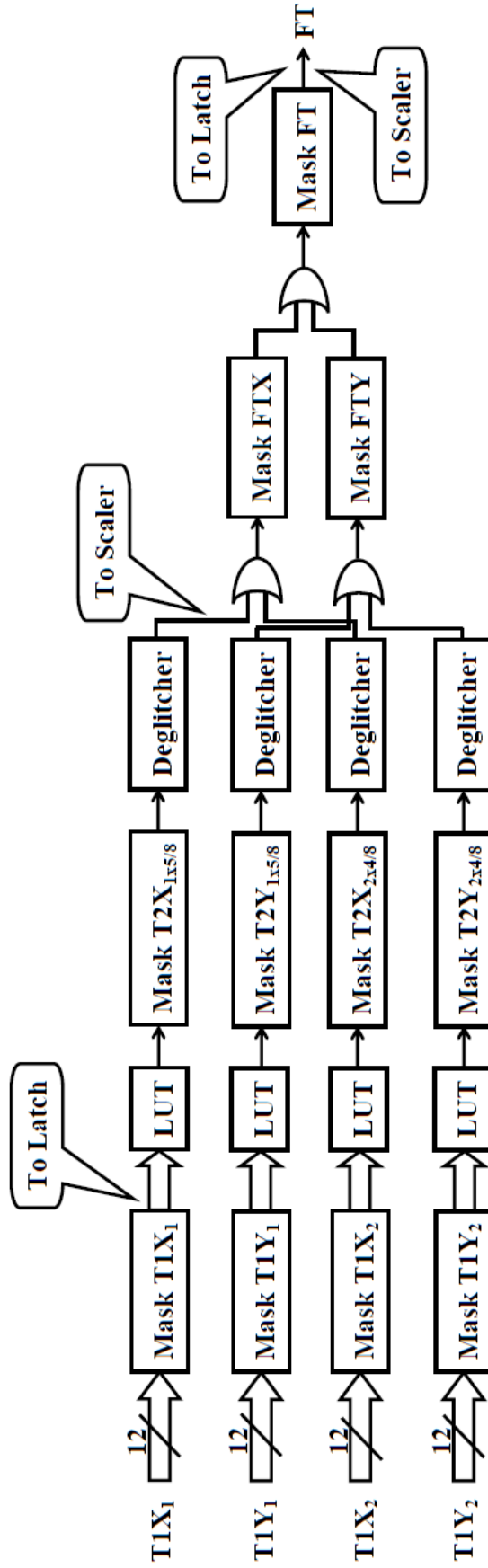


Figure 33: Schematic diagram of the design of the Final Trigger Module.

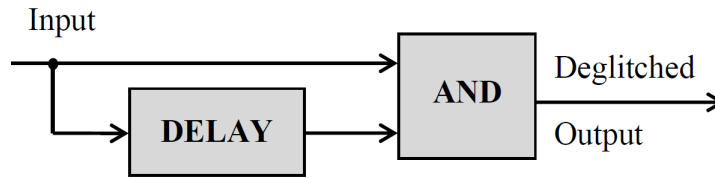


Figure 34: Schematic of the circuit used for deglitching the coincidence signals.

### 3.4 PERFORMANCE VALIDATION

The reliability of the FPGA-based design is assessed by evaluating the performance of the FTM in the prototype detector. This is carried out in two phases. The fraction of spurious or false triggers generated by the FTM is first estimated. Secondly, the trigger inefficiency or the fraction of genuine events missed by the FTM is determined. The FTM should exhibit a minimal fraction of spurious triggers as well as trigger inefficiency to ensure that similar design technique can be employed for the trigger system of a low event rate experiment like ICAL.

*Two-stage validation*

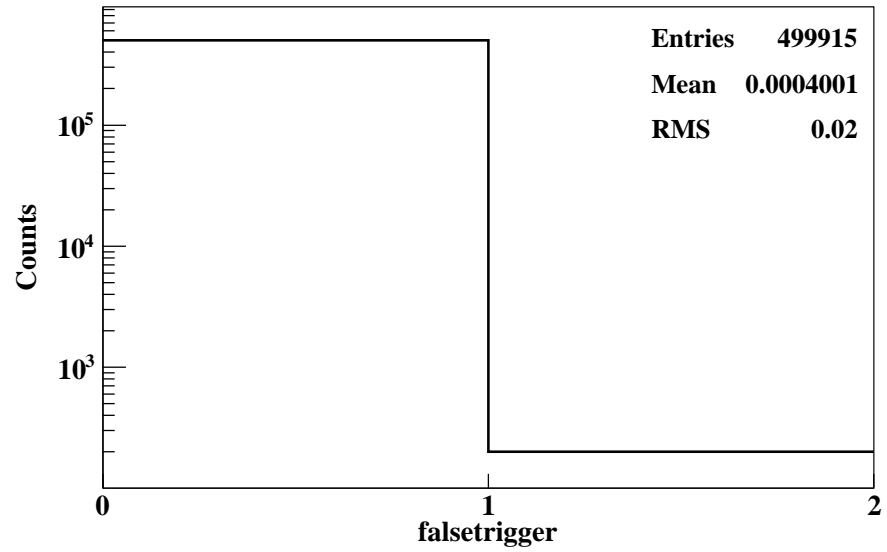
#### 3.4.1 False triggers

In the first step, the FTM is used to generate the trigger for the prototype detector. The event data recorded are analysed offline to look for false triggers. The events for which the hit pattern does not satisfy the trigger criteria but trigger is generated by the FTM are counted as false triggers.

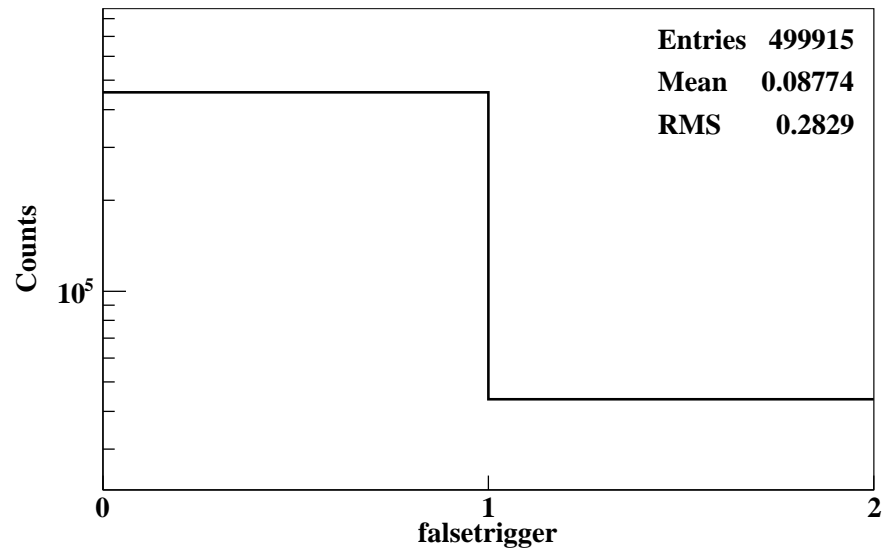
Typical RPC pulses, after being amplified using pre-amplifiers, have amplitude of about 150 mV, with negative polarity, across a 50  $\Omega$  load. A discriminator threshold of -20 mV is used. Under the normal situation, the noise level of the detector is well below the threshold level and the average signal pick-up rate per RPC strip (100 cm  $\times$  3 cm) is about 60 Hz. The system is said to be stable and the false trigger rate is found to be less than 1%, under such a scenario, as shown in Fig. 35a.

*Spurious triggers < 1% when the system is stable*

However, the grounding and the shielding of the detector and the readout electronics was found to be inadequate due to some design limitations. As a result, occasionally, the external EMI elevates the ground level and the noise level becomes high enough to cross the discriminator threshold. The RPC noise rate goes up drastically in such a situation, resulting in an average strip pick-up rate of about 1 MHz. A maximum of 4 out of 12 RPCs in the prototype detector are observed to have an unstable behavior, i.e., their noise rates would fluctuate very often. The false trigger rate goes up to about 8 - 10% for such a noisy system, as can be seen in Fig. 35b.



(a)



(b)

Figure 35: Distributions of false trigger for the FTM with the system operating under (a) stable and (b) noisy situation. The flag *falsetrigger* is true (assigned value 1 in the plot) for an event whose hit pattern does not meet the trigger criteria and is false (assigned value 0 in the plot) otherwise. The false trigger rate is less than 1% when the system is stable but goes up to about 8 – 10% under noisy circumstances.

### 3.4.2 Missed triggers

The next step is to estimate the fraction of missed triggers or the trigger inefficiency of the FTM. Missed triggers are defined as those events whose hit pattern satisfy the trigger criteria but are missed by the FTM and hence are not recorded by the data acquisition system.

In order to determine the missed trigger rate for the FTM, the trigger signal for the data acquisition system is generated independently using a set of scintillator paddles. A total of 9 rectangular paddles, each of dimension 96 cm x 36 cm x 1 cm, have been used. The arrangement of the paddles is shown in Fig. 36.

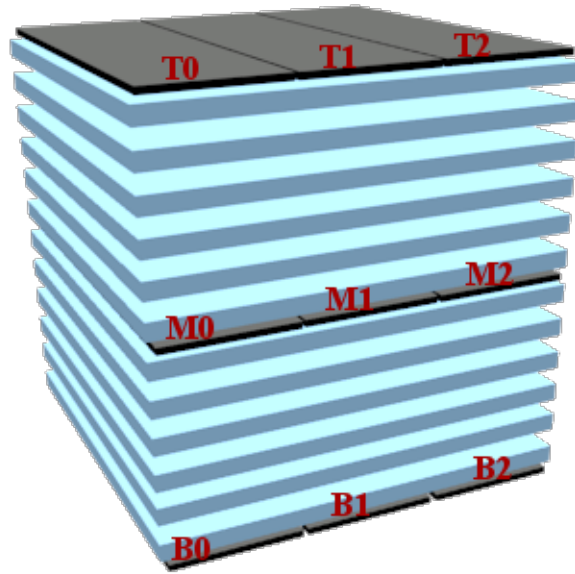


Figure 36: Arrangement of scintillator paddles for trigger generation in the prototype detector. There are total 9 paddles, each of dimension 96 cm x 32 cm x 1 cm, arranged in three layers. The bottom layer of paddles is placed below the bottommost RPC, the middle layer is placed on the middle (6th) RPC and the top layer is placed on the topmost RPC. The trigger signal for the data acquisition system is generated by combining the signals from the paddles.

The trigger signal for the data acquisition system is formed by combining the paddle signals according to the following logic.

$$\begin{aligned} \text{DAQ trigger} &= (\text{T}_0 \text{ OR } \text{T}_1 \text{ OR } \text{T}_2) \\ &\quad \text{AND } (\text{M}_0 \text{ OR } \text{M}_1 \text{ OR } \text{M}_2) \\ &\quad \text{AND } (\text{B}_0 \text{ OR } \text{B}_1 \text{ OR } \text{B}_2) \end{aligned} \quad (3.1)$$

*Configuration of  
paddle trigger*

Such trigger logic is chosen to ensure that the trigger signal is generated for a track incident at any angle and hitting any one of the paddles in each of the three layers and thereby covering the entire fiducial volume of the detector. The average trigger rate is found to be 6 – 8 Hz. The paddles are observed to have an average noise rate

of 100 Hz. The choice of the trigger logic also guarantees a negligible chance coincidence rate ( $\sim 10^{-5}$  Hz) which implies that the probability of generating a chance trigger, in such a scenario, is minimal.

*Trigger inefficiency*  
 $\sim 0.01\%$

The data acquisition system records the event data on receiving a paddle trigger. The data collected are analysed offline to check for events with sufficient hits to satisfy the trigger criteria for which trigger was not generated by the FTM. The response of the FTM for an event is obtained from the status of the latched FT signal corresponding to that event. The missed trigger rate is observed to be about 0.01%, as shown in Fig. 37a.

*Configuration of  
paddle trigger for  
diagonal tracks*

The paddle trigger is then generated only for tracks passing diagonally through the detector by combining the paddle signals as per the following logic.

$$\begin{aligned} \text{DAQ trigger} = & (\text{T}_0 \text{ AND } \text{M}_1 \text{ AND } \text{B}_2) \\ & \text{OR } (\text{T}_2 \text{ AND } \text{M}_1 \text{ AND } \text{B}_0) \end{aligned} \quad (3.2)$$

*Trigger inefficiency*  
 $\sim 0.04\%$

This has been done to evaluate the functioning of the module under extreme circumstances with tracks passing across the boundary of the RPCs. Fig. 37b illustrates that the missed trigger rate, in such a case, increases to about 0.04% which is still under the tolerable limit.

### 3.4.3 Coincidence rates and final trigger rate

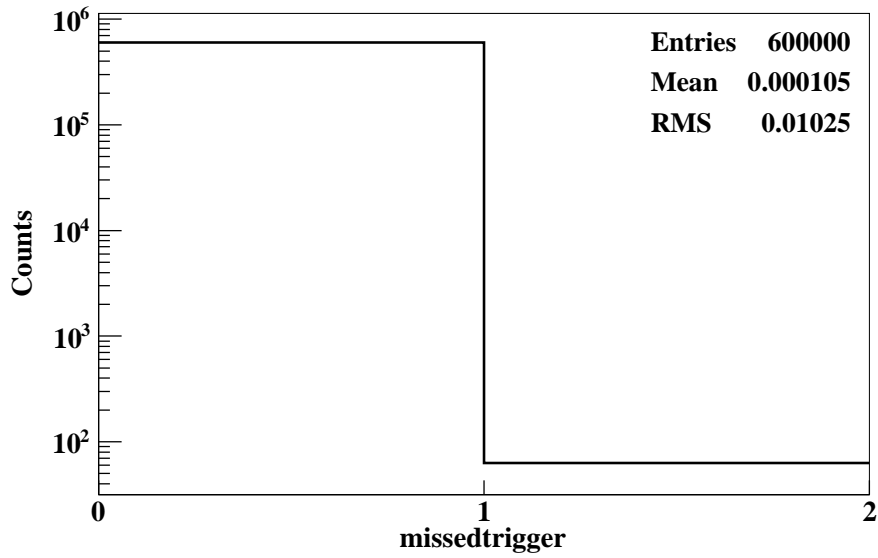
The rates for the four coincidence (T2) signals and the FT signal, as obtained from the FTM scalers, are shown in Fig. 38a and Fig. 38b respectively, for a counting period of 10 seconds. The FT signal is the combination of all the coincidence signals and hence the FT rate is observed to be higher than that of the individual coincidence signals. The RPC strips belonging to the Y-plane are found to have lower noise rates compared to the X-plane strips which explains the lower rates of the coincidence signals originating from the Y-plane relative to those from the X-plane. All the plots show few counts with values much higher than the mean value which can be attributed to the occasionally high chance coincidence rate as a result of correlated noise.

### 3.4.4 Additional inputs

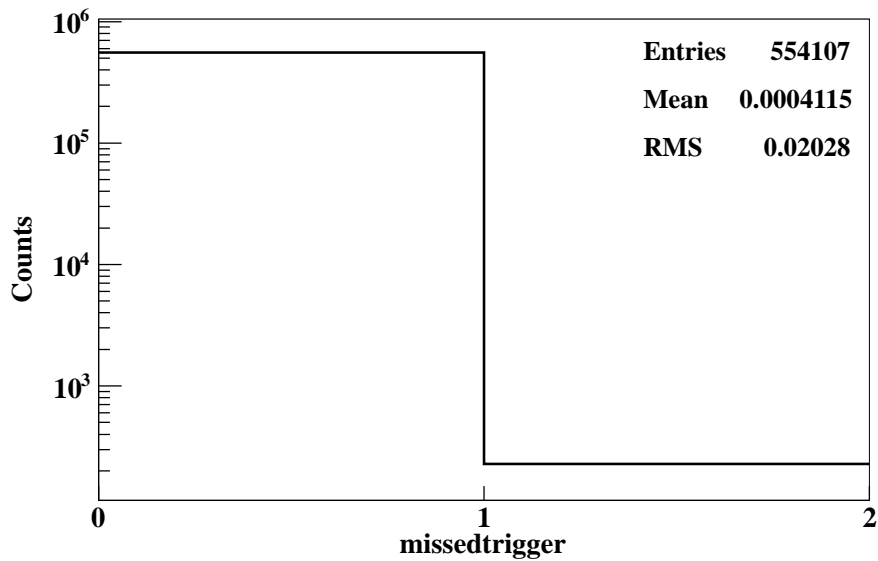
*All pre-trigger  
signals used as FTM  
input*

The aforesaid results are obtained with two sets of trigger criteria, as mentioned in Section 3.3. The performance of the FTM is also evaluated with four sets of trigger criteria, as listed below, where the all four T1<sub>M</sub> signals are used as inputs to the FTM.

- (i) 1x5/8
- (ii) 2x4/8
- (iii) 3x3/8
- (iv) 4x2/8

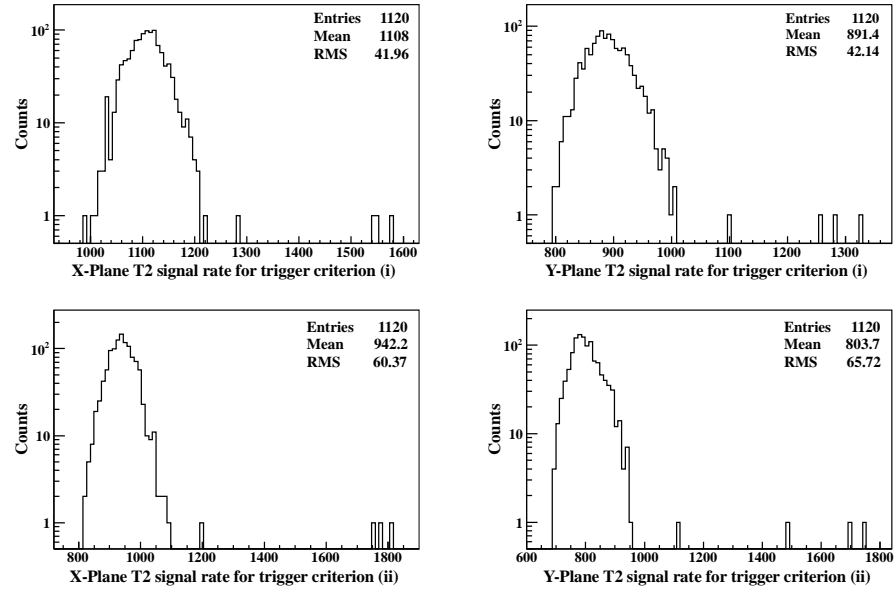


(a)

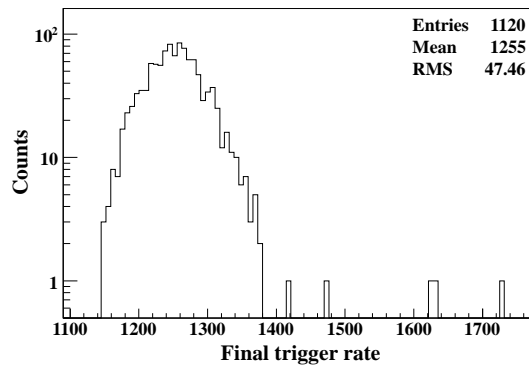


(b)

Figure 37: Distributions of missed trigger for the FTM with paddle trigger generated according to (a) Eq. 3.1 and (b) Eq. 3.2. The flag *missedtrigger* is true (assigned value 1 in the plot) in case the event hit pattern meets the trigger criteria but trigger is not produced by the FTM and is false (assigned value 0 in the plot) otherwise. The missed trigger rate is about 0.01% in case (a) and increases to about 0.04% in case (b).



(a)



(b)

Figure 38: Rates for (a) the coincidence (T2) signals and (b) the final trigger (FT) signal of the FTM for a counting period of 10 seconds. The FT signal is the combination of all the coincidence signals and hence the FT rate is observed to be higher than that of the individual coincidence signals. The RPC strips belonging to the Y-plane are found to have lower noise rates compared to the X-plane strips which explains the lower rates of the coincidence signals originating from the Y-plane relative to those from the X-plane. The presence of a few counts with values much higher than the mean value, in all the plots, can be attributed to the occasionally high chance coincidence rate as a result of correlated noise.

The additional inputs are accommodated using mezzanine cards on the CAEN V1495 board. In case of muon events, the 3-Fold and the 4-Fold signals mostly result from correlated noise. The false trigger rate is observed to increase to about 2% while the missed trigger rate is found to be around 0.03%, under such circumstances. The rates of the coincidence signals as well as the final trigger signal, recorded by the FTM scalers, demonstrate similar trend as discussed in Section 3.4.3.

Hence, the FPGA-based trigger module is working satisfactorily in the prototype detector, with negligible fraction of spurious triggers and trigger inefficiency when the system is operating in stable condition. The performance validation of the trigger module offers a proof of principle that such design technique can be successfully and reliably used for implementing the trigger system for the ICAL detector.



## IMPLEMENTATION LAYOUT OF THE ICAL TRIGGER SYSTEM

The layout for the implementation of the trigger system for one module of the ICAL detector is presented in this chapter. The overall latency involved in trigger generation is estimated. Results from a study carried out to assess the feasibility of a signal transmission scheme, to be employed for transmitting the trigger signals for the ICAL detector, are discussed. A technique for calibrating the delay offsets associated with the return-path of the trigger signal, which is crucial for proper timing measurement, is also proposed.

*Chapter  
summary*

### 4.1 TRIGGER SYSTEM LAYOUT

The layout for implementation of the ICAL trigger system is illustrated in Fig. 39, which has been devised in compliance with the proposed architecture of the trigger scheme.

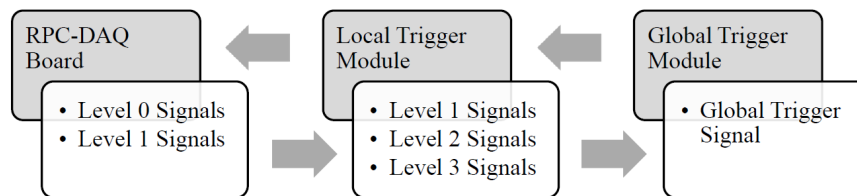


Figure 39: Layout for implementation of the ICAL trigger system and the signals associated with each level of trigger generation.

The RPC level trigger signals are processed in the trigger section of the RPC-DAQ board where the RPC strip signals are combined to form the Level 0 and the Level 1 trigger signals. The next level in the implementation hierarchy is the segment trigger station, namely, the Local Trigger Module (LTM). The LTM takes the pre-trigger signals produced by the RPC-DAQ board of each constituent RPC of the segment as input and finally generates the Level 3 or local trigger signals for the X and the Y plane, based on the trigger criteria. The Global Trigger Module (GTM) receives the output of all the LTMs and produces the global trigger signal for the detector module. The global trigger signal is fed back to the RPC-DAQ boards of all constituent RPCs of the detector module, via the respective LTMs, for the purpose of recording the event data.

*Implementation  
layout conforms to  
the proposed  
architecture of the  
trigger scheme*

The RPC-DAQ board is mounted inside the RPC unit. The physical placement of the LTMs and the GTM should conform to the mechanical constraints associated with the detector structure in order to ensure the

*2 alternate schemes  
for placement of  
trigger modules*

feasibility of implementation of the trigger scheme. Since the global trigger signal will be used for latching the event data in the RPC-DAQ board, an estimate of the latency involved in trigger generation is essential for determining parameters like, minimum width of shaped strip pulses, full scale range of TDC, etc., and also the dead time of the data acquisition system. Moreover, this is necessary to fix the width of the coincidence window for trigger generation. The trigger latency and the coincidence window are determined by the delay incorporated in the processing as well as the propagation of the signal through various levels of the trigger system. Two alternate schemes have been considered for the placement of the LTMs and the trigger latency and the coincidence window width have been estimated in both the cases.

#### 4.1.1 Scheme A

*LTMs on the  
detector face and  
GTM at the back-end*

Fig. 40 shows the placement of the LTMs and the GTM under scheme A. The LTMs are placed on the front as well as the back face of the detector, i.e., the faces located on opposite sides, perpendicular to the direction of the road. The GTM is placed along with the back-end system at one corner of the detector module.

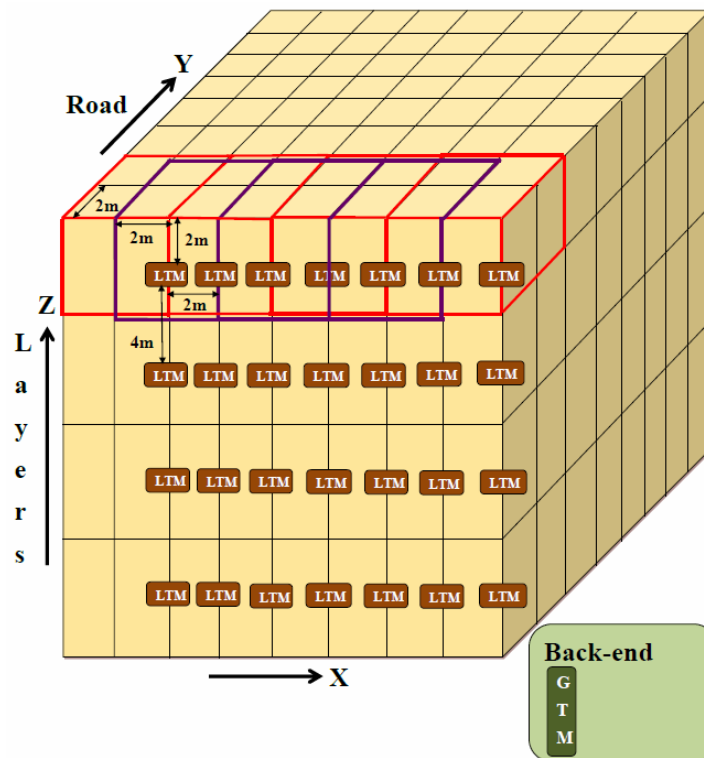


Figure 40: Placement of the trigger modules under Scheme A. The LTMs are placed on the front as well as the back face of the detector, i.e., the faces located on opposite sides, perpendicular to the direction of the road. The GTM is placed along with the back-end system at one corner of the detector module.

The maximum routing and the processing delays involved in different stages of generation of the local trigger signal are listed in Table 8. Henceforth, two different approaches for latching the event data have been taken into consideration.

PATH	DELAY (ns)
Cable length from RPC front-end to RPC-DAQ board : 3 m	15
Processing in RPC-DAQ board	20
Cable length from RPC-DAQ board to LTM : 10 m	50
Track length (diagonal-length for a volume of 4 m x 4 m x 1 m) : 6 m	20
Fan-out generation (max. 3 stages)	60
Cable length for fan-out : 5 m (max.)	25
Processing in LTM	50
Delay introduced for de-glitching	20
Tolerance	30
Net delay in local trigger generation	290

Table 8: Various delays incorporated in local trigger generation under Scheme A. The tolerance is taken as ~10% of the total delay.

#### 4.1.1.1 Event data latch with local trigger

The local trigger signal generated at the segment level is fed back to the RPC-DAQ boards of the constituent RPCs of that segment as well as the neighboring segments for recording the strip hit profile and the timing information. One segment can have a maximum of 26 neighboring segments, 8 in the same layer and 9 in each of the layers located above and below. Hence the generation of a single local trigger signal will initiate the latching of data in a total of 27 segments.

The current scheme of integration suggests that the RPCs belonging to each half-road of the detector module will be handled through the nearest detector face (front or back). Hence, mechanical constraints will arise in handling the segments lying across the half-road boundary of the detector module. Table 9 shows the trigger latency assuming that there are no LTMs for the segments lying across the half-road border and no interconnection exists between the segments lying on opposite halves of the road.

The concept of dividing the detector into two independent halves across the road might be helpful in avoiding lot of integration issues. Nevertheless, it poses serious risk toward losing some genuine events of interest which are distributed over the segments lying across the

*Difficulty in  
handling segments  
lying across the  
half-road boundary*

PATH	DELAY (ns)
Generation of local trigger	290
Propagation of local trigger from LTM output to RPC-DAQ board : 16 m	80
Tolerance	40
Local trigger latency	410

Table 9: Local trigger latency considering no LTMs for the segments lying across the half-road boundary and no interconnection between the segments lying on opposite halves of the road.

half-road border. The trigger latency is estimated with the assumption that the segments lying across the half-road boundary can be handled using respective LTMs, overcoming the mechanical constraints. The maximum cable length from the RPC-DAQ board to the LTM sitting on the detector face, in this case, will be 14 m, i.e., the net delay in generating the local trigger signal will be 310 ns. The maximum length of the return path of the local trigger signal from the LTM to the RPC-DAQ board can be 32 m or 48 m depending on whether the cable is routed through the road or around the detector. The maximum trigger latency in this case is shown in Table 10.

PATH	DELAY (ns)
Generation of local trigger	310
Propagation of local trigger from LTM output to RPC-DAQ board : 32 m / 48 m	160 / 240
Tolerance	50
Local trigger latency	520 / 600

Table 10: Local trigger latency assuming that it is possible to handle the segments lying across the half-road boundary using respective LTMs, overcoming the mechanical constraints.

*Issues with multiple triggers and signal routing*

However, in either of the cases, multiple segments may generate local trigger signal in the case of a long track and hence multiple triggers may be fed to one RPC-DAQ board for the same event. The system should be capable of handling such situation. Moreover, there will be lot of interconnections between neighboring segments which might cause difficulty in signal routing.

#### 4.1.1.2 Event data latch with global trigger

The global trigger signal generated at the module level by combining the local trigger signals from the constituent segments of the detector

is fed back to all the LTMs. Each LTM will, in turn, transmit the global trigger signal to the RPC-DAQ boards of the constituent RPCs of the segment for recording the event data. The longest path for the propagation of the local trigger signal from the LTM output to the GTM input will be approximately 50 m. Table 11 shows the corresponding global trigger latency.

PATH	DELAY (ns)
Generation of local trigger	310
Propagation of local trigger from LTM output to GTM input : 50 m	250
Processing in GTM	25
Propagation of global trigger from GTM output to LTM input : 50 m	250
Fan-out generation	25
Propagation of global trigger from LTM output to RPC-DAQ board : 10 m	50
Tolerance	90
Global trigger latency	1000

Table 11: Global trigger latency under Scheme A.

The use of global trigger signal for latching the event data offers higher trigger latency than that using the local trigger signal. However, the former approach is advantageous as it avoids multiple triggers for an event and also the need of interconnections between adjacent segments which eliminates lot of signal routing issues.

*Overcomes signal routing and multiple trigger issues*

#### 4.1.1.3 Coincidence window

The maximum relative delay between the input signals of an LTM, incorporated in different stages of the propagation of the pre-trigger signals from the output of the RPC-DAQ board up to the LTM input, is shown in Table 12. Hence, a coincidence window of width  $\sim 200$  ns needs to be used for the generation of the Level 2 trigger signal in the LTM.

*Coincidence window of width  $\sim 200$  ns necessary*

#### 4.1.2 Scheme B

The implementation of Scheme A should ensure that it does not offer any obstruction to the movement of the RPCs in and out of the detector which makes the available physical space for positioning the LTMs too much stringent. Moreover, a number of mechanical issues related to the handling of the segments lying across the half-road boundary

PATH	DELAY (ns)
Cable length difference from RPC-DAQ board to LTM : 6 m (horizontal) + 6 m (vertical) = 12 m	60
Track length (diagonal-length for a volume of 4 m x 4 m x 1 m) : 6 m	20
Fan-out generation (max. 3 stages)	60
Cable length for fan-out : 5 m (max.)	25
Tolerance	20
Net relative delay between LTM inputs	185

Table 12: Maximum relative delay between LTM input signals under Scheme A, which implies that a coincidence window of width  $\sim 200$  ns needs to be used for the generation of the Level 2 trigger signal.

*LTM along with  
GTM at the back-end  
– more convenient for  
integration purpose*

need to be resolved. An alternate scheme is to place the LTMs and the GTM along with other back-end modules at one end of the detector, as illustrated in Fig. 41. This scheme offers much more flexibility towards the physical placement of the trigger modules and simultaneously adapts to the structural constraints of the detector but at the expense of driving the pre-trigger signals over longer distance. The convenience of integration thus favours Scheme B over Scheme A.

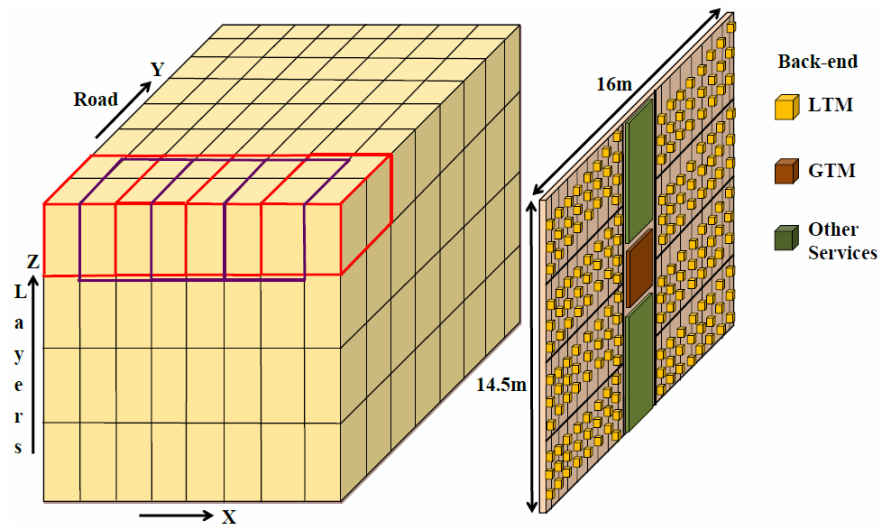


Figure 41: Placement of the trigger modules under Scheme B. The LTMs as well as the GTM are placed at one end of the detector, which offers the maximum physical space for positioning the trigger modules and also adapts to the structural constraints of the detector.

Various routing and processing delays involved in the generation of the local trigger signal are listed in Table 13. Hereafter, two approaches are considered for latching the event data, similar to scheme A.

PATH	DELAY (ns)
Cable length from RPC front-end to RPC-DAQ board : 3 m	15
Processing in RPC-DAQ board	20
Cable length from RPC-DAQ board to LTM input : 50 m	250
Track length (diagonal length for a volume of 4 m x 4 m x 1 m) : 6 m	20
Fan-out generation (max. 3 stages)	60
Cable length for fan-out : 5 m (max.)	25
Processing in LTM	50
Delay introduced for de-glitching	20
Tolerance	50
Net delay in local trigger generation	510

Table 13: Various delays incorporated in local trigger generation under Scheme B.

#### 4.1.2.1 Event data latch with local trigger

Table 14 shows the trigger latency when the local trigger signal generated at the LTM output is fed back to the RPC-DAQ boards of the constituent RPCs of the segment as well as the neighboring segments for registering the event data. Some issues associated with the use of local trigger signal, as mentioned in Section 4.1.1.1, are likely to arise here too.

PATH	DELAY (ns)
Generation of local trigger	510
Propagation of local trigger from LTM output to RPC- DAQ board : 55 m	275
Tolerance	80
Local trigger latency	865

Table 14: Local trigger latency under Scheme B.

#### 4.1.2.2 Event data latch with global trigger

The trigger latency incurred when the global trigger signal produced at the GTM output is transmitted back to each RPC of the detector module, through the respective LTMs, for recording the event data, is shown in Table 15.

PATH	DELAY (ns)
Generation of local trigger	510
Propagation of local trigger from LTM output to input : 13 m	65
Processing in GTM	25
Propagation of global trigger from GTM output to LTM input : 13 m	65
Fan-out generation	25
Propagation of global trigger from LTM output to RPC-DAQ board : 50 m	250
Tolerance	100
Global trigger latency	1040

Table 15: Global trigger latency under Scheme B.

A comparison of the figures in Table 14 and Table 15 reveal that the latencies for the local and the global trigger signals are almost at par under this scheme. Thus, the global trigger signal is preferred over the local trigger signal for latching the event data since it helps to avoid the issues associated with the later approach, as discussed in Section 4.1.1.2. The global trigger latencies under Scheme A (Table 11) and Scheme B (Table 15) are also found to be comparable. Hence, Scheme B turns out to be superior to Scheme A as it helps circumventing lot of integration issues while offering similar trigger latency.

#### 4.1.2.3 Coincidence window

Table 16 shows the maximum relative delay between the input signals of an LTM which implies that the generation of the Level 2 trigger signal in the LTM will require a coincidence window of width  $\sim 200$  ns.

## 4.2 STUDY OF LVDS TRANSMISSION

It is evident from the discussions in Section 4.1 that, under the proposed trigger scheme, the trigger signals need to be driven over a path of length around 40 – 50 m for one module of the ICAL detector. It is decided to use the LVDS standard for transmitting the trigger signals because of the advantages offered by LVDS, like high speed, low EMI and less cost, in comparison with other standards. However, it also needs to be ensured that the signal characteristics are preserved well after being transmitted over such a long distance. A study has been undertaken by transmitting LVDS signal over different lengths of CAT5

*To assess reliability  
of LVDS standard  
for transmitting the  
trigger signals*

PATH	DELAY (ns)
Cable length difference from RPC-DAQ board to LTM : 8 m + 4 m = 12 m	60
Track length (diagonal-length for a volume of 4 m x 4 m x 1 m) : 6 m	20
Fan-out generation (max. 3 stages)	60
Cable length for fan-out : 5 m (max.)	25
Tolerance	20
Net relative delay between LTM inputs	185

Table 16: Maximum relative delay between LTM input signals under Scheme B, which indicates that the generation of the Level 2 trigger signal will require a coincidence window of width  $\sim 200$  ns.

cable and also using different input pulse widths and comparing the input and the output signal parameters.

#### 4.2.1 Experimental set-up

Fig. 42 describes the experimental set-up for studying LVDS transmission over long distance. The input and the output signal characteristics are studied at point 1 and 2 respectively, as shown in the figure. DS90C031BTM [84] and DS90C032BTM [85] chips have been used as LVDS driver and receiver respectively.

The following parameters have been studied for the signal at the transmitting as well as the receiving end.

- (i) Amplitude
- (ii) Pulse width
- (iii) Rise time
- (iv) Baseline
- (v) Input-output delay

Table 17 lists different values of the cable length and the pulse width of the input LVDS signal for which the measurements have been recorded.

PARAMETER	VALUES
Cable length (m)	25, 30, 35, 40, 45, 50
Pulse width of input LVDS signal (ns)	10, 25, 50, 75, 100, 125, 150

Table 17: Different cable lengths and input pulse widths used in the study.

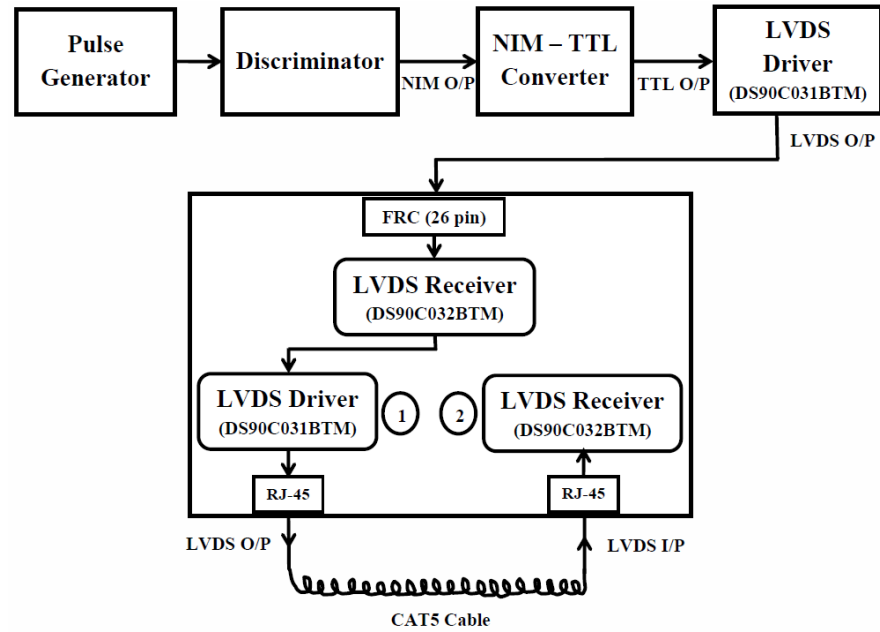


Figure 42: Experimental set-up to study LVDS transmission using different lengths of CAT5 cable and different input pulse widths. The input and the output signal characteristics are studied at point 1 and 2 respectively.

#### 4.2.2 Results

Screenshots of the input and the output pulses, both LVDS and TTL, for a cable length of 40 m and input pulse width of 100 ns are shown in Fig. 43. The signal amplitude remains almost unchanged and the baseline is observed to be stable.

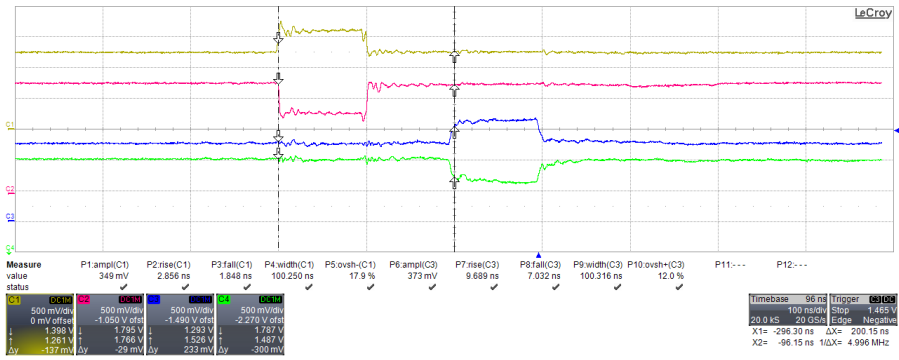
However, a too narrow input pulse results in the formation of triangular pulse at the output as the rise time of the output pulse, which is determined by the capacitance of the cable, becomes larger than the input pulse width. Fig. 44 shows the input-output pulses for a cable length of 50 m and input pulse width of 25 ns, which correspond to this scenario.

Fig. 45 shows the input-output delay ( $\delta$ ) as a function of cable length ( $L$ ) for an input LVDS pulse width of 100 ns. The average delay per unit cable length, obtained by fitting the data to a straight line, is about 5 ns/m, which matches well with the value quoted in literatures [16]. Similar value is obtained for other pulse widths also. The delay vs. cable length characteristics for different input pulse widths is shown in Fig. 46.

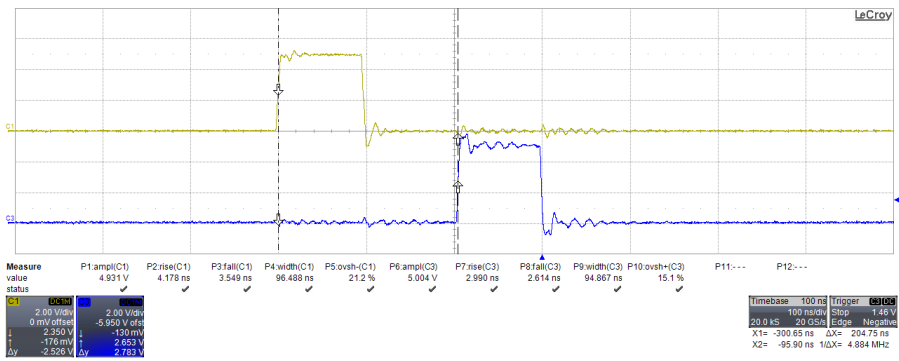
The deviation ( $\delta_r$ ) of the input-output delay from an estimated value, assuming the average delay per unit cable length to be 5 ns/m [16], as a function of cable length ( $L$ ) for different input pulse widths, is shown in Fig. 47. The maximum deviation is observed to be within  $\pm 2$  ns.

*Triangular pulse at the output for too narrow input pulse*

*Average delay per unit cable length obtained as 5 ns/m*

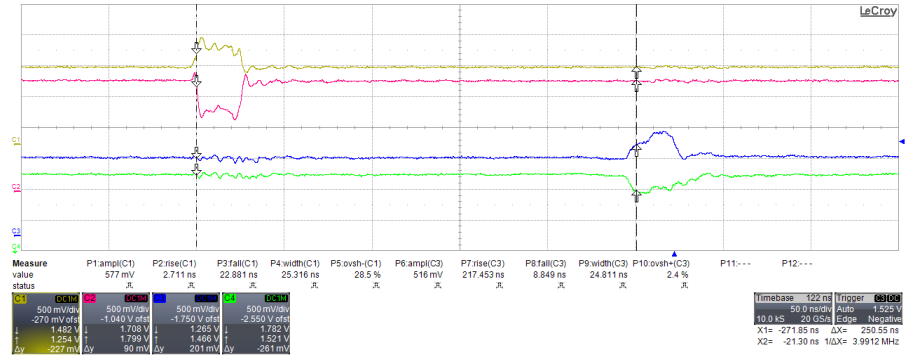


(a)

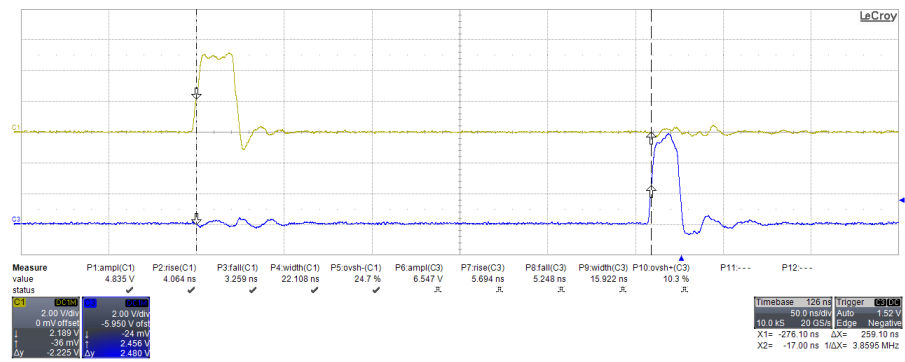


(b)

Figure 43: (a) LVDS and (b) TTL input-output pulses for a cable length of 40 m and input pulse width of 100 ns.



(a)



(b)

Figure 44: (a) LVDS and (b) TTL input-output pulses for a cable length of 50 m and input pulse width of 25 ns. A too narrow input pulse results in the formation of triangular pulse at the output whose rise time, determined by the cable capacitance, becomes larger than the input pulse width.

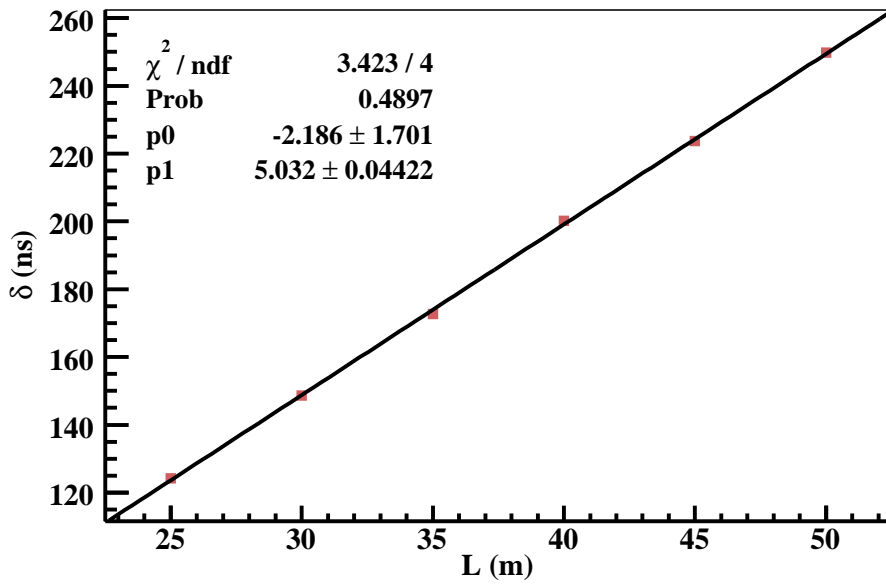


Figure 45: Input-output delay ( $\delta$ ) as a function of cable length (L) for input LVDS pulse width of 100 ns. The average delay per unit cable length is about 5 ns/m.

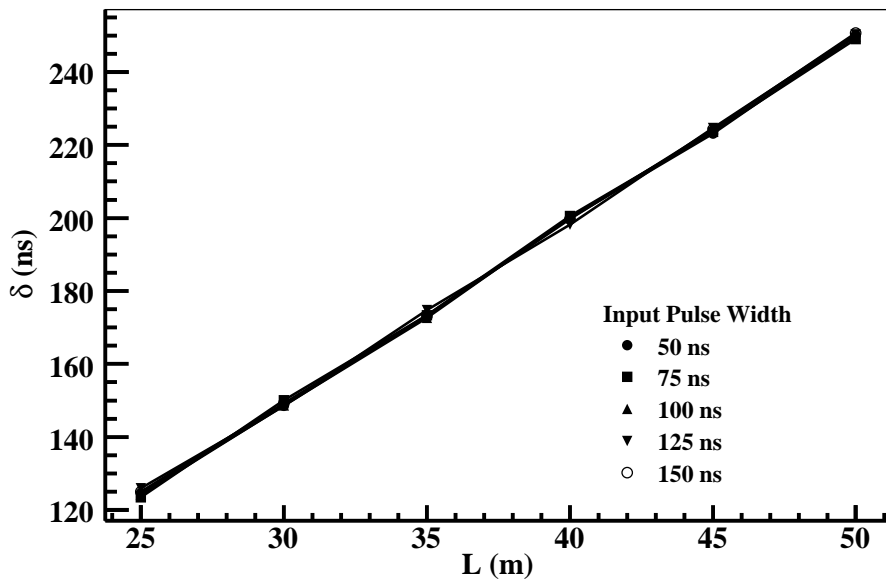


Figure 46: Variation of the input-output delay ( $\delta$ ) with cable length (L) for different input LVDS pulse widths.

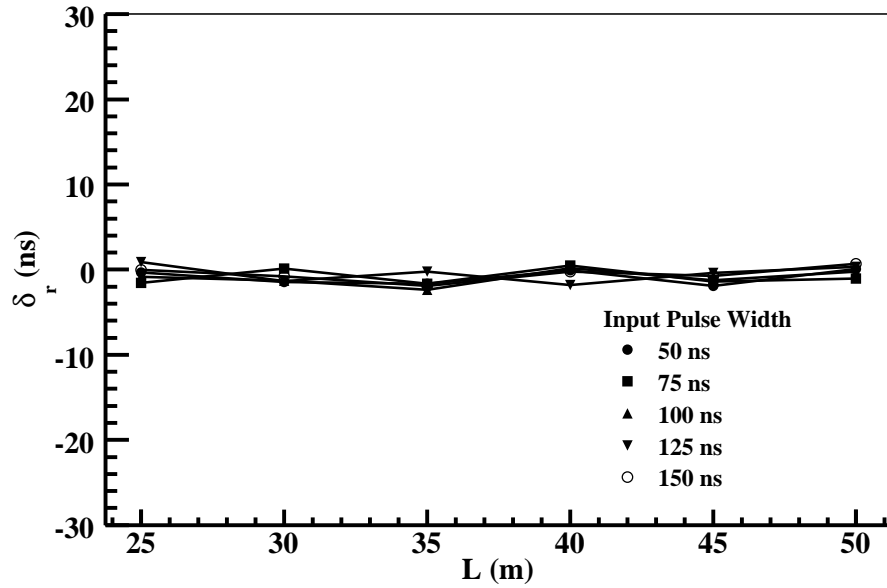


Figure 47: Deviation ( $\delta_r$ ) of the input-output delay from an estimated value, assuming the average delay per unit cable length to be 5 ns/m, as a function of cable length (L) for different input LVDS pulse widths. The maximum deviation is observed to be within  $\pm 2$  ns.

*Rise time of LVDS output goes up and output TTL pulse becomes narrower with cable length*

Fig. 48 shows the variation of the rise time ( $t_r$ ) of the LVDS output with cable length (L). A longer cable offers larger capacitance and hence the rise time increases with increase in the cable length. The difference of the input and the output TTL pulse widths ( $\Delta_{PW}$ ) as a function of cable length (L) is shown in Fig. 49. Due to the increase in the rise time of LVDS output with cable length, the corresponding TTL pulse becomes narrower and hence the difference goes up.

### 4.3 DELAY OFFSET CALIBRATION

*Synchronization of global trigger paths or calibration of delay offsets essential for proper timing measurement*

The global trigger signal will be used as the reference for the measurement of timing of the RPC signals in the RPC-DAQ board which will provide information about the directionality (upward or downward) of the tracked particle. However, the return-paths of the global trigger signal from the output of the GTM to the input of different RPC-DAQ boards vary widely in length due to the vast volume of the detector. Proper timing measurement, therefore, necessitates either complete synchronization of the return-paths of the global trigger signal or accurate estimation of the corresponding delay offsets.

*Synchronization through active or passive delay compensation*

The synchronization can be achieved using either passive or active delay compensation technique. Passive delay compensation employs cables of identical length to transmit the global trigger signal from the GTM to different RPC-DAQ boards. This will, however, lead to accumulation of cables in huge excess in the detector which might

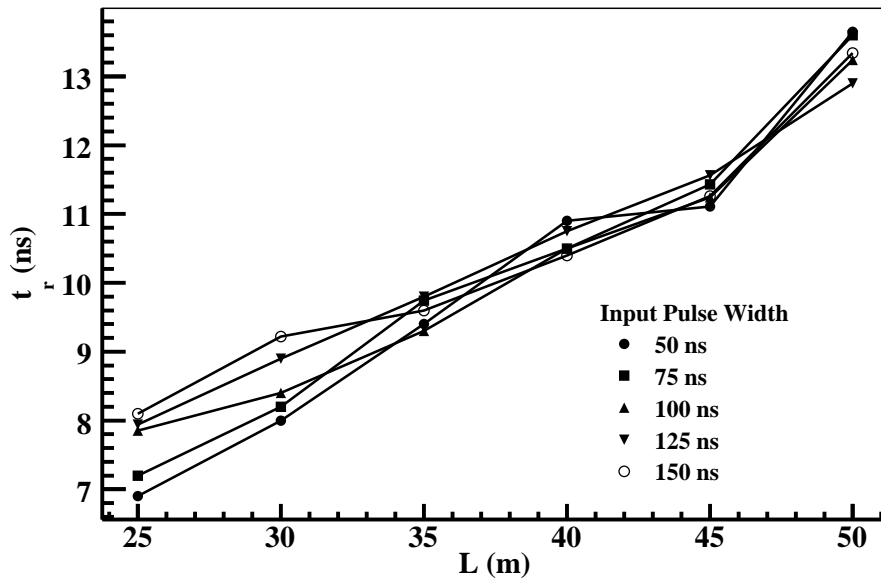


Figure 48: Variation of rise time ( $t_r$ ) of LVDS output with cable length ( $L$ ). A longer cable offers larger capacitance and hence the rise time of the output signal increases with cable length.

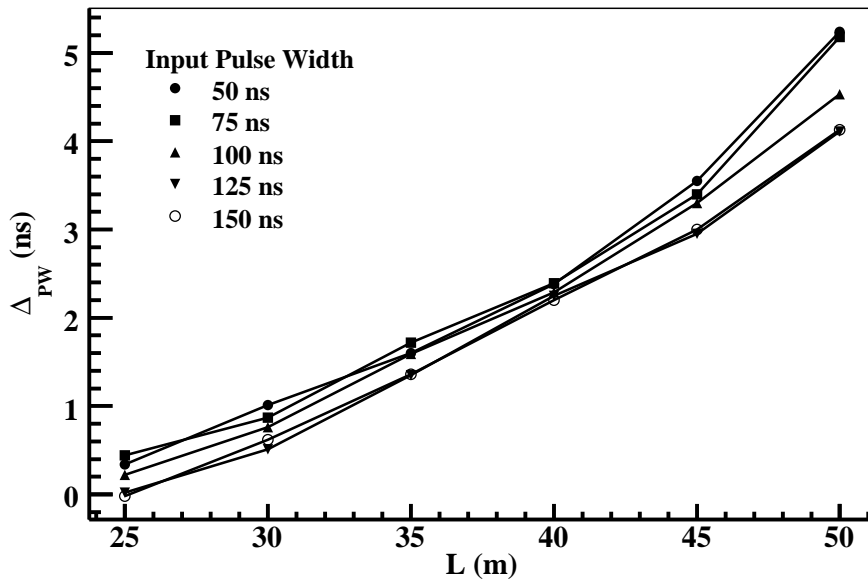


Figure 49: TTL input-output pulse width difference ( $\Delta_{PW}$ ) as a function of cable length ( $L$ ). Due to the increase in the rise time of LVDS output with cable length, the output TTL pulse becomes narrower and hence the difference goes up.

give rise to integration issues. Active delay elements can also be used to compensate the unequal delays experienced by the global trigger signal in different paths. Nevertheless, it needs to be ensured that this does not introduce additional timing jitter of more than 100 ps since the least count of the TDC will be about 200 ps [81].

Another alternative is to calibrate the delay offsets associated with different return-paths of the global trigger signal through an intensive calibration process. The offsets, thus estimated, can be incorporated in the analysis to obtain the exact timing of the RPC signals. The concept of calibration is preferred over that of synchronization as it helps to avoid integration problems and also does not contribute to the timing jitter.

Fig. 50 illustrates the proposed technique for delay offset calibration which involves different levels of the trigger system. The RPC-DAQ board has a pair of signals, one input and another output, for the purpose of calibrating the associated delay offset. The GTM generates the calibration signals which are fed to the LTMs and simultaneously used as the *Start* signals for a TDC. The delay offsets for the constituent RPCs of an LTM are calibrated sequentially using a multiplexer and a demultiplexer, both having the same select lines and thus handling the same RPC-DAQ board at a time. The LTM receives the input calibration signal from the GTM and sends it to the RPC-DAQ board selected by the demultiplexer. The RPC-DAQ board sends an output calibration signal back to the LTM, on receiving the input calibration signal. The LTM, in turn, transmits the calibration signal received from the RPC-DAQ board to the GTM, using the multiplexer. The input calibration signals received by the GTM from the LTMs are used as the *Stop* signals for the TDC. The time-intervals between the respective *Start* and *Stop* signals, recorded by the TDC, give an estimate of the delay offsets associated with the corresponding RPC for each LTM. The delay offset for one RPC per LTM is calibrated at a time and repetitive cycles complete the calibration process for all the constituent RPCs of the detector.

*Delay offset calibration favoured over synchronization*

*Delay offset calibration using different stages of trigger system*

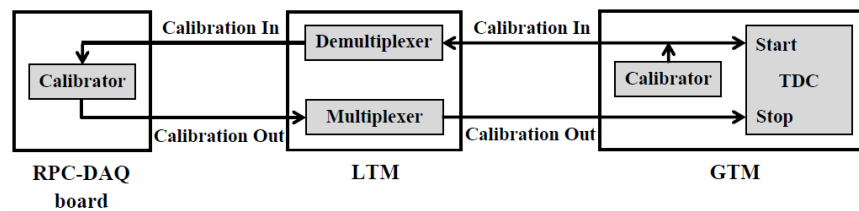


Figure 50: Proposed technique for delay offset calibration.

Different options have been explored in designing the overall layout for implementing the trigger system for the ICAL detector. The scheme which stands out to be the optimal one in terms of satisfying the trigger system requirements as well as the integration constraints is

finally selected. Results from the study of LVDS transmission over long distance ensure that this standard can be reliably used for transmitting the trigger signals for the ICAL detector under the proposed trigger scheme. Finally, a technique for calibrating the delay offsets associated with the propagation of the global trigger signal, which is absolutely essential for accurate timing measurement, is contemplated. However, the reliability of the proposed technique can be determined only after its evaluation at the system level.



## DESIGN OF TRIGGER BOARDS FOR THE ICAL DETECTOR

---

A bigger prototype of the ICAL detector, known as the ICAL Engineering Module, is being constructed as a prelude to building the final detector. This will serve as a testbench for the development of various integral components, like RPCs, magnet, gas system, front-end electronics, data acquisition system, etc., which will be finally deployed in the ICAL detector. The trigger boards, proposed to constitute the ICAL trigger system, will be used to build the trigger system for the Engineering Module in order to authenticate their performance. This chapter conceives the board-level designs for the LTM and the GTM, the building blocks of the ICAL trigger system.

*Chapter  
summary*

### 5.1 THE ICAL ENGINEERING MODULE

The upcoming prototype of the ICAL detector, the Engineering Module, will be of dimension 8 m x 8 m x 2 m, having RPC units placed in 20 layers between alternate layers of iron plates. Each RPC layer will be made up of 16 RPC units and the detector will thus comprise a total of 320 RPC units. The iron plates and the RPC units will be identical to those which will be used in the final ICAL detector. The Engineering Module, like the ICAL detector, will be magnetized to a field of 1.3 T.

*20 RPC layers, each  
with 16 RPCs*

Fig. 51 is a schematic of the ICAL Engineering Module with top view of the magnet coils. Table 18 illustrates a comparative study of some important structural parameters of the Engineering Module and the ICAL detector.

Each of the intrinsic sub-systems of the detector, like gas system, front-end readout electronics, trigger and data acquisition system, etc., need to be initially validated in the Engineering Module before being administered in the ICAL detector.

### 5.2 TRIGGER SYSTEM LAYOUT FOR THE ENGINEERING MODULE

The layout for the implementation of the proposed trigger scheme for the ICAL detector is contemplated in Chapter 4, Section 4.1. The trigger system for the Engineering Module should be built in line with the proposed implementation layout in order to substantiate the feasibility of the same. Fig. 52 is a three-dimensional view of the logical segmentation of the Engineering Module with overlap between adjacent segments. Table 19 demonstrates a comparison of

*Trigger system for  
the Engineering  
Module a miniature  
version of the ICAL  
trigger system*

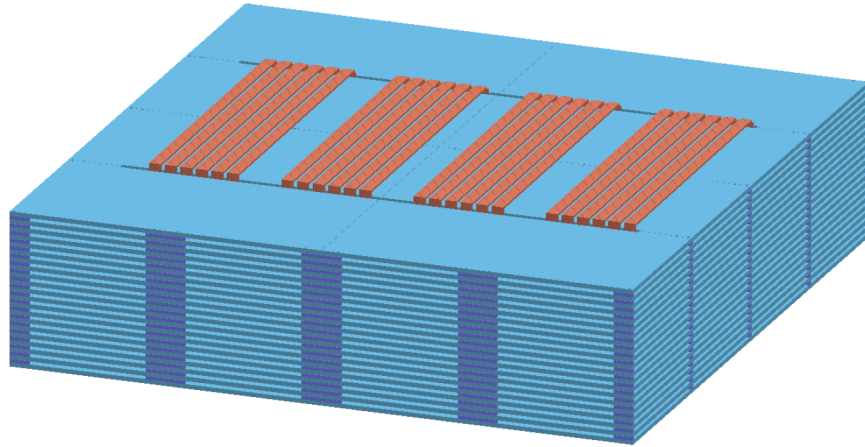


Figure 51: Schematic diagram of the ICAL Engineering Module (8 m x 8 m x 2 m) with top view of the magnet coils.

PARAMETERS	ICAL DETECTOR	ENGINEERING MODULE
Modules	3	1
Module dimension	16 m x 16 m x 14.5 m	8 m x 8 m x 2 m
Iron layers	151	21
Iron plate thickness	56 mm	56 mm
RPC layers	150	20
Gap for RPC units	40 mm	40 mm
RPC dimension	1800 mm x 1910 mm x 20 mm	1800 mm x 1910 mm x 20 mm
RPC units/ layer/ module	64	16
RPC units/ module	9600	320
Magnetic field	1.3 T	1.3 T

Table 18: Comparative study of the structural parameters of the Engineering Module and the ICAL detector.

some important parameters of the trigger system of the Engineering Module with those of the ICAL detector. Identical segment dimensions, with similar horizontal and vertical overlap, are used in both the cases to ensure that the construction of the ICAL trigger system can be accomplished by scaling up the same for the Engineering Module. Unlike the ICAL detector, it is not necessary to consider vertical overlap for the segments of the Engineering Module due to lesser number of layers. However, the design of the trigger boards have provisions to accommodate the requisite number of signals for vertical overlap to make the same compatible for the ICAL detector.

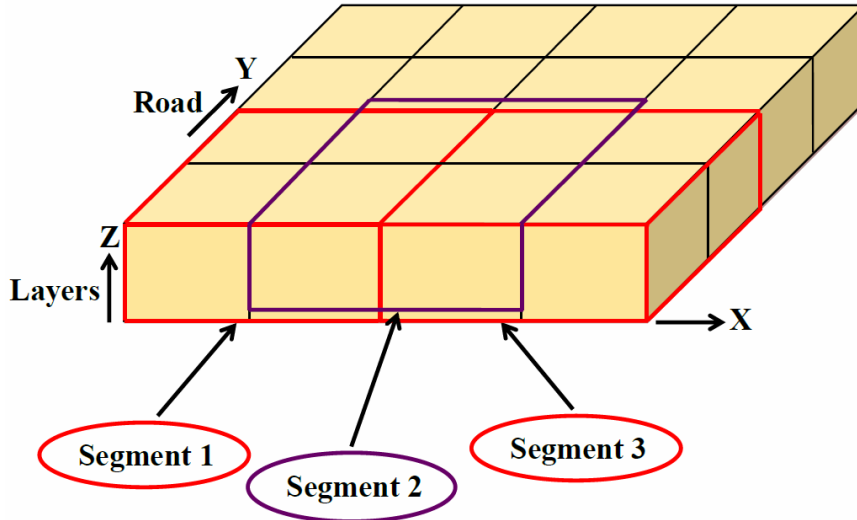


Figure 52: Three-dimensional view of the logical segmentation of the ICAL Engineering Module with overlap between adjacent segments. Overlap along only the X direction is shown here and similar overlaps exist in the Y and the Z directions as well.

PARAMETERS	ICAL DETECTOR	ENGINEERING MODULE
Segment dimension	4 m × 4 m × 2 m	4 m × 4 m × 2 m
RPC units/ segment (including vertical overlap of 7 layers)	27 × 4 = 108	27 × 4 = 108
Segments/ module	392	9
LTMs/ module	392	9
GTM/ module	1	1

Table 19: Comparison of the trigger system parameters of the Engineering Module with those of the ICAL detector.

*Trigger latency and coincidence window*

The placement of the LTMs and the GTM in the Engineering Module will be undertaken according to the Scheme B depicted in Chapter 4, Section 4.1.2. The event data will be latched in the RPC-DAQ board using the global trigger signal, rather than the local trigger signal, because of the obvious advantages, as mentioned in Chapter 4. Table 20 lists the various routing and processing delays involved in the generation of the local trigger signal. Table 21 shows the corresponding global trigger latency. The maximum relative delay between the LTM inputs is shown in Table 22, which indicates that a coincidence window of width  $\sim 200$  ns will be sufficient for the generation of the Level 2 trigger signal in the LTM.

PATH	DELAY (ns)
Cable-length from RPC front-end to RPC-DAQ board : 3 m	15
Processing in RPC-DAQ board	20
Cable-length from RPC-DAQ board to LTM input : 25 m	125
Track-length (diagonal length for a volume of 4 m x 4 m x 1 m) : 6 m	20
Fan-out generation (max. 3 stages)	60
Cable-length for fan-out : 5 m (max.)	25
Processing in LTM	50
Delay introduced for de-glitching	20
Tolerance	40
<b>Net delay in local trigger generation</b>	<b>375</b>

Table 20: Various delays incorporated in local trigger generation for the Engineering Module. The tolerance is taken as  $\sim 10\%$  of the total delay.

### 5.3 THE LOCAL TRIGGER MODULE

As discussed in Chapter 4, the LTM is the segment level trigger station which receives the pre-trigger signals from the RPC-DAQ boards of the constituent RPCs of the segment and generates the corresponding local trigger signal. The signal flow in the LTM is schematically shown in Fig. 53a.

Each RPC-DAQ board generates, in total, 8 Level 1 (T1) or pre-trigger signals, with 4 T1 signals per plane (Ref. Chapter 2, Section 2.3.1). The LTM needs to fan-out a part or whole of the T1 signals it receives, to the neighboring LTMs, in order to take care of overlap between adjacent segments. The LTM accepts user inputs to enable or

PATH	DELAY (ns)
Generation of local trigger	375
Propagation of local trigger from LTM output to GTM input : 4 m	20
Processing in GTM	25
Propagation of global trigger from GTM output to LTM input : 4 m	20
Fan-out generation	25
Propagation of global trigger from LTM output to RPC-DAQ board : 25 m	125
Tolerance	60
Global trigger latency	650

Table 21: Global trigger latency for the Engineering Module.

PATH	DELAY (ns)
Cable-length difference from RPC-DAQ board to LTM : 8 m + 2 m = 10 m	50
Track-length (diagonal length for a volume of 4 m x 4 m x 1 m) : 6 m	20
Fan-out generation (max. 3 stages)	60
Cable length for fan-out : 5 m (max.)	25
Tolerance	20
Net relative delay between LTM inputs	175

Table 22: Maximum relative delay between LTM input signals for the Engineering Module which implies that a coincidence window of width  $\sim 200$  ns is required for the generation of the Level 2 trigger signal.

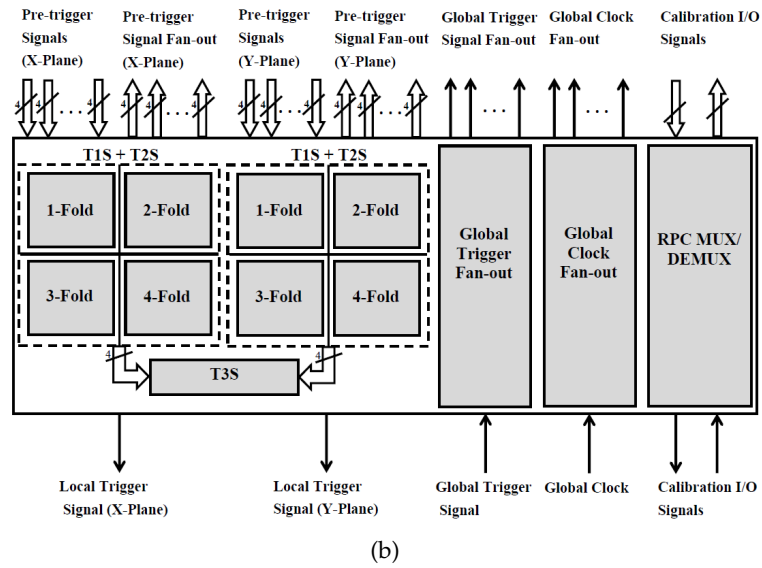
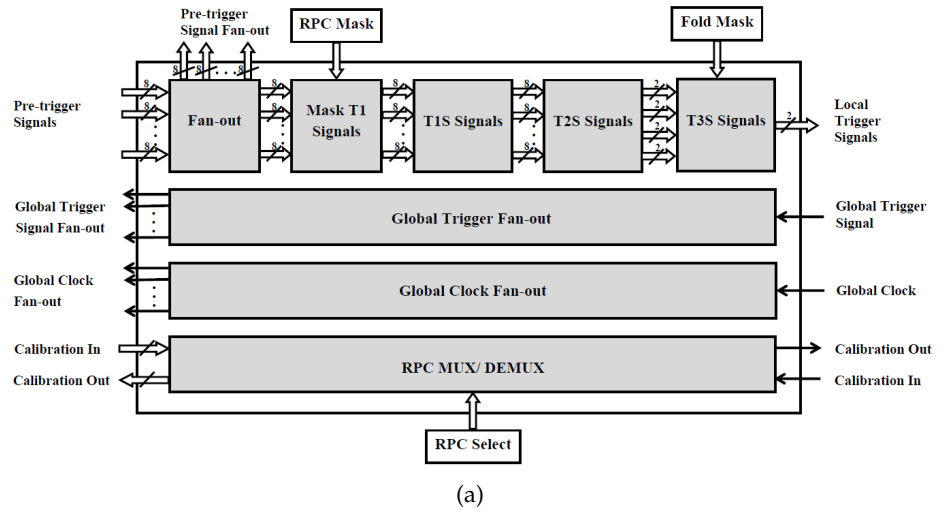


Figure 53: (a) Signal flow and (b) conceptual layout of different sub-sections in the LTM.

disable the T1 signals from any RPC or any intermediate coincidence signal. The Level 1 trigger (T1S) signal for a horizontal layer of the segment is obtained by combining the masked T1 signals belonging to the constituent RPCs of that layer. The Level 2 trigger (T2S) signal is produced for each plane provided the user-specified trigger criterion is satisfied by the corresponding T1S signals. Finally, the Level 3 (T3S) or local trigger signal is generated per plane by combining the masked T2S signals for different trigger criteria, belonging to the respective planes, and is fed to the GTM. The LTM receives the global trigger signal from the GTM and sends it back to the RPC-DAQ board of each constituent RPC of the segment for the purpose of recording the event data. The LTM also fans out the global clock received from the GTM to the constituent RPC-DAQ boards and participates in the calibration process. The proposed technique for delay offset calibration is discussed in Chapter 4, Section 4.3.

*Signal flow  
in the LTM*

It is desirable to implement all the functionalities of the LTM, as described above, in a single board to minimize interconnection issues. However, it is also not feasible to perform all the necessary operations using a single chip, mainly due to I/O pin constraints. Fig. 53b illustrates the conceptual layout of different sub-sections, each handling a specific operation, in the LTM board. There are 8 identical blocks, each of which receives the pre-trigger signal of a particular type from the constituent RPC-DAQ boards, generates the requisite number of fan-outs and produces the corresponding T2S signal. The formation of the local trigger signal and its transmission to the GTM is handled by another block. There are also individual blocks to deal with the distribution of each of the global trigger, global clock and calibration signals.

*Sub-sections in  
the LTM board*

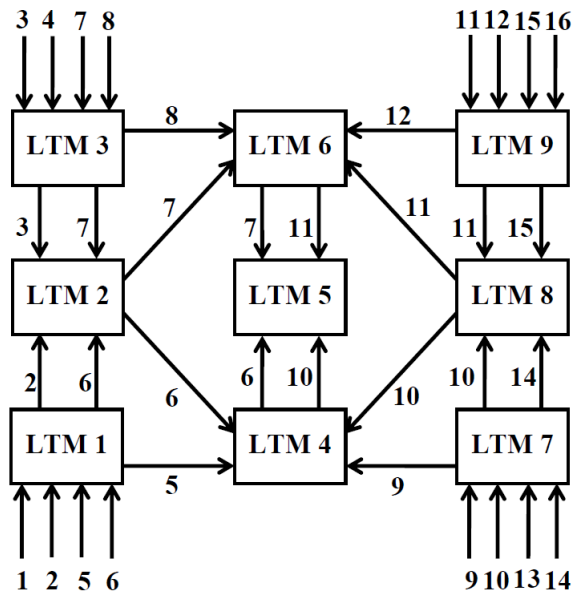
The 16 RPCs per layer of the Engineering Module constitute a  $4 \times 4$  matrix, as shown in Fig. 54a. The scheme for interconnecting and feeding the input signals to the LTMs is illustrated in Fig. 54b. Only 4 out of 9 LTMs receive the pre-trigger signals directly from the RPC-DAQ boards and fan out the same to the rest of the LTMs. The distribution of the global trigger, global clock and calibration signals, from the GTM to the individual RPC-DAQ boards, are carried out using these 4 LTMs alone, which are termed as type I LTMs. Rest of the 5 LTMs are involved only in the generation of the corresponding local trigger signal and are referred to as type II LTMs. Table 23 categorizes the LTM boards, shown in Fig. 54b, into two types.

*Scheme for  
interconnecting and  
feeding the input  
signals to the LTMs –  
2 types of LTM  
boards*

The current design of integration considers the pre-trigger signals from two RPCs along a road being carried out using the same cable assembly. The proposed scheme for LTM interconnection thus ensures that there is no need to split the cable before feeding the pre-trigger signals to the LTMs. Moreover, use of only a part of the LTMs for handling the global signals leads to improved synchronization of the same and also requires fewer calibration cycles.

4	8	12	16
3	7	11	15
2	6	10	14
1	5	9	13

(a)



(b)

Figure 54: (a) The  $4 \times 4$  matrix of 16 RPCs per layer of the Engineering Module and (b) the scheme for interconnecting and feeding input signals to the LTMs. The numbers at the LTM input and output denote the pre-trigger signals received and the fanned out respectively from the corresponding RPC. The proposed scheme for LTM interconnection conforms to the integration design, ensures improved synchronization of the global signals and also requires fewer calibration cycles.

CATEGORY	LTM	FUNCTION
Type I	LTM 1, LTM 3, LTM 7, LTM 9	Local trigger generation, distribution of global signals
Type II	LTM 2, LTM 4, LTM 5, LTM 6, LTM 8	Local trigger generation

Table 23: Categorization of the LTMs into two types based on functionality.

The I/O specifications for the LTM board are listed in Table 24 with the quoted figures representing the maximum requirement. All I/O signals will be transmitted using the LVDS standard.

#### 5.4 THE GLOBAL TRIGGER MODULE

As mentioned in Chapter 4, the GTM receives the local trigger signals from all the LTMs and generates the global trigger signal for the detector. The signal flow in the GTM is described in Fig. 55.

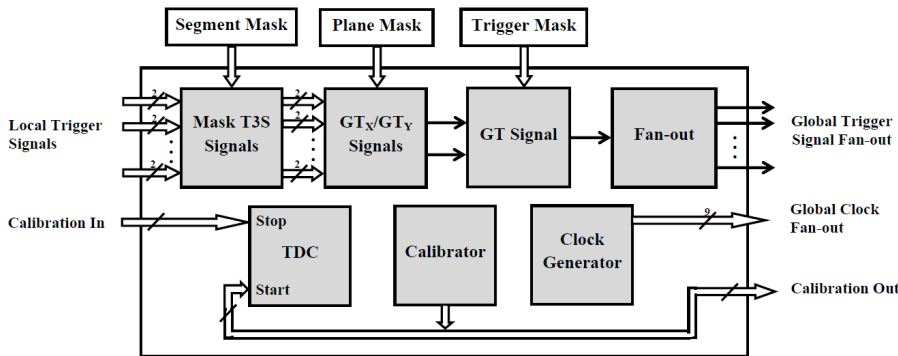


Figure 55: Signal flow in the GTM.

Each LTM generates two local trigger signals, one for each plane, and hence a total of 18 local trigger signals from 9 LTMs are fed as inputs to the GTM. The local trigger signal from any segment or the global trigger signal at any intermediate stage can be individually masked by the user. The global trigger ( $GT_X$  and  $GT_Y$ ) signal for the X and the Y plane are obtained by combining the masked local trigger signals, for the respective planes, from all the LTMs. The global trigger (GT) signal is generated as a final OR of the  $GT_X$  and the  $GT_Y$  signals. The GT signal is fed back to the 4 type I LTMs, which, in turn, transmit the same to the RPC-DAQ boards of all constituent RPCs of the detector for registering the event data. The GTM also generates the global clock and fans it out to each of the 9 LTMs and is involved in the calibration process. The proposed technique for delay offset calibration is discussed in Chapter 4, Section 4.3.

*Signal flow in the GTM*

Input signals	RPC-end (pre-trigger) : $27 \times 4 \times 8 = 864$
	RPC-end (calibration) : $20 \times 4 = 80$
	GTM-end (global trigger) : 1
	GTM-end (global clock) : 1
	GTM-end (calibration) : 1
Output signals	Pre-trigger fan-out : $27 \times 4 \times 8 = 864$
	GTM-end (local trigger) : 2
	GTM-end (calibration) : 1
	RPC-end (global trigger) : $20 \times 4 = 80$
	RPC-end (global clock) : $20 \times 4 = 80$
RPC-end (calibration) : $20 \times 4 = 80$	
Total i/o signals	2054
T1ST2S blocks	$4 + 4 = 8$
Input signals/ T1ST2S block	RPC-end (pre-trigger) : $27 \times 4 = 108$
Output signals/ T1ST2S block	Pre-trigger fan-out : $27 \times 4 = 108$ Level 2 trigger : 1
Total i/o signals/ T1ST2S block	217
T3S block	1
Input signals/ T3S block	Level 2 trigger : $4 + 4 = 8$
Output signals/ T3S block	Local trigger : 2
Total i/o signals/ T3S block	10
Global trigger fan-out	1 : 80
Global clock fan-out	1 : 80
Calibration block	1
Input signals/ calibration block	RPC-end : 80 GTM-end: 1
Output signals/ calibration block	RPC-end : 80 GTM-end: 1
Total i/o signals/ calibration block	162

Table 24: I/O specifications for the LTM. The quoted figures represent the maximum requirement.

Table 25 lists the I/O specifications of the GTM. All I/O signals will be transmitted using the LVDS standard.

Input signals	Local trigger : $9 \times 2 = 18$ Calibration : 4
Output signals	Global trigger : 4 Global clock : 9 Calibration : 4
Total i/o signals	39
Global trigger fan-out	1 : 4
Global clock fan-out	1 : 9

Table 25: I/O specifications for the GTM.

## 5.5 COMPONENT SELECTION FOR DESIGN OF TRIGGER BOARDS

The essential components for designing the LTM and the GTM boards include FPGAs, LVDS drivers and high density connectors. Since the trigger boards need to handle huge number of I/O signals (~2000) in limited space, the number of I/Os supported by these components and their physical dimensions play the decisive role in their selection. Products from a large pool of vendors have been explored and finally the most expedient ones are chosen.

*FPGAs, LVDS drivers and high density connectors*

### 5.5.1 FPGA

The factors which play important role in selecting the suitable FPGA for designing the trigger boards are mentioned below.

- (i) Number of LVDS I/Os
- (ii) Logic capacity
- (iii) Block RAM capacity
- (iv) Power consumption
- (v) Physical dimension
- (vi) Cost

A number of FPGAs from different families of Altera [86] and Xilinx [87], which satisfy the design specifications for the LTM and the GTM boards, are listed in Table 26. The Cyclone 5 FPGA (5CEBA7F31) from Altera and the Spartan 6 FPGA (XC6SLX150FGG900) from Xilinx are found to be the most suitable candidates for designing the ICAL trigger boards.

*Cyclone 5 FPGA from Altera and Spartan 6 FPGA from Xilinx*

*Total number of  
FPGAs per LTM  
board of each type*

The total number of FPGAs that will be required to design the LTM boards can be derived from the I/O specifications of different subsections of the LTM, as shown in Table 24. Generation of fan-out of the pre-trigger signals and formation of the corresponding Level 2 trigger signal, of each type, can be implemented using 1 FPGA. Production of the Level 3 or local trigger signals from the Level 2 trigger signals and distribution of the global trigger, global clock and calibration signals can be handled by 1 FPGA. Lastly, 1 more FPGA is required to establish the back-end interface and facilitate remote configuration of the other FPGAs.

Hence, the type I LTM board can be designed using a total of 10 FPGAs while design of the type II LTM board requires 9 FPGAs.

### 5.5.2 LVDS drivers

*LVDS driver and  
fan-out chips from  
Texas Instruments*

FPGAs can drive LVDS signals up to a length of 5 – 10 m. However, the type I LTMs need to drive the trigger signals over a length of about 50 m for one module of the ICAL detector and thus LVDS drivers have to be used. Table 27 lists the specifications of the LVDS driver and fan-out chips, selected to be deployed in the type I LTM board.

The 1:10 LVDS fan-out chip (DS90LV110T) [88] will be used to distribute the global trigger and the global clock signals from the LTM to the RPC-DAQ boards of the constituent RPCs of the segment. Similarly, the calibration signals will be transmitted from the LTM to the constituent RPC-DAQ boards through the 16 channel LVDS driver chip (SN75LVDS387DGG) [89].

Apart from driving the trigger signals over long distance, use of the LVDS driver and fan-out chips also results in reduced consumption of the FPGA I/O resources.

### 5.5.3 Connectors

Handling of large number of LVDS I/Os demands use of high density connectors in the trigger boards. The selected products are listed in Table 28.

*High density I/O  
connectors from  
Samtec and Tyco  
Electronics*

The LTM board uses connectors with different pin counts, viz., 50 pin, 16 pin and 114 pin connectors, for various purposes. The 50 pin connectors [90] will be used to receive the pre-trigger signals from the constituent RPC-DAQ boards. The I/O signals between the LTMs and the GTM will be handled by the 16 pin connector [90]. The 114 pin connectors [91] will be used for interconnection between the LTMs. The type I and type II LTM boards require varying numbers of connectors owing to different fan-in and fan-out configurations.

The relatively simpler GTM board uses only 16 pin connectors [90] to communicate with the LTMs.

VENDOR	FAMILY	DEVICE	PACKAGE	DIMENSION	LOGIC CELLS (k)	BLOCK RAM (kB)	TOTAL BLOCK RAM	LVDS I/OS	POWER (W)
Altera	Stratix 4	EP4SE230	FBGA780	29 mm x 29 mm	228	9, 144	1235, 22	244	3.9
	Stratix 4	EP4SE530	FBGA1517	40 mm x 40 mm	531	9, 144	1280, 64	488	
	Arria 5	5AGXA5	FBGA1152	35 mm x 35 mm	190	10	1180	256	
	Cyclone 5	5CEA7	FBGA896	31 mm x 31 mm	150	10	686	240	1.6
Xilinx	Spartan 6	XC6SLX150	FG(G)900	31 mm x 31 mm	147	18	268	288	1.85
	Virtex 6	XC6VLX130T	FF1156	35 mm x 35 mm	128	36	264	300	6.4
	Artix 7	XC7A200T	FFG1156	35 mm x 35 mm	215	36	365	240	3.5
	Virtex 7	XC7V585T	FFG1157	35 mm x 35 mm	583	36	795	288	2.2

Table 26: List of suitable FPGAs from different families of Altera and Xilinx for designing the LTM and the GTM boards.

VENDOR	TYPE	DEVICE	PINS	DIMENSION	NUMBER PER LTM	SIGNAL
Texas Instruments	LVDS fan-out (1:10)	DS90LV110T	28	9.8 mm x 6.6 mm	16	Global trigger, Global clock
Texas Instruments	LVDS driver (16)	SN75LVDS387DGG	64	17.1 mm x 8.3 mm	5	Calibration

Table 27: LVDS driver and fan-out chips selected for designing the type I LTM board.

VENDOR	CONNECTOR	PINS	PITCH (mm)	DIMENSION	SIGNAL
Samtech	SHF-125-01-X-D-SM	50	1.27	9 mm x 46.3 mm	RPC-DAQ I/O
Samtech	SHF-108-01-X-D-SM	16	1.27	9 mm x 24.7 mm	GTM I/O
Tyco Electronics	1-5767096-0	114	0.64	5.4 mm x 50.8 mm	LTM fan-out I/O

Table 28: Different types of high density connectors selected for designing the trigger boards.

#### 5.5.4 Back-end interface

The trigger boards should be equipped with a back-end interface which is essential for several purposes, like, configuration of the LTM FPGAs to implement new trigger criteria, selective masking of signals at different levels of trigger generation, readout of trigger rates and latch data, etc. A standard crate structure is also necessary to accommodate the large number of trigger boards making efficient use of the available space. A commercial bus system such as VME [92] or  $\mu$ TCA [93][94] is the favourable option due to the availability of standard bus protocol and electrical and mechanical specifications.

VME or  
 $\mu$ TCA bus

### 5.6 LTM BOARD DESIGN

The composition of the two types of LTM boards, with the required count of each component, are shown in Table 29.

LTM CATEGORY	Components/ board		
	FPGA	CONNECTORS	LVDS DRIVERS
Type I	10	50 pin : 40 16 pin : 1 114 pin : 20	Fan-out : 16 Driver : 5
Type II	9	16 pin : 1 114 pin : 32	–

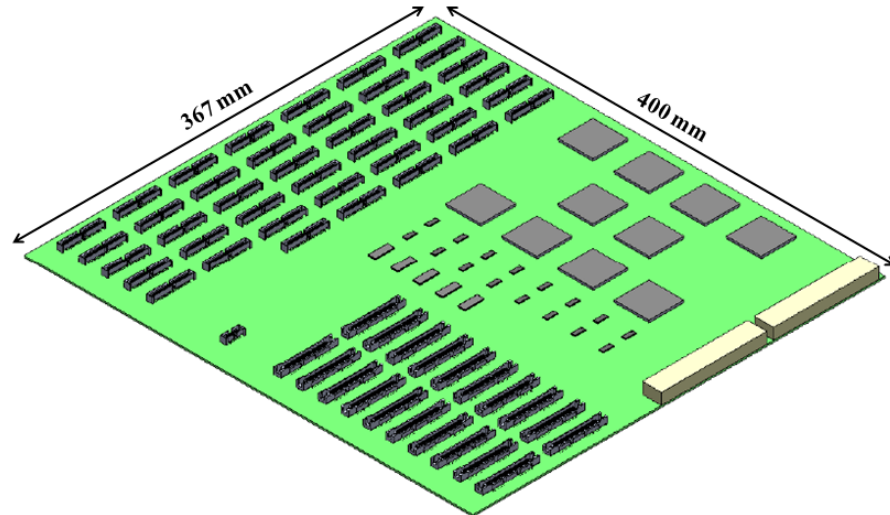
Table 29: Design components for the two types of LTM boards.

The schematics of the LTM boards of two types, containing the essential components, like the FPGAs, LVDS driver and fan-out chips, I/O and VME connectors, are illustrated in Fig. 56a and Fig. 56b. The boards are designed with a form factor of 367 mm x 400 mm (9U). The LTM boards thus designed for the Engineering Module can be deployed in the ICAL detector as well.

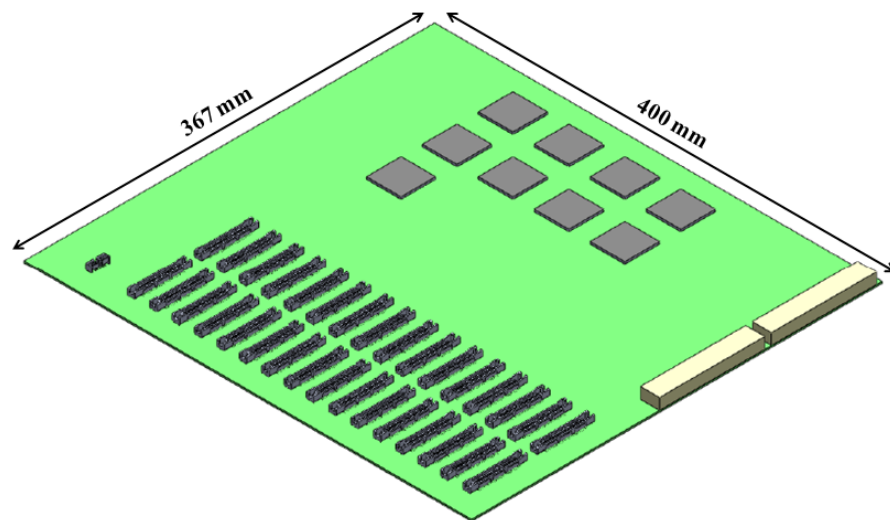
### 5.7 GTM BOARD DESIGN

The I/O specifications of the GTM, listed in Table 25, imply that the necessary functionalities of the GTM for the Engineering Module can be implemented using 1 FPGA, 1 16-channel TDC and 1 oscillator. Design of the GTM for the ICAL detector module, however, would require multiple FPGAs and also multiple boards, as it needs to deal with huge number of I/O connectors, owing to the large number of LTMs (~400).

Fig. 57 shows the schematic of the GTM board for the Engineering Module with the design components like the FPGA, TDC and oscillator



(a)



(b)

Figure 56: Schematic of the LTM board of (a) type I and (b) type II, designed with a 9U (367 mm x 400 mm) form factor, showing the design components like the FPGAs, LVDS driver and fan-out chips, I/O and VME connectors.

chips, I/O and VME connectors. The board is designed with a form factor of 367 mm x 400 mm (9U).

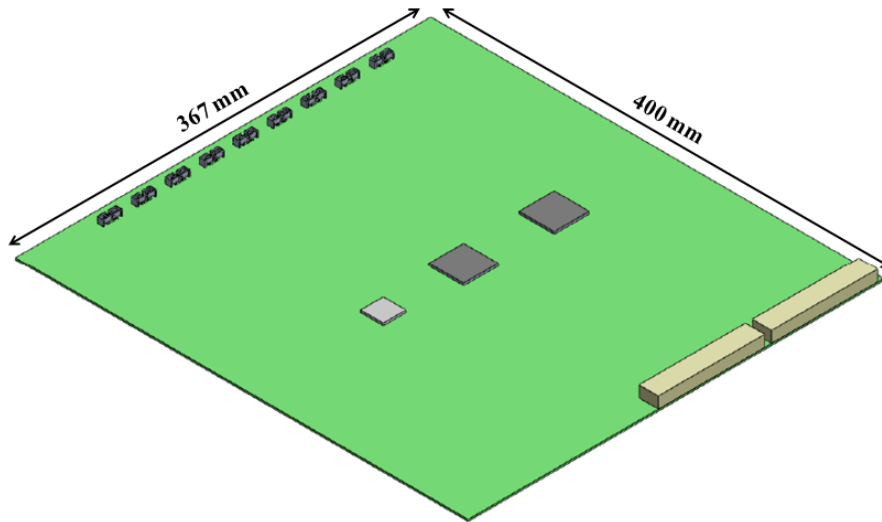


Figure 57: Schematic of the GTM board designed with a 9U (367 mm x 400 mm) form factor, showing the design components like the FPGA, TDC and oscillator chips, I/O and VME connectors.

The viability of the proposed layout for implementation of the ICAL trigger scheme will be assessed by building the trigger system for the Engineering Module in compliance with the same. The designs of the trigger boards, proposed to be used in the ICAL trigger system, are contemplated and the essential design components have been selected. The performance of these trigger boards will be evaluated by deploying them in the Engineering Module.



Part III

CONCLUSIONS



SUMMARY AND FUTURE SCOPE

---

This chapter presents in a nutshell the work on the development, validation and implementation of the ICAL trigger system, elucidated in the previous chapters. The future road map for the successful progress and culmination of this work has been highlighted. The scope of deployment of the same system under different circumstances is also discussed.

*Chapter  
summary*

## 6.1 SUMMARY

The INO collaboration is presently conducting a full-fledged R&D program aimed at building the 50 kton ICAL detector with the goal of studying atmospheric neutrino oscillations. The unique capability of charge identification, by virtue of magnetic field, equips the detector with the potential of resolving the long-standing ambiguity of neutrino mass hierarchy. The detector will be housed inside a cavern with rock overburden of more than 1 km in order to ensure minimal cosmic muon background. Considering the extremely low rate of neutrino interactions, the trigger scheme for such an experiment should achieve maximal detection efficiency for the desired events while minimizing the chance coincidence rates. The vast detector volume, consisting of 28,800 RPCs and more than 3.6 million electronic channels, also poses serious design challenges concerning the feasibility of hardware implementation of the trigger system.

*The ICAL detector  
and the trigger  
system*

A trigger scheme with a distributed and hierarchical architecture, which will satisfy these criteria, has been developed for the ICAL detector. The detector module is logically sub-divided into identical segments for the purpose of trigger generation. The choice of the segment dimensions is based upon the expected hit pattern of the events of interest, the associated chance trigger rates and the feasibility of implementation. Pre-trigger signals produced at the RPC level are combined together to generate a local trigger signal at the segment level. Combination of all the local triggers produces a global trigger signal at the module level which initiates the data acquisition system to record the event data.

*Proposed  
architecture of the  
ICAL trigger scheme*

Chance coincidence rates are calculated for different combinations of the trigger parameters, at successive levels of trigger generation, which help to fix the criteria for an admissible chance trigger rate. A simulation framework has been developed to estimate the trigger efficiency of the scheme for the events of interest for the ICAL detector. Muon as well as neutrino events of different kinds are generated and

*Validation through estimation of chance coincidence rates and determination of trigger efficiency*

simulated using the INO-ICAL simulation package. The output of detector simulation provides the hit position information in the detector which is fed to the trigger simulation framework to determine the trigger efficiency. The results ensure that substantially high detection efficiency ( $> 95\%$ ) can be obtained for the desired events under the proposed trigger scheme. The nature of variation of trigger efficiency as a function of different trigger parameters and the correlation of the trigger parameters with different interaction signatures are also understood. Such observations will be helpful in fixing these parameters to attain the desired efficiency for an event of interest. The validation of the proposed trigger scheme for the ICAL detector has thus been accomplished.

*Design of FPGA-based trigger module and validation in the prototype detector*

As the first step toward the implementation of the trigger scheme, an FPGA-based trigger module is designed using the look-up table based technique. This technique offers the unique advantage that the inner hardware and consequently the processing time, are independent of the input pattern. The look-up tables are implemented using the internal block RAMs of the FPGA. The trigger module is equipped with several features like, selective masking of inputs and intermediate coincidence signals, deglitching of output, internal latches and scalers, etc. The performance of the trigger module is evaluated by deploying it in the prototype detector. Initially, the output of the trigger module is used as the trigger signal for the data acquisition system. The data thus recorded is analysed to determine the fraction of spurious triggers which is found to be less than  $1\%$ . Thereafter, the trigger signal for the data acquisition system is generated independently using a set of scintillator paddles. The trigger inefficiency, estimated by analysis of the recorded data and its comparison with the response of the trigger module, is found to be around  $0.01\%$ . Hence, the trigger module has delivered satisfactory performance in the prototype detector which ascertains the credibility of the technique in designing the ICAL trigger system.

*Layout for implementation of the trigger scheme for the ICAL detector*

The overall layout for the implementation of the proposed trigger scheme for the ICAL detector is then devised. A number of schemes have been surveyed out of which the one that meets the trigger system requirements as well as caters to the integration constraints is opted for. The overall latency associated with trigger generation is estimated taking into consideration the processing and the propagation delays at each level of the trigger system. The LVDS standard has been chosen for transmitting the trigger signals for the ICAL detector. However, the adopted scheme for the placement of the trigger modules implies that the trigger signals have to be driven over a path of length  $40 - 50$  m for one module of the ICAL detector. It is thus necessary to ensure that the signal does not suffer significant distortion while being propagated over such a long distance. A study has been carried out to assess the reliability of LVDS standard in signal transmission over long distance.

The results ensure the deployment of this standard in transmitting the trigger signals for the ICAL detector. Another issue of concern lies with the measurement of the timing of the RPC signals with reference to the global trigger signal. The return-paths of the global trigger signal from the output of the GTM to the inputs of different RPC-DAQ boards are of varying lengths. Hence, accurate estimation of the corresponding delay offsets is absolutely necessary for proper timing measurement. A technique for delay offset calibration, involving different stages of the trigger system, is proposed.

A larger prototype of the ICAL detector is going to be constructed to develop, validate and optimize different detector components. The corresponding trigger system will be built in adherence to the conceived layout for implementation of the ICAL trigger system. The performance of the trigger boards, proposed to be used for the final ICAL detector, will be initially evaluated in the upcoming prototype. The designs of the trigger boards are contemplated and the design components like, FPGAs, connectors, LVDS driver and fan-out chips, etc., have been selected.

The work documented in this thesis has thus facilitated the evolution of the ICAL trigger system from the conceptual stage up to the board-level design.

## 6.2 FUTURE SCOPE

The immediate plan of action comprises procurement of the components chosen for designing the trigger boards, board fabrication and their performance validation in the Engineering Module. Apart from the trigger logic, which has been implemented using the substantiated look-up table based technique, the residual work packages consist of establishing the back-end interface, remote configuration of FPGAs and inter-FPGA communication. The layout design and fabrication of the trigger boards, accommodating large number of components and I/O signals, appear to be challenging tasks and demand use of high-end design tools.

The reliability of the proposed technique for calibrating the delay offsets associated with the return-paths of the global trigger signal, which is crucial for estimating the timing of the RPC signals, needs to be evaluated at the system level. The hardware calibration might be coupled with software calibration as well, which can be obtained through the analysis of straight tracks recorded in the absence of magnetic field.

Another important goal is to accomplish seamless integration of the trigger system with the overall ICAL detector system. This includes routing of the pre-trigger signals from the RPC-DAQ boards to the corresponding LTM, interconnection between adjacent LTMs and between the LTMs and the GTM and propagation of the global trigger

*Design of trigger boards to be validated in upcoming prototype*

*Fabrication and validation of trigger boards*

*Evaluation of delay offset calibration technique*

*System integration*

signal from the GTM to the RPC-DAQ boards. A successful system integration will cater to the mechanical constraints associated with the detector structure without hindering the functionalities of the trigger system.

*Future  
deployment*

Since the ICAL detector is also foreseen as a future far detector for a neutrino factory beam, the trigger system should be capable of operating at high rates. The trigger latency plays a major role in determining the maximum event rate that can be handled by the data acquisition system. A trigger latency of 2  $\mu\text{s}$ , for instance, implies that the events can be recorded by the data acquisition system at a rate no larger than 500 kHz. This can, however, be improved by the use of large readout buffers. The trigger system can also be employed for detecting other varieties of low-rate events, e.g., those induced by dark matter interactions, provided their detection signatures are precisely known.

*Exploring the  
'triggerless' option*

An attractive alternative to the conventional hardware trigger system is to have a triggerless system where the FPGA-based trigger boards are replaced by fast processors. The status of the detector is read at regular intervals, determined by a free-running clock, and the trigger algorithm is implemented in software to identify the events of interest. Circumventing the hardware components is advantageous as it helps to simplify the system integration. The constituent elements of the triggerless system, viz., processors, network interface, software tools, etc., evolve to be technologically superior as well as economical at a rate faster than that of the hardware components like FPGA, VME, etc. However, successful implementation of the triggerless system needs to ensure minimal trigger latency by employing techniques like pipelining, optimizing the trigger algorithms, parallel processing on GPUs and data transfer through high-speed network interfaces. It will be interesting to explore the scope of developing a triggerless system for the ICAL detector once the hardware trigger system is fully operational.

Part IV

APPENDIX



## A.1 PEER-REVIEWED RESEARCH PAPERS

1. **S. Dasgupta**, N.K. Mondal, D. Samuel, M.N. Saraf, B. Satyanarayana, S.S. Upadhyaya, "Development of trigger scheme for the ICAL detector of India-based Neutrino Observatory", Nuclear Instruments and Methods in Physics Research Section A: Accelerators, Spectrometers, Detectors and Associated Equipment, vol. 678, pp. 105–113, 2012.
2. **S. Dasgupta**, N.K. Mondal, D. Samuel, M.N. Saraf, B. Satyanarayana, S.S. Upadhyaya, "Toward the implementation of the trigger scheme for the ICAL detector of India-based Neutrino Observatory", Nuclear Instruments and Methods in Physics Research Section A: Accelerators, Spectrometers, Detectors and Associated Equipment, vol. 694, pp. 126–132, 2012.
3. A. Behere, M. Bhuyan, V.B. Chandratre, **S. Dasgupta**, V.M. Datar, S.D. Kalmani, S.M. Lahange, N.K. Mondal, P.K. Mukhopadhyay, P. Nagaraj, B.K. Nagesh, S. Pal, Shobha.K. Rao, D. Samuel, M.N. Saraf, B. Satyanarayana, R.S. Shastrakar, R.R. Shinde, K.M. Sudheer, S.S. Upadhyaya, P. Verma, "Electronics and data acquisition system for the ICAL prototype detector of India-based Neutrino Observatory", Nuclear Instruments and Methods in Physics Research Section A: Accelerators, Spectrometers, Detectors and Associated Equipment, vol. 701, pp. 153–163, 2013.
4. M. Bhuyan, V.B. Chandratre, **S. Dasgupta**, V.M. Datar, S.D. Kalmani, S.M. Lahange, N.K. Mondal, P. Nagaraj, S. Pal, S.K. Rao, A. Redij, D. Samuel, M.N. Saraf, B. Satyanarayana, R.R. Shinde, S.S. Upadhyaya, "VME-based data acquisition system for the India-based Neutrino Observatory prototype detector", Nuclear Instruments and Methods in Physics Research Section A: Accelerators, Spectrometers, Detectors and Associated Equipment, vol. 661, Supplement 1, pp. S73–S76, 2012.

## A.2 CONFERENCE PROCEEDINGS

1. **S. Dasgupta**, N.K. Mondal, D. Samuel, M.N. Saraf, B. Satyanarayana, S.S. Upadhyaya, "Proposed Trigger Scheme for the ICAL detector of India-based Neutrino Observatory", In proceedings of XI Workshop on Resistive Plate Chambers and Related Detectors, POS(RPC2012)068, 2012.

2. B. Satyanarayana, **S. Dasgupta**, S. Dhuldhaj, N. Mondal, P. Nagaraj, S. Rao, D. Samuel, M. Saraf, R. Shinde, S. Upadhyaya, V. Chandratre, V. Salodia, P. Saxena, M. Tewani, S. Saha, Y. Viyogi, "Electronics and data acquisition systems for the RPC based INO ICAL detector", In proceedings of XI Workshop on Resistive Plate Chambers and Related Detectors, POS(RPC2012)042, 2012.
3. **S. Dasgupta**, N.K. Mondal, D. Samuel, B. Satyanarayana, "Design of FPGA-based TDC for the ICAL detector of India-based Neutrino Observatory", In proceedings of 4th International Conference on Electronics Computer Technology, 2012.

#### A.3 TECHNICAL NOTES

1. **S. Dasgupta**, B. Satyanarayana, S.S. Upadhyaya, "Proposed trigger scheme for the ICAL detector", version 2.1, September 2012.
2. **S. Dasgupta**, M.N. Saraf, B. Satyanarayana, S.S. Upadhyaya, "Design of trigger module for the ICAL prototype detector", version 2.4, August 2012.
3. **S. Dasgupta**, B. Satyanarayana, S.S. Upadhyaya, "Trigger latency estimation for the ICAL detector", version 1.3, January 2013.
4. **S. Dasgupta**, M.N. Saraf, B. Satyanarayana, S.S. Upadhyaya, "Design of trigger system for the ICAL Engineering Module", version 1.2, April 2013.

## BIBLIOGRAPHY

---

- [1] Zhi-Zhong Xing and Shun Zhou. *Neutrinos in Particle Physics, Astronomy and Cosmology*. Springer, 1st edition, 2011.
- [2] W. Pauli. Letter to the participants of workshop at Tübingen, Germany, 1930.
- [3] C.L. Cowan, Jr., *et al.* Detection of the Free Neutrino: a Confirmation. *Science*, 124(3212):103–104, 1956.
- [4] F. Reines and C.L. Cowan, Jr. The Neutrino. *Nature*, 178:446, 1956.
- [5] Claus Grupen and Irène Buvat (Eds.). *Handbook of Particle Detection and Imaging*. Springer, 2012.
- [6] INO Project Report, vol. 1, <http://www.ino.tifr.res.in/ino/OpenReports/INOReport.pdf>, 2006.
- [7] Claus Grupen and Boris Shwartz. *Particle Detectors*. Cambridge University Press, 2nd edition, 2008.
- [8] M. Bhuyan *et al.* Development of 2 m x 2 m size glass RPCs for INO. *Nuclear Instruments and Methods in Physics Research Section A*, 661:S64–S67, 2012.
- [9] A. Garfagnini *et al.* The OPERA muon spectrometers. *Nuclear Instruments and Methods in Physics Research Section A*, 572(1):177–180, 2007.
- [10] J. Allison *et al.* Geant4—a simulation toolkit. *Nuclear Instruments and Methods in Physics Research Section A*, 506(3):250–303, 2003.
- [11] D. Casper. The nuance Neutrino Physics Simulation and the Future. *Nuclear Physics B Proceedings Supplements*, 112:161–170, 2002.
- [12] M. Bhuyan *et al.* Cosmic ray test of INO RPC stack. *Nuclear Instruments and Methods in Physics Research Section A*, 661:S68–S72, 2012.
- [13] A. Behere *et al.* Electronics and data acquisition system for the ICAL prototype detector of India-based Neutrino Observatory. *Nuclear Instruments and Methods in Physics Research Section A*, 701:153–163, 2013.
- [14] Altera Corporation. Cyclone Device Handbook, vol. 1, <http://www.altera.com/literature/>, 2008.

- [15] CAEN. Mod. V1495 Technical Information Manual, rev. 11, <http://www.caen.it/csite/>, 2012.
- [16] Draka. SuperCat 5 24 Cat.5e U/UTP installation cable for outdoor use, [http://communications.draka.com/sites/eu/Datasheets/SuperCat5\\_24\\_U\\_UTP\\_Install.pdf](http://communications.draka.com/sites/eu/Datasheets/SuperCat5_24_U_UTP_Install.pdf), 2009.
- [17] C.D. Ellis and W.A. Wooster. The Average Energy of Disintegration of Radium E. *Proc. R. Soc. Lond. A*, 117:109–123, 1927.
- [18] L. Meitner and W. Orthmann. *Z. Phys.*, 60:143–155, 1930.
- [19] N. Bohr. Chemistry and Quantum Theory of Atomic Constitution (Faraday Lecture). *J. Chem. Soc.*, 135:349–384, 1932.
- [20] E. Fermi. *La Ricerca Scientifica*, 2:12, 1933.
- [21] E. Fermi. *Z. Phys.*, 88:161, 1934.
- [22] H. Bethe and R. Peierls. The "Neutrino". *Nature*, 133:532, 1934.
- [23] T.D. Lee and C.N. Yang. *Proceedings of the International Conference on High Energy Physics, Rochester (New York: Interscience)*, page 567, 1960.
- [24] G. Danby *et al.* Observation of High-Energy Neutrino Reactions and the Existence of Two Kinds of Neutrinos. *Phys. Rev. Lett.*, 9:36–44, 1962.
- [25] M. Perl *et al.* Evidence for Anomalous Lepton Production in  $e^+e^-$  Annihilation. *Phys. Rev. Lett.*, 35:1489–1492, 1975.
- [26] Kodama *et al.* (DONuT collaboration). Observation of tau neutrino interactions. *Phys. Lett. B*, 504:218–224, 2001.
- [27] B. Adeva *et al.* (L3 collaboration). A determination of the properties of the neutral intermediate vector boson  $Z^0$ . *Phys. Lett. B*, 231:509–518, 1989.
- [28] D. Decamp *et al.* (ALEPH collaboration). Determination of the number of light neutrino species. *Phys. Lett. B*, 231:519–529, 1989.
- [29] M.Z. Akrawy *et al.* (OPAL collaboration). Measurement of the  $Z^0$  mass and width with the opal detector at LEP. *Phys. Lett. B*, 231:530–538, 1989.
- [30] P.A. Arnio *et al.* (DEPHI collaboration). Measurement of the mass and width of the  $Z^0$ -particle from multihadronic final states produced in  $e^+e^-$  annihilations. *Phys. Lett. B*, 231:539–547, 1989.
- [31] S.L. Glashow. Partial-symmetries of weak interactions. *Nucl. Phys.*, 22:579–588, 1961.

- [32] S. Weinberg. A Model of Leptons. *Phys. Rev. Lett.*, 19:1264–1266, 1967.
- [33] A. Salam. *Proceedings of the 8th Nobel Symposium on 'Elementary Particle Theory, Relativistic Groups and Analyticity', Stockholm, Sweden*, pages 367–377, 1969.
- [34] S. Chatrchyan *et al.* (CMS collaboration). Observation of a new boson at a mass of 125 GeV with the CMS experiment at the LHC. *Phys. Lett. B*, 716:30–61, 2012.
- [35] G. Aad *et al.* (ATLAS collaboration). Observation of a new particle in the search for the Standard Model Higgs boson with the ATLAS detector at the LHC. *Phys. Lett. B*, 716:1–29, 2012.
- [36] iSGTW (international science grid this week). <http://www.isgtw.org/spotlight/go-particle-quest-first-cern-hackfest>, 2012.
- [37] B. Pontecarvo. *Sov. Phys. JETP*, 6:429, 1957.
- [38] B. Pontecarvo. *Sov. Phys. JETP*, 7:172–173, 1958.
- [39] Z. Maki *et al.* Remarks on the Unified Model of Elementary Particles. *Prog. Theor. Phys.*, 28:870–880, 1962.
- [40] L. Wolfenstein. Neutrino Oscillations In Matter. *Phys. Rev. D*, 17:2369, 1978.
- [41] S.P. Mikheev and A.Y. Smirnov. Resonance Enhancement Of Oscillations In Matter And Solar Neutrino Spectroscopy. *Sov. J. Nucl. Phys.*, 42:913–917, 1985.
- [42] A. Gouvêa. On determining the neutrino mass hierarchy, <http://theory.fnal.gov/seminars/slides/2006/AGouvea.pdf>, 2006.
- [43] C. Kraus *et al.* Final results from phase II of the Mainz neutrino mass search in tritium  $\beta$  decay. *Eur. Phys. J.*, 40:447–468, 2005.
- [44] V.M. Lobashev *et al.* Direct search for mass of neutrino and anomaly in the tritium beta-spectrum. *Phys. Lett. B.*, 460:227–235, 1999.
- [45] J.N. Bahcall *et al.* Solar Neutrinos. I. Theoretical. *Phys. Rev. Lett.*, 12:300–302, 1964.
- [46] K. Hirata *et al.* (Kamiokande collaboration). Observation of a neutrino burst from the supernova SN1987A. *Phys. Rev. Lett.*, 58:1490–1493, 1987.
- [47] R.M. Bionta *et al.* (IMB collaboration). Observation of a neutrino burst in coincidence with supernova 1987A in the Large Magellanic Cloud. *Phys. Rev. Lett.*, 58:1494–1496, 1987.

- [48] E.N. Alekseev *et al.* Possible detection of a neutrino signal on 23 February 1987 at the Baksan underground scintillation telescope of the Institute of Nuclear Research. *JETP Lett.*, 45:589–592, 1987.
- [49] R. Davis. Solar Neutrinos. II. Experimental. *Phys. Rev. Lett.*, 12:303–305, 1964.
- [50] R. Davis *et al.* Search for Neutrinos from the Sun. *Phys. Rev. Lett.*, 20:1205–1209, 1968.
- [51] P. Anselmann *et al.* (GALLEX collaboration). Solar neutrinos observed by GALLEX at Gran Sasso. *Phys. Lett. B*, 285:376–389, 1992.
- [52] P. Anselmann *et al.* (GALLEX collaboration). Implications of the GALLEX determination of the solar neutrino flux. *Phys. Lett. B*, 285:390–397, 1992.
- [53] A.I. Abazov *et al.* Search for neutrinos from the Sun using the reaction  ${}^{71}\text{Ga}(\nu_e, e^-){}^{71}\text{Ge}$ . *Phys. Rev. Lett.*, 67:3332–3335, 1991.
- [54] M. Altmann *et al.* (GNO collaboration). Complete results for five years of GNO solar neutrino observations. *Phys. Lett. B*, 616:174–190, 2005.
- [55] J.N. Abdurashitov *et al.* Measurement of the Solar Neutrino Capture Rate by the Russian-American Gallium Solar Neutrino Experiment During One Half of the 22-Year Cycle of Solar Activity. *J. Exp. Theor. Phys.*, 95:181–193, 2002.
- [56] M. Koshiba. Observational neutrino astrophysics. *Phys. Rep.*, 220:229–381, 1992.
- [57] Y. Fukuda *et al.* (Kamiokande collaboration). Solar Neutrino Data Covering Solar Cycle 22. *Phys. Rev. Lett.*, 77:1683–1686, 1996.
- [58] J. Hosaka *et al.* (Super-Kamiokande Collaboration). Solar neutrino measurements in Super-Kamiokande-I. *Phys. Rev. D*, 73:112001, 2006.
- [59] J. Boger *et al.* (The SNO Collaboration). The Sudbury Neutrino Observatory. *Nucl. Instrum. Meth. A*, 449:172–207, 2000.
- [60] B. Aharmim *et al.* (The SNO Collaboration). Electron energy spectra, fluxes, and day-night asymmetries of  ${}^8\text{B}$  solar neutrinos from measurements with NaCl dissolved in the heavy-water detector at the Sudbury Neutrino Observatory. *Phys. Rev. C*, 72:055502, 2005.
- [61] C. Arpesella *et al.* (Borexino Collaboration). First real time detection of  ${}^7\text{Be}$  solar neutrinos by Borexino. *Phys. Lett. B*, 658:101–108, 2008.

- [62] Y. Ashie *et al.* (Super-Kamiokande Collaboration). Measurement of atmospheric neutrino oscillation parameters by Super-Kamiokande I. *Phys. Rev. D*, 71:112005, 2005.
- [63] K. Eguchi *et al.* (KamLAND Collaboration). First Results from KamLAND: Evidence for Reactor Antineutrino Disappearance. *Phys. Rev. Lett.*, 90:021802, 2003.
- [64] T. Araki *et al.* (KamLAND Collaboration). Measurement of Neutrino Oscillation with KamLAND: Evidence of Spectral Distortion. *Phys. Rev. Lett.*, 94:081801, 2005.
- [65] M. Apollonio *et al.* Initial results from the CHOOZ long baseline reactor neutrino oscillation experiment. *Phys. Lett. B*, 420:397–404, 1998.
- [66] M. Apollonio *et al.* Search for neutrino oscillations on a long base-line at the CHOOZ nuclear power station. *Eur. Phys. J. C*, 27:331–374, 2003.
- [67] Y. Abe *et al.* (Double Chooz Collaboration). Indication of Reactor  $\bar{\nu}_e$  Disappearance in the Double Chooz Experiment. *Phys. Rev. Lett.*, 108:131801, 2012.
- [68] F.P. An *et al.* Observation of Electron-Antineutrino Disappearance at Daya Bay. *Phys. Rev. Lett.*, 108:171803, 2012.
- [69] J.K. Ahn *et al.* (RENO Collaboration). Observation of Reactor Electron Antineutrinos Disappearance in the RENO Experiment. *Phys. Rev. Lett.*, 108:191802, 2012.
- [70] S.H. Ahn *et al.* Detection of accelerator-produced neutrinos at a distance of 250 km. *Phys. Lett. B*, 511:178–184, 2001.
- [71] E. Aliu *et al.* (The K2K Collaboration). Evidence for Muon Neutrino Oscillation in an Accelerator-Based Experiment. *Phys. Rev. Lett.*, 94:081802, 2005.
- [72] S. Yamamoto *et al.* (K2K Collaboration). Improved Search for  $\nu_\mu \rightarrow \nu_e$  Oscillation in a Long-Baseline Accelerator Experiment. *Phys. Rev. Lett.*, 96:181801, 2006.
- [73] P. Adamson *et al.* (MINOS Collaboration). Study of muon neutrino disappearance using the Fermilab Main Injector neutrino beam. *Phys. Rev. D*, 77:072002, 2008.
- [74] P. Adamson *et al.* (MINOS Collaboration). Measurement of the Neutrino Mass Splitting and Flavor Mixing by MINOS. *Phys. Rev. Lett.*, 106:181801, 2011.
- [75] Y. Itow *et al.* (T2K Collaboration). The JHF-Kamioka neutrino project. *hep-ex/0106019*, 2001.

- [76] D. Beavis *et al.* Long Baseline Neutrino Oscillation Experiment at the AGS (Proposal E889), Physics Design Report, BNL 52459, 1995.
- [77] K. Abe *et al.* (T2K Collaboration). Indication of Electron Neutrino Appearance from an Accelerator-Produced Off-Axis Muon Neutrino Beam. *Phys. Rev. Lett.*, 107:041801, 2011.
- [78] G.L. Fogli *et al.* Evidence of  $\theta_{13} > 0$  from global neutrino data analysis. *Phys. Rev. D*, 84:053007, 2011.
- [79] C.V. Achar *et al.* Detection of muons produced by cosmic ray neutrinos deep underground. *Phys. Lett.*, 18:196–199, 1965.
- [80] C.V. Achar *et al.* Observation of a non-elastic cosmic ray neutrino interaction. *Phys. Lett.*, 19:78–80, 1965.
- [81] B. Satyanarayana *et al.* Electronics and data acquisition systems for the RPC based INO ICAL detector. In *proceedings of XI Workshop on Resistive Plate Chambers and Related Detectors*, POS(RPC2012)042, 2012.
- [82] Nokia Corporation. Qt – cross-platform application and UI framework, <http://qt.nokia.com/>, 2012.
- [83] V.M. Datar *et al.* Development of glass resistive plate chambers for INO experiment. *Nuclear Instruments and Methods in Physics Research Section A*, 602:744–748, 2009.
- [84] National Semiconductor. DS90C031B LVDS Quad CMOS Differential Line Driver, <http://pdf1.alldatasheet.com/datasheet-pdf/view/225792/NSC/DS90C031BTM.html>, 2001.
- [85] National Semiconductor. DS90C032B LVDS Quad CMOS Differential Line Receiver, <http://pdf1.alldatasheet.com/datasheet-pdf/view/225795/NSC/DS90C032BTM.html>, 2003.
- [86] Altera Corporation. <http://www.altera.com/devices/fpga/fpga-index.html>, 2013.
- [87] Xilinx. <http://www.xilinx.com/products/silicon-devices/fpga/index.htm>, 2013.
- [88] Texas Instruments. <http://www.ti.com/product/ds90lv110t>, 2011.
- [89] Texas Instruments. <http://www.ti.com/product/sn75lvds387>, 2001.
- [90] Samtec. <http://www.samtec.com/documents/webfiles/pdf/shf.pdf>, 2013.

- [91] Tyco Electronics Corporation. <http://www.te.com/catalog/feat/en/c/11473?BML=10576,17745,17739>, 2013.
- [92] VITA. <http://www.vita.com/>, 2011.
- [93] Vadatech Inc. <http://vadatech.com/>, 2008.
- [94] N.A.T. GmbH. <http://www.nateurope.com/>, 2012.